Molecular nanostructures on ferromagnetic metals for spintronics

Instituto de Ciencia Molecular

Universitat de Valencia

Memoria presentada por Michele Mattera para aspirar al grado de Doctor en Nanociencia y Nanotecnologia

Septiembre 2017

Directores :

Prof. Eugenio Coronado Miralles

Dra. Alicia Forment Aliaga

Dr. Sergio Tatay

Tutor

Dra. Alicia Forment Aliaga

D. EUGENIO CORONADO MIRALLES, catedratico del Departamento de Química Inorgánica de la Universitat de Valencia, Dña. ALICIA FORMENT ALIAGA doctora por la Universitat de Valencia y actualmente investigadora en el Instituto de Ciencia Molecular de la Universitat de Valencia y D. SERGIO TATAY, doctor por la Universitat de Valencia y actualmente investigadora en el Instituto de Ciencia Molecular de la Universitat de Valencia,

CERTIFICAN:

Que la memoria presentada por D. Michele Mattera con titulo: Molecular nanostructures on ferromagnetic metals for spintronics corresponde a su Tesis Doctoral y ha sido realizada bajo su dirección en el Instituto de Ciencia Molecular, autorizando mediante este escrito la presentación de la misma para optar al grado de Doctor.

En Paterna, a 26 de Septiembre de 2017

Prof. Eugenio Coronado Miralles

Dra Alicia Forment Aliaga

Dr Sergio Tatay

Michele Mattera

1. *When a distinguished but elderly scientist states that something is possible, he is almost certainly right. When he states that something is impossible, he is very probably wrong.*

2. *The only way of discovering the limits of the possible is to venture a little way past them into the impossible.*

3. *Any sufficiently advanced technology is indistinguishable from magic.*

Arthur C.Clarke ' Laws

to my wife MaFe,

my parents Paola and Salvatore,

and my grandparents.

Table of Contents

Acknowledgements

The road to accomplish the title of PhD is long, but the path is made of a large number of people, that I will divide in different groups, to which I would express my thankfullness personally.

The first group, is the one of the directors: Prof. Eugenio Coronado, Dra Alicia Forment and Dr Sergio Tatay. The three of them have been so important during these years with their enduring support, talks about problems, and brainstormings to reach the new frontiers in organic and molecular spintronics. I would like to thank Prof Eugenio Coronado, for welcoming in his group to develop my PhD. For my supervisors Alicia and Sergio, I would like to thank them, for their ideas to solve especially the organization of chapter 4, that still remains an interesting work with some open issues.

A special thank goes to my parents, Paola and Salvatore, with their endless support you gave me the motivation, along these years, to pursue my ambition to obtain a PhD degree in Nanoscience, even if you are not so familiar with this theme.

I want to give a special thank to my wife, Mafe, who waited for me to finish and helped me maintaining clear my focus and motivation to achieve the best results as possible.

An important group is made by the people which were not in the lab, but mean very much to me: my wife and mine cousins, Elisabetta, Guglielmo, Alessandro, Erika which had always a joke to help me relax during the holidays (easter, summer or Christmas).

The lab people group with which I spent so many hours together, in different aspects : from longer measurements sessions in the lab with different equipments, like Ramon, Garin, Victor in the AFM lab, with music and jokes, Marc with Raman, who has so many patience to obtain the best conditions for the measurement. The technicians, Angel, Jose, Eva, who supported me in the routine of the lab. There were also people that supported me outside the lab, like the people who already finished their thesis but were up to join in social dinners, or simply having a refreshing beer in the plaza de los negritos, in the city center. These people are Mauri, who was also my bestman, David, Jorge, Maria and all the others mentioned before.

I would like to thank the all the people from the office 2.10.1-3: Efren, Julia, Elena, Yoan, Juan Pablo, Walter, Sara, Samuel y Ramon, Marco and Manel. With you I could balance the long days with some jokes, while smoking outside and drinking a coffee, and we also talked about chemistry, physics, and all the wonderful hidden in the quantum world.

All of you are so important to the ultimate goal of a PhD Thesis, the possibility to create a network that will persist also when the thesis ends, and I hope will support me for years.

I would also thank the eventual reader, which will find all the information to repeat my experiments, and in the case it helps to motivate him/her to do a PhD, I hope he/she will improve my work and maybe obtain something interesting from it.

Motivation and organization of this thesis

The main goal that motivated the development of this thesis was the preparation of new protocols to functionalize room temperature ferromagnetic materials by means of the formation of self-assembled monolayers (SAMs). We pursued to create inorganic/organic interfaces through strategies that i) are cheap and easily applicable in a chemistry lab; ii) do not degrade the magnetic nature of the underlying substrate; iii) lead to high-quality, oxide free interfaces like those needed when the interface is implemented in spintronic devices. Therefore, metals and alloys such as cobalt and permalloy, which magnetization and spin polarization properties persist at room temperature and have been widely used in spintronics, have been our focus of study.

This manuscript is divided in four main chapters:

In Chapter 1 a brief introduction to the concept of SAMs is presented. First, we will discuss the chemical groups commonly chosen to functionalize different kinds of surfaces, then, we will summarize the surface characterization

techniques usually applied to study these SAMs. Finally, a brief summary of SAMs most common applications will be presented.

Chapter 2 is focused on the functionalization of permalloy through the attachment of the molecular units to its passivating oxide layer. We will present a strategy that combines hydrogen plasma treatment, to increase the oxide reactivity and wet chemistry to form high quality SAMs of alkylphosphonic acids (APAs). We will also show how microcontact printed SAMs can be successfully prepared and that they can be used as efficient etch resistant layers.

In Chapter 3 a new protocol to recover already passivated ferromagnetic metals is presented. We will pursue a selective removal of the oxide layer without damaging the metallic bulk and compatible with lithographic techniques used in modern spintronic device production. The method presented here can be used to allow the preparation of SAMs directly on the ferromagnetic metallic surface. At the end of the chapter, we will briefly discuss how these hybrid interfaces composed of SAM and metal have been successfully integrated in magnetic tunnel junctions that are able to work at room temperature.

During the development of chapter 3, we observed the appearance of discrete lamellar domains on the surface of alkanethiolate modified ferromagnetic surfaces when they were exposed to air. This spontaneous effect had been never reported before. In chapter 4, we present a detailed study of these domains by means of different surface characterization techniques that

permitted us to follow the growing process in real time and unravel the metal organic nature of these lamellar structures.

Finally, we summarize the general conclusions that can be extracted from the research results reported in this thesis as well as the future perspectives, along with some questions that in our opinion still remain open, but that we expect to tackle in the future.

At the end of the manuscript, we have included a specific section that describes the experimental methods used and developed during this work. Moreover, we have included an appendix that explain in more detail some specific characterization techniques, such as AFM, XRR and IRRAS, used thorough the development of this thesis. We hope that this information will help those not familiar with them to better follow the results presented here.

Abbreviations

µCP	Microcontact printing
AES	Auger electron spectroscopy
AF	Antiferromagnetic
AFM	Atomic force microscopy
Alq	Tris(hydroxyquinoline)aluminium(III)
AMR	Anisotropic magnetoresistance (AMR)
APAs	Alkylphosphonic acids
CD	Compact disc
Co	Cobalt
CoFeB	Cobalt Iron Boron
Fe	Iron
FM	Ferromagnetic
GA	Glycolic acid
GIXRD	Grazing incidence X-ray diffraction
GMR	Giant magnetoresistance effect
IRRAS	Infrared reflection absorption spectroscopy
ITO	Indium tin oxide
LBL	Layer-by-layer
LDHs	Layered double hydroxides
LEDs	Light emitting diodes
LMAs	Lamellar Metal-alkanethiolates
LSMO	Lanthanum Strontium Manganite Oxide
MALDI-TOF	Matrix assisted laser desorption/ionization time of flight
MOKE	Magneto-optical Kerr effect

MRAM	Magnetoresistive random-access memories
MTJ	Magnetic tunnel junction
ND	Neutral-density filter
Ni	Nickel
Py	NiFe alloy or Permalloy
OFETs	Organic field effect transistors
OLEDs	Organic light emitting diodes
PDMS	Polydimethylsiloxane
SAES	Scanning Auger electron spectroscopy
SAMs	Self-assembled monolayers
surMOF	Surface metal organic framework
SV	Spin-valve
T	slab thickness
T_6	Sexithienyl
TMDCs	Transition metal dichalcogenides
TMR	Tunnel magneto resistance
TOF-SIMS	Time of flight secondary ions mass spectrometry
TS	Template stripping
wθAA	Water advancing contact angle
wθCA	Water contact angle
wθRA	Water receding contact angle
XAS	X-ray absorption spectroscopy
XMCD	X-ray magnetic circular dichroism
XPS	X-ray photoelectron spectroscopy
XRR	X-ray reflectivity
ρ	Density of the material in the slab

List of publications

1. Michele Mattera, Ramón Torres-Cavanillas, Juan Pablo Prieto-Ruiz, Helena Prima-Garcia, Sergio Tatay, Alicia Forment-Aliaga and Eugenio Coronado, Self-Assembled Monolayers on a Ferromagnetic Permalloy Surface. *Langmuir* **31,** 5311–5318 (2015).

2. Marta Galbiati, Sophie Delprat, Michele Mattera, Samuel Mañas-Valero, Alicia Forment-Aliaga, Sergio Tatay, Cyrile Deranlot, Pierre Seneor, Richard Mattana and Frédéric Petroff, Recovering ferromagnetic metal surfaces to fully exploit chemistry in molecular spintronics. *AIP Adv.* **5,** 57131 (2015).

3. Michele Mattera, Marta Galbiati, Sergio Tatay, Alicia Forment-Aliaga and Eugenio Coronado, Spountaneous formation of lamellar island domains on ferromagnetic surfaces (*manuscript in preparation*).

4. Víctor Rubio-Giménez, Marta Galbiati, Javier Castells-Gil, José Navarro-Sánchez, Garín Escorcia-Ariza, Michele Mattera, Thomas Arnold, Jonathan Rawle, Sergio Tatay, Eugenio Coronado and Carlos Martí-Gastaldo, Bottom-up fabrication of conductive Metal-Organic Frameworks ultrathin films (*manuscript submitted*)

List of Figures

Chapter 1

Chapter 2

Chapter 3

Chapter 4

Appendix

List of Tables

Chapter 1

Chapter 2

Chapter 3

Chapter 4

1 Introduction

1.1 Self-assembled monolayers for surface functionalization

Self-assembled monolayers (SAMs) are ordered molecular assemblies formed from the spontaneous adsorption of an active surfactant on a solid substrate.[1] This process can take place both in liquid or in gas phase. The liquid approach has been the most extensively used, in particular, by chemists. This approach will be also the one used in this thesis.

As represented in Figure 1, the surfactant can be divided in three main parts: 1) heading or functional group, 2) body or backbone and 3) anchoring fragments/groups. As we will see below, each one of them plays a particular role in the assembly.

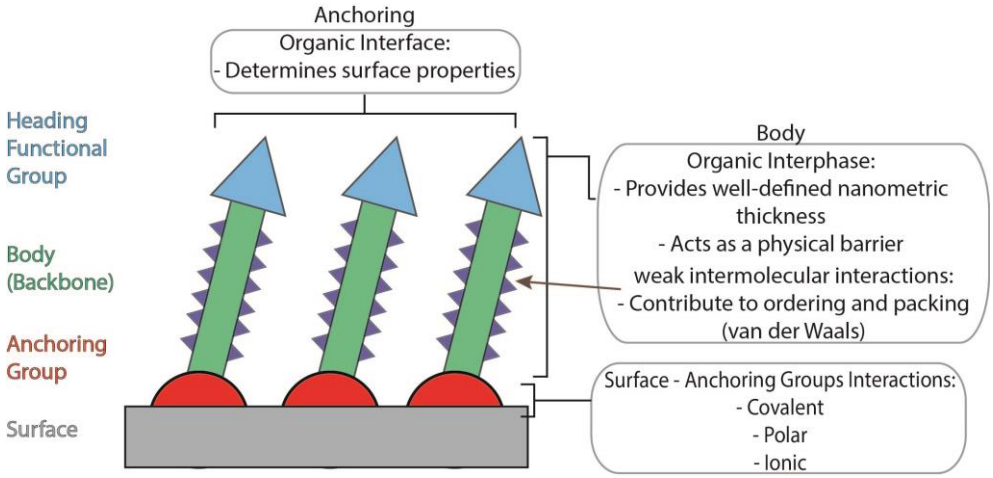

Figure 1 - Pictorial representation of the structure of a SAM highlighting its different parts and its properties.

Anchoring group

The anchoring group is able to recognize the surface linking the molecule to the surface through chemical interactions. As summarized in the Table 1 this process tends to be selective. For example, silane groups ($-SiR_3$, R = -H, -Cl, $-OCH_2CH_3$…), can hydrolyze in the presence of surface hydroxyl groups, giving rise to strong siloxane bonds. For that reason, they have been used to functionalize silicon, both native and thermal,[2] as well as the metal oxides of hafnium,[3] titanium,[4] or indium and tin (ITO).[5]

In a similar way, carboxylic and phosphonic acids show affinity towards oxides too. They also form hydrogen and/or ester bonds with the hydroxyl groups present on the oxide surface. As a result, these anchoring groups have been extensively used to form SAMs on oxides of aluminium,[6] titanium,[7] hafnium,[8] zinc,[9] zirconium[10] and ITO.[11] Compared to silanes, phopshonic acids display

some advantages: they react easily with metal oxide surfaces, have less tendency to homocondensate and are not so dependent on the quantity of surface hydroxyl groups. Moreover, once formed, the resulting SAMs present better stability to moisture.[12–17]

Table 1 - Anchoring group–surface combinations commonly used in SAM formation.

Anchoring Group	Substrate	Ref	Anchoring Group	Substrate	Ref
RCOO-/RCOOH	α-Al_2O_3	18,19	**RSeH**	Ag	20,21
	Ti/TiO_2	22,23		Au	24,21
	AgO	25,26	**RSeSeR'**	Au	24,21
RSH	Ag	27,28			
	Au	27,28		Al	29,30
	Cu	27,31		Al-OH	32,30
	Fe	33,34	**RPO_3^{2-}/$RP(O)(OH)_2$**	Mica	35
	Hg	36,37		ITO	38,11
	Ni	39,40		TiO_2	4,30
	Pd	41,42			
	Pt	43,44		HfO_2	3,4
	Co	45,46	**$RSiX_3$**	ITO	47,5
RSSR'	Ag	48,49	**X= H, Cl, OCH_3, CH_3**	SiO_2	2,50
	Au	51,52		TiO_2	4,53

On the other side, Group 16 chalcogenide elements like sulfur and selenium in the form of thiols or selenols, can form strong R–S/Se–M bonds (being R an

hydrocarbonated chain and M a metal). They have been used to functionalize gold[54], silver,[27] copper,[27] platinum[55] and mercury.[36]

In these previous examples, depending on the nature of the surface, different anchoring groups can be selected for the assembly process (Table 1). The nature and strength of the interaction can vary from pure covalent, in the case of silane on silicon oxide, to covalent but slightly polar, in the case of thiols on gold, or even ionic, in the case of carboxylic acids on silver oxide.

Body/backbone part

The body, or the backbone of the surfactant, can contain for example aromatic rings or hydrocarbonated alkane, alkene or alkyne chains. During the self-assembly, intermolecular forces between neighbor body groups tend to contribute to stabilize the structure favoring the assembly process and leading to an efficient molecular packing, as represented in Figure 1. For example, in the case of alkylic hydrocarbon chains, during the first stages of the assembly, intermolecular interactions are weak and methylene groups freely rotate one with respect to the other. Later on, as the assembly spontaneously continues, intermolecular interactions become more important and eventually, consecutive methylene groups adopt a trans conformation to maximize van der Waals interactions between neighboring chains. The initial liquid-like film gives rise to a more crystalline, dense and robust SAM. In the case of aromatic rings, π-stacking interactions can also play a significant role in their packing.[56]

The presence or the absence of conjugated bonds, in the backbone of the molecule will also define the electronic transport through the formed monolayer. SAMs formed by saturated chains are insulating,[57] while conjugated or aromatic ones tend to be more conducting.[58]

Head group

Finally, the head group is the part mainly responsible of defining the new air-substrate interface and determines the potential uses of the new functionalized surface. As we will see later in section 1.3, SAMs including polar/apolar head groups can be employed to render hydrophilic/hydrophobic surfaces.[27] Other possibility is to utilize the head group as scaffolds to anchor other molecules, biomolecules or nanostructures using covalent bonds or supramolecular interactions.[59]

1.2 Characterization techniques

In order to characterize SAM properties and structure, specific surface-sensitive techniques are needed. In the next paragraphs, we will briefly describe some of these techniques and the information about the SAM that can be extracted.

Contact angle goniometry[60] is a fast and convenient technique to characterize the formation of a SAM. It is based on the study of the change of surface wetting properties, contact angle, resulting from SAM formation. The measurement can be carried out using two modes: static and dynamic. In the

static mode, when a drop of solvent with a determined volume is placed on the surface, this technique is used to analyze the contact angle (θ_A), defined as the tangent of the meniscus formed between the drop and the surface. As an example, air stored gold surfaces have a water contact angle ($w\theta_{CA}$) below 50°. If the sample is treated with an oxidizing solution (i.e. piranha) to remove adventitious contaminants, the $w\theta_{CA}$ will drop below 10°, while in the case of a functionalized surface with an alkanethiol SAM, it will rise to 110° or higher, as a result of the high hydrophobic nature of the formed SAM. However, if we change water by hexane, the drop will cover the entire surface of the SAM, confirming the hydrophobicity of the alkanethiolate SAM.[61]

In the **dynamic mode sessile drop method**, the volume of the drop is changed dynamically, first adding a determined volume that will result in the growth of the drop until a plateau is reached - the formed angle is called water advancing contact angle ($w\theta_{AA}$;Figure 2a) – then, the same volume is removed until a second plateau is reached, which will define the receding contact angle ($w\theta_{RA}$; Figure 2b). Usually the measurement of this second plateau is less reproducible compared to the first one, due to liquid sorption or solid swelling.[62] We can define the hysteresis as the difference between $w\theta_{AA}$ and $w\theta_{RA}$. It can be correlated with the quality of the formed monolayer. Smaller differences are characteristic of defect-free SAMs. In this work the dynamic mode will be used to characterize the studied SAMs.

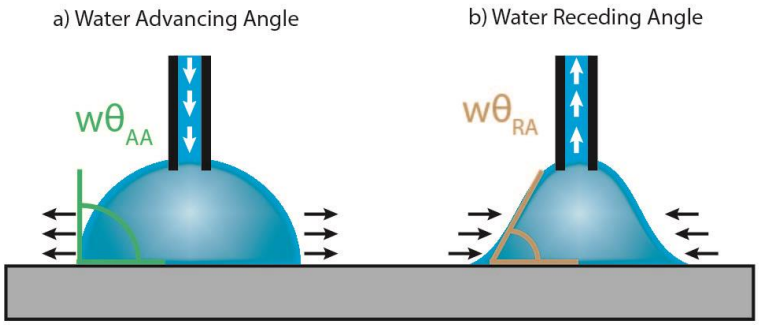

Figure 2 – Schematic representation of the dynamic sessile drop method : a) $w\theta_{AA}$: a constant volume of water is added to the first drop till reaching a plateau. b) $w\theta_{RA}$: a constant volume of water is removed from the drop till reaching a plateau.

Atomic force microscopy (AFM)[63] is one of the most used characterization tools to determine topographical properties of a surface. A sharp tip, placed at the end of a cantilever, is approached to the surface of the sample in a controlled way. Using piezoelectric elements that assure the micrometric positioning, the tip is scanned over the surface following the topography of the sample. When a SAM is formed through the nucleation of discontinuous domains, (i.e.: alkylphosphonic acids SAMs on mica),[35] by means of AFM, one can observe their growth and aggregation in real-time (Figure 3). In other cases, where the formed monolayer replicates the topography of the underlying surface,[64] (i.e.: alkanethiol SAMs on gold) topographic AFM measurements only provide us information about the homogeneity of the surface, but they do not prove the formation of the SAM.

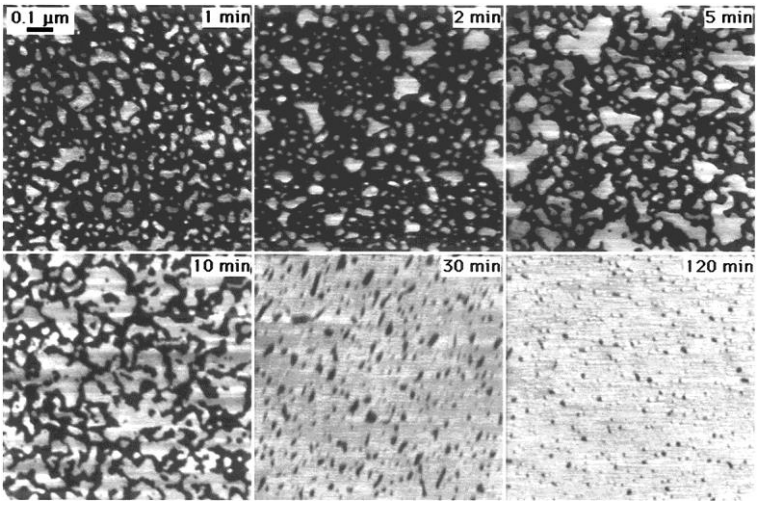

Figure 3 - AFM images of mica functionalized with alkanephosphonic acid at different stages of the SAM formation. The evolution from discrete domains to a complete monolayer can be observed. Figure reproduced from ref 35.

Vibrational spectroscopies (infrared reflection absorption spectroscopy – IRRAS–[65], Raman spectroscopy[66]) provide complementary information about the molecular composition, structure and interactions within a sample. These techniques measure vibrational energy levels, which are associated with the chemical bonds in the sample. IRRAS, is a surface based infrared spectroscopy which takes advantage of the grazing angle geometry, that allows an increase in the detection of functional groups perpendicular to the surface. When applied to SAM characterization it gives information about the functional groups present on the surface and their structure. In the particular case of alkylphosphonic acids SAM, IRRAS is used to determine the coordination mode of the phosphonic group to the surface by studying the change in the phosphonate frequency upon grafting.[67] Moreover, it is also useful to characterize the crystallinity and molecular tilt of the alkyl chains. This

information is extracted from the analysis of the frequency and intensity of the stretching modes of the methylene and methyl groups. The position (frequency) of both groups is related with the quality of the SAM (densely packed or liquid-like structure), while correspondent intensities give information about the tilting angle of the molecules.[68]

In Raman spectroscopy the sample is irradiated with monochromatic light and the photons are either inelastically or elastically scattered. The inelastically scattered light, known as Raman scatter, has lost (Stokes) or gained (Anti–Stokes) energy during this interaction and the emitted photon contains information about the molecular structure of the sample. The elastically scattered light has the same energy as the incident laser light and is called Rayleigh scatter. There is other requirement for a vibration to be Raman active, when the molecule vibrates there must be a change in polarisability i.e., a change in the shape, size or orientation of the electron cloud that surrounds the molecule. Raman spectroscopy can be used to gain additional chemical information, showing vibrations that are IR silent. Moreover, its higher spatial resolution, compared to IRRAS, allows us to perform surface mappings of particular functional groups.[69] In this work we will use the Raman Stokes scattering.

Electron/and X-ray based spectroscopies (Auger electron spectroscopy –AES–[70], X-ray photoelectron spectroscopy –XPS–[70] and synchrotron X-ray absorption spectroscopy –XAS–) can be used to get information about the elemental composition of SAMs, complementing the information obtained with previous techniques. In general, an excitation source such as X-rays, electrons or

synchrotron radiation will promote/eject an electron to/from an inner-shell orbital of an atom. XAS is based on the detection of photoelectrons that are promoted by X-rays, XPS relays on the detection of photoelectrons that are ejected by X-rays, and AES is based on the detection of electrons that are ejected from higher orbitals to conserve energy during electron transitions. All these spectroscopies are very surface sensitive, because their probe depth is related with the electron escape depth, which, in the typical energy range of these measurements (1 to 20 KeV), is only a few tens of nanometers.[70] In particular, XAS and XPS give information about the presence or absence of an element on the surface and also about its chemical oxidation state and chemical environment. In some cases, the attenuation of one element signal in XPS can be used to extract information about the thickness of the overlaying film.[71] Moreover, changing the incident beam-detector angle it is also possible to be more or less sensitive to a certain part of the monolayer.[72] AES, on the contrary, is less sensible to elemental oxidation state, but it is even more surface sensitive than XPS (specially for elements with low Z).[73] Additionally, with the scanning Auger electron spectroscopy (SAES) it is possible to combine the surface sensibility of AES with the spatial resolution of scanning electron microscopies. Characterization of magnetic materials can be also carried out by changing the polarization of the X-ray beam, varying from linear to circular polarized, which is translated in the enhancement or cancellation of the signal from a particular orbital.[46] Calculating the difference of the two XAS spectra, recorded with opposite polarizations, in presence of a magnetic field, it is possible to observe the X-ray magnetic circular dichroism (XMCD), that can be correlated with sample magnetic properties.

X-ray diffraction/reflection techniques (Grazing incidence X-ray diffraction -GIXRD- and X-ray reflectivity -XRR-) are used to study the molecular arrangement and packing and the thickness of a film deposited on a surface, respectively. GIXRD employs an incident X-ray beam using glancing incidence angle geometry to increase the sensitivity towards the diffraction signals. XRR employs specular reflection of X-rays, at very low angles (generally from 1° to 5°) to probe the electron density profile, at different depths of the film. Data can be modelled to extract parameters such as electron density, thickness and roughness of the slabs (layers of uniform density stacked adjacent to each other) that form a film.

As an example, we can refer to Wen *et al.*[74] about an organosilane SAM that underwent a post-assembly chemical modification process when the terminal group was changed from an alcohol to a carboxylic acid. GIXRD was used to determine the in-plane molecular arrangement and packing, which resulted to be hexagonal over all the reaction. XRR was used to determine the change in the film thickness as result of the transition from alcohol to carboxylic acid, while the backbone of the SAM did not suffer any change.

Mass spectrometry techniques (Time of flight secondary ions mass spectrometry -TOF-SIMS- and Matrix assisted laser desorption/ionization time of flight -MALDI-TOF-) are useful to analyze the surface composition by detecting the molecular peaks associated with the formed layers. TOF-SIMS uses an electron beam to extract secondary ions from the surface, which can be also used to acquire mappings of each species present on the surface. This feature makes this technique a common tool for surface characterization. Wolf

et al. [75] described the characterization of a SAM formed on gold with different chain length and resolved the metal-SAM complexes on the surface. MALDI-TOF MS is commonly used in the field of the proteomics to characterize crystallized proteins. This is a soft ionization technique that uses a polymer matrix, deposited on the surface, which is irradiated with a laser. The ionized matrix transfer protons to the molecules on the surface, allowing the detection of their mass, without causing fragmentation. Last developments in instrumentation have permitted to extend the limits of this technique to characterize thin films and SAMs. For example, Quiñones *et al.*[76] studied the functionalization of oxide surfaces with a family of alkylphosphonic acid (APA) SAMs and were able to differentiate between the formation of monolayer and multilayers . A full description of techniques such as AFM, IRRAS and XRR will be given in the Appendix.

1.3 Application of SAMs

SAMs find application, in many different fields nowadays. They can be used as a simple way to **control the wetting properties** of a surface, like in the case of the formation of superhydrophobic surfaces,[77] or in more complex applications like when they are used as a **scaffold for the anchoring and growth of other species**. This process can be driven by means of the formation of covalent bonds (i.e. SAMs with a terminal group bearing azide were used to bind acetyl group moieties through the azide-alkyne Huisgen cycloaddition reaction) [59], or through non-covalent interactions, like van der Waals and/or electrostatic forces, permitting the adsorption of surfactants, polymers or colloidal particles.[78–80] In this respect, SAMs can be also useful for **biochemical and**

biological purposes, to study the cell-substrate and biomolecule substrate interactions. Mrkisch et al. [81] have performed studies that control the specific interaction between adherent cells and SAM modified electrodes. Electrochemical pulses were used to reduce or oxidize the terminal groups of the SAM in order to attach or to release the chemical moieties that are responsible of the substrate recognition. Regarding synthetic chemistry, SAM modified substrates have been used **to obtain oriented crystal growth**, taking advantage of the oriented projections of the terminal functional groups. Crystals of many different materials have been grown including proteins, enantiomerically pure amino acids and semiconductors. [82–84]

Another important application of SAMs is their use as **protective layer** for the control of tribological, lubricant, wear and fouling properties, and more specifically as **etch resistant layers** for the formation of patterned surfaces. Whitesides et al.[85] made microstructured alkanethiolate SAMs on gold using microcontact printing (μCP). This technique relies on the use of polymeric stamps made of polydimethylsiloxane (PDMS), imbibed with solutions of the molecule to deposit. When the stamp is contacted with the surface, a SAM is formed only on the surface regions that are in direct contact with the stamp. If the functionalized substrate is then exposed to an etching solution - for example potassium cyanide in the case of gold surfaces - non-functionalized areas will be etched away, leaving behind the patterned structure on the surface (Figure 4).

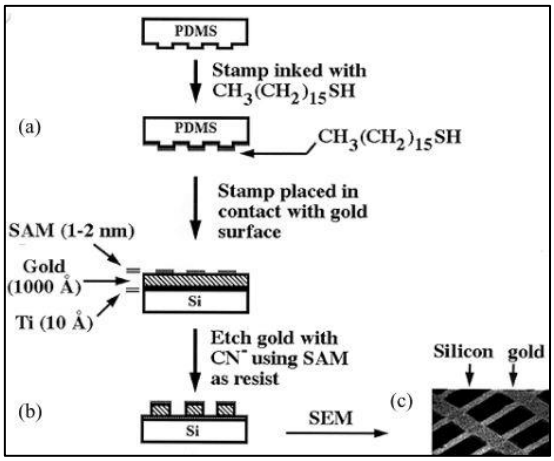

Figure 4 – Schematic representation of the microcontact printing and wet-chemical etching processes used to microstructure < 1 µm Si features. Figure reproduced from reference 85.

Similar ideas have also led to the investigation of SAMs as **electrode modifiers** in electrochemistry applications. SAMs can act as barriers that prevent the diffusion of electroactive species to the surface of the electrode.[86] For example during the electrochemical metal deposition on SAM modified electrodes, SAMs can be used as **molds** to generate metal-metal structures.[87] When insulating SAMs are used, metal deposition will take place on the non-covered regions of the electrode.[88]

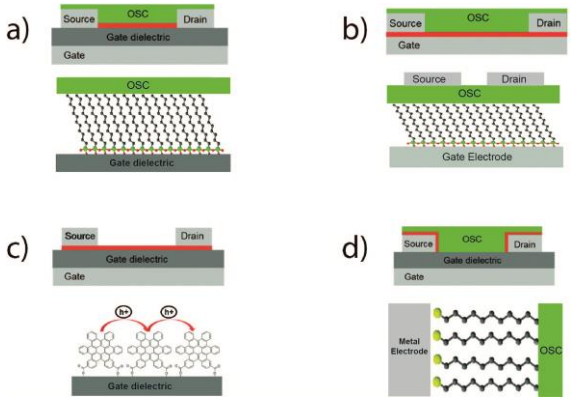

Figure 5 - Schematic cross-section representation of bottom–gate top–contact OFETs integrating a SAM that plays different roles: (a) gate dielectric primer, (b) molecular dielectric, (c) organic semiconductor and (d) electrode modifier. Figure adapted from reference 93

SAMs have also found wide application in the area of molecular electronics (Figure 5). They can be grafted on top of the **gate dielectric** to reduce traps and optimize the morphology and the structure of the semiconducting layer in organic field effect transistors (OFETs).[89] They can be also used to tune band alignment in light emitting diodes (LEDs), for example, modification of ITO electrodes with alkylphosphonic acids results in a more efficient charge injections to the organic semiconductor layer.[90] Moreover, SAMs can be used as **active electronic components**. For example, SAMs with saturated backbones can work as nanometer-thick and high capacitance dielectrics.[57,91] Alternatively, if π-conjugated SAM are used, they can work as semiconducting layers.[92] An interesting review on the theme was published by Casalini et al.[93]

In conclusion, SAMs represent the paradigm of bottom-up nanotechnology . Thanks to their modular design and ease of processing, they are capable to

build up architectures integrated at multiple scales and are versatile materials that have found wide applicability in very different fields.

1.4 SAMs application in spintronics

Going one step further from electronics, spintronics, which derives from the contraction of the words spin and electronics, is a research field where the spin of the electron together with its charge are used to transfer and process information. In this scenario, molecular species aims to complement, or even substitute, the inorganic materials traditionally used in spintronics. The next paragraphs will be focused on spintronics, since one of the aims of this thesis is the development of grafting protocols for the growth of SAMs over ferromagnetic materials to tune the interfaces of spintronic devices.

1.4.1. Basis of Spintronics

The simplest spintronic device consists on a non-magnetic spacer sandwiched between two ferromagnetic electrodes showing different coercive fields. Depending on the electrical nature of this spacer, the device will be called spin-valve (SV), in the case of a semiconductor, while it will be dubbed as magnetic tunnel junction (MTJ), in the case of an insulator.

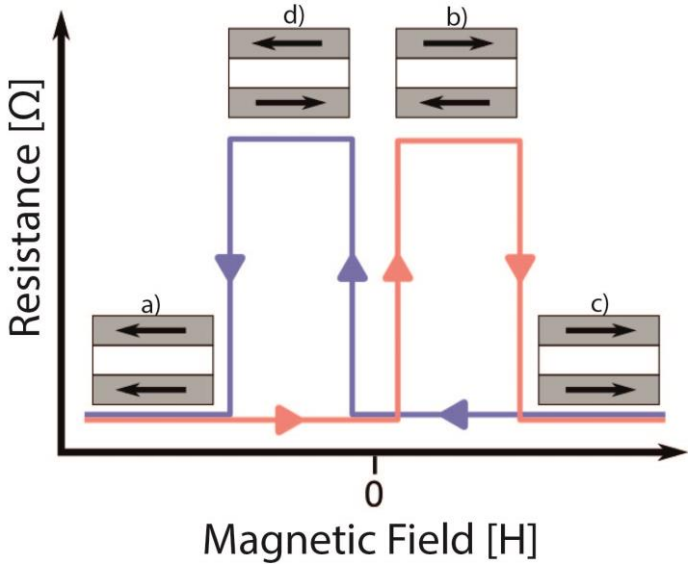

Figure 6 - Pictorial representation of a Resistance vs Magnetic Field (R(H)) measurements in a generic spintronic device: a) The magnetization in both electrodes is parallel, resulting in a low resistance; b) the magnetic field is swept till the magnetization of one of the electrodes (the softer one) changes its orientation, resulting in an antiparallel configuration, characterized with a higher resistance; c) the magnetic field is swept till the magnetization of the other electrode (the harder one) changes, returning to a parallel configuration, resulting again in low resistance and d) the cycle is closed by sweeping the magnetic field in the reverse direction to return to a).

The working principle for the two devices is the same. When a voltage is applied, a spin polarized current is generated in the device, and its magnitude will depend on the relative orientation of the ferromagnetic electrodes. The current will flow easily through the spacer (case of semiconductors) or tunnel through it (case of nanometric thick insulating barriers) when the magnetization of the electrodes is parallel. If the coercive field of the two ferromagnetic electrodes is different, applying an external magnetic field it is possible to control the relative orientation of the magnetization of the two electrodes (Figure 6). This will result in lower currents flowing through the

spacer/barrier when the magnetization of the electrodes is antiparallel. To guarantee the selective switch of the magnetization of the electrodes different materials can be used: Lanthanum Strontium Manganite Oxide (LSMO), Cobalt (Co), Nickel (Ni), Iron (Fe) and their alloys as Permalloy (NiFe alloy or Py) or Cobalt Iron Boron (CoFeB), for instance.

The first example of spin valve was reported independently by Fert[94] and Grünberg[95] in the late 80's, when they were working with artificial thin-film materials composed of alternate ferromagnetic and non-magnetic metallic layers, such as Fe/Cr. These systems exhibited very large changes of resistance, in the order of 10-15% at room temperature, as a function of the relative magnetization of the ferromagnetic layers in response to an external magnetic field. This phenomenon was dubbed giant magnetoresistance effect (GMR), which allowed in 2007 Fert and Grünberg to be awarded with the Nobel Prize in physics.

In the late 90's, the area witnessed the first commercial application of this effect when the first GMR-based read-write hard disk heads, developed by Parkin in IBM, were released to the market and lead to the successful fabrication of the 16.8 Gigabyte hard disk memory.[96]

MTJs are based on a phenomenon analogous to the GMR, dubbed tunnel magneto resistance (TMR). It was already postulated by Julliere[97] in the 1975, who directly related the changes in resistance observed with the two configurations of the electrodes (antiparallel and parallel). But, it was not until the 90's, when very thin alumina oxide layers were available that MTJs became popular. Resistance changes in the order of 70% were reported by Miyazaki.[98]

More recently, it was demonstrated that if alumina is replaced by magnesium oxide, TMR values as high as 2000% could be achieved.[99] These days, application of TMR can be found in magnetic random access memories[100] and in new generation storage technologies like solid state disk memories.[101]

1.4.2. Molecular Spintronics

Organic molecules are flexible, lightweight and can be designed at will finely tuning their properties using chemical synthesis. Thus, their electronic properties and their functionalities span an extremely large range. Moreover, since organic materials are made from light-weight elements, both spin-orbit and hyperfine interactions, the two principal ways for spins depolarization, are weak.[102] As a result, organic materials are characterized by their ability to sustain long-living spin states. These facts have stimulated the potential implementation of molecules in spintronics, an area that had been traditionally dominated by inorganic materials.

The contributions by Dediu et al.[103] in 2002 and by Vardeny et al.[104] in 2004, officially gave birth to the field of organic/molecular spintronics. The first group developed a lateral spin valve using as ferromagnetic electrodes LSMO and sexithienyl (T_6) as organic spacer. A magnetoresistance effect was observed having a maximum of 30 % at room temperature. The second group developed a vertical organic spin valve, using LSMO and Cobalt as electrodes, separated by Tris(8-hydroxyquinoline)aluminium(III) (Alq3), which is an organic semiconductor widely used in organic light emitting diodes (OLEDs). A negative magnetoresistance effect of 40% at 11K was measured.

More recently, a new research line dubbed as spinterface has arisen in the field of molecular spintronics.[105,106] When an organic molecule is put in contact with a ferromagnetic electrode, a mixing of the energy levels takes place. Such hybridization is characteristic to organic-inorganic interfaces and can alter the magnetoresistance signal, often giving an inversion of its sign.

1.4.3. SAMs in spintronics

As we introduced before, SAMs have interesting properties such as nanometer thickness, tight close packing, flexibility and lightweight. These reasons make them ideal candidates as toy-barriers in spintronic applications. We would like to highlight two pioneering works on spintronics with SAMs. Both of them based on the use of alkanethiol SAMs and ferromagnetic metals.

The first example was reported by Petta et al.[107] who prepared a spintronic device functionalizing a nickel bottom electrode with an octanethiol SAM, deposited from diluted ethanol solutions. In order to avoid short-circuits, they decreased the size of the device by scaling down the area of the contact, fabricating a pore in the range of 5-10 nanometers (Figure 7a), where the SAM grows. The samples were characterized at 4.2 K and showed up to 16% of TMR with low bias voltages (5 mV) (Figure 7b).

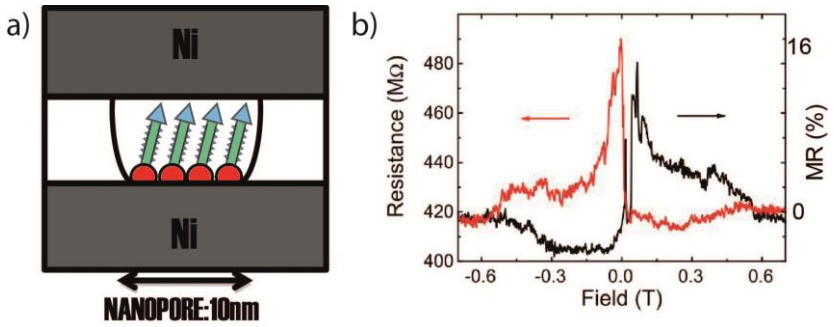

Figure 7 - a) Scheme of the MTJ used by Petta. b) R(H) measurement done at 4.2 K with 5 mV bias, showing 16% of TMR. Figure adapted from reference 107.

Another example was reported by Wang et *al.* in 2006, [108] they used the same geometry as Petta, changing the top electrode from nickel to cobalt (Figure 8a). The sample was measured at 4.2 K and showed an ambiguous change in resistance (Figure 8b).

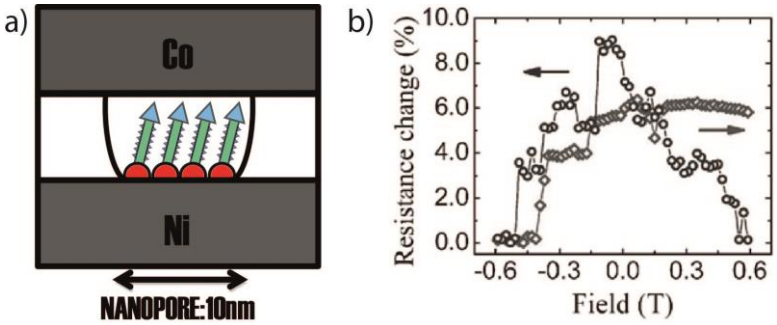

Figure 8 - a) Scheme of the MTJ used by Wang. b) R(H) measurement done at 4.2 K with 10 mV bias, showing 10% of TMR. Figure adapted from reference 108.

In both cases, magnetoresistance signals were low and not very clear. This fact can be attributed to the presence of some oxide on the nickel bottom electrode, which can be the source of a spin polarization loss of the electron tunnel current.

In order to overcome this drawback, Galbiati et *al.* some years later changed the bottom electrode from nickel to LSMO, which is an air-stable half metallic perovskite that is fully spin polarized at low temperature, but that loses it when approaching room temperature.[109] They reported the fabrication of a MTJ,[110,111] where long chain alkylphosphonic acids SAMs (C12P and C18P) were grafted on LSMO and used cobalt as the top electrode. In this case, in order to minimize the statistic of short-circuits, nanoindented contacts with 20 nm size were fabricated using AFM (Figure 9a). The sample was characterized down to 4K at different bias voltage (Figure 9b). TMR was observed ranging from 35% at 10 mV, down to 17% at 2 V.

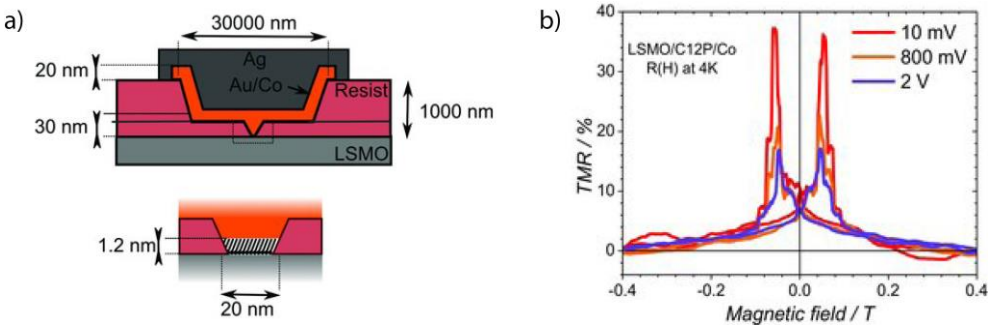

Figure 9 - a) Scheme of the MTJ used by Galbiati et al. . b) R(H) measurement done at 4 K at different bias voltages: 10 mV (red), 800 mV (orange) and 2 V (blue). Figure adapted from reference 111.

1.5 References

1. Ulman, A. Formation and Structure of Self-Assembled Monolayers. *Chem. Rev.* **96,** 1533–1554 (1996).

2. Sagiv, J. Organized monolayers by adsorption. 1. Formation and structure of oleophobic mixed monolayers on solid surfaces. *J. Am. Chem. Soc.* **102,** 92–98 (1980).

3. Fadeev, A. Y., Helmy, R. & Marcinko, S. Self-Assembled Monolayers of Organosilicon Hydrides Supported on Titanium, Zirconium, and Hafnium Dioxides. *Langmuir* **18,** 7521–7529 (2002).

4. Helmy, R. & Fadeev, A. Y. Self-Assembled Monolayers Supported on TiO2 : Comparison of C18H37SiX3 (X = H, Cl, OCH3), C18H37Si(CH3)2Cl, and C18H37PO(OH)2. *Langmuir* **18,** 8924–8928 (2002).

5. Pruna, R. *et al.* Organosilane-functionalization of nanostructured indium tin oxide films. *Interface Focus* **6,** 20160056 (2016).

6. Gao, W., Dickinson, L., Grozinger, C., Morin, F. G. & Reven, L. Self-Assembled Monolayers of Alkylphosphonic Acids on Metal Oxides. *Langmuir* **12,** 6429–6435 (1996).

7. Kanta, A., Sedev, R. & Ralston, J. The formation and stability of self-assembled monolayers of octadecylphosphonic acid on titania. *Colloids Surfaces A Physicochem. Eng. Asp.* **291,** 51–58 (2006).

8. Acton, O. *et al.* Simultaneous modification of bottom-contact electrode

and dielectric surfaces for organic thin-film transistors through single-component spin-cast monolayers. *Adv. Funct. Mater.* **21,** 1476–1488 (2011).

9. Zhang, B. *et al.* Surface Functionalization of Zinc Oxide by Carboxyalkylphosphonic Acid Self-Assembled Monolayers. *Langmuir* **26,** 4514–4522 (2010).

10. Lomoschitz, C. J. *et al.* Directing Alkyl Chain Ordering of Functional Phosphorus Coupling Agents on ZrO<sub>2<\sub>. *Langmuir* **27,** 3534–3540 (2011).

11. Bardecker, J. A. *et al.* Self-assembled Electroactive Phosphonic Acids on ITO: Maximizing Hole-Injection in Polymer Light-Emitting Diodes. *Adv. Funct. Mater.* **18,** 3964–3971 (2008).

12. Mutin, P. H., Guerrero, G. & Vioux, A. Hybrid materials from organophosphorus coupling molecules. *J. Mater. Chem.* **15,** 3761–3768 (2005).

13. Vioux, A., Bideau, J., Mutin, P. H. & Leclercq, D. in *New Aspects in Phosphorus Chemistry IV* (ed. Majoral, J.-P.) 145–174 (Springer Berlin Heidelberg, 2004). doi:10.1007/b13781

14. Hanson, E. L., Schwartz, J., Nickel, B., Koch, N. & Danisman, M. F. Bonding Self-Assembled, Compact Organophosphonate Monolayers to the Native Oxide Surface of Silicon. *J. Am. Chem. Soc.* **125,** 16074–16080 (2003).

15. Kang, M. S., Ma, H., Yip, H. L. & Jen, A. K. Y. Direct surface functionalization of indium tin oxide via electrochemically induced assembly. *J. Mater. Chem.* **17,** 3489–3492 (2007).

16. Liakos, I. L., Newman, R. C., McAlpine, E. & Alexander, M. R. Comparative study of self-assembly of a range of monofunctional aliphatic molecules on magnetron-sputtered aluminium. *Surf. Interface Anal.* **36,** 347–354 (2004).

17. Silverman, B. M., Wieghaus, K. A. & Schwartz, J. Comparative Properties of Siloxane vs Phosphonate Monolayers on A Key Titanium Alloy. *Langmuir* **21,** 225–228 (2005).

18. Taylor, C. E. & Schwartz, D. K. Octadecanoic Acid Self-Assembled Monolayer Growth at Sapphire Surfaces. *Langmuir* **19,** 2665–2672 (2003).

19. Liascukiene, I., Aissaoui, N., Asadauskas, S. J., Landoulsi, J. & Lambert, J.-F. Ordered Nanostructures on a Hydroxylated Aluminum Surface through the Self-Assembly of Fatty Acids. *Langmuir* **28,** 5116–5124 (2012).

20. Han, S. W., Lee, S. J. & Kim, K. Self-Assembled Monolayers of Aromatic Thiol and Selenol on Silver: Comparative Study of Adsorptivity and Stability. *Langmuir* **17,** 6981–6987 (2001).

21. Shaporenko, A., Ulman, A., Terfort, A. & Zharnikov, M. Self-Assembled Monolayers of Alkaneselenolates on (111) Gold and Silver. *J. Phys. Chem. B* **109,** 3898–3906 (2005).

22. Chen, H.-G. *et al.* Self-assembled Monolayers of n-Hexadecanoic Acid and

α-Hydroxyl n-Hexadecanoic Acid on Titanium Surfaces. *Chinese J. Chem.* **20,** 1467–1471 (2010).

23. Liu, Q., Ding, J., Mante, F. K., Wunder, S. L. & Baran, G. R. The role of surface functional groups in calcium phosphate nucleation on titanium foil: a self-assembled monolayer technique. *Biomaterials* **23,** 3103–3111 (2002).

24. Han, S. W. & Kim, K. Self-Assembled Monolayers of Organoselenium Compounds on Gold: Surface-Enhanced Raman Scattering Study. *J. Colloid Interface Sci.* **240,** 492–497 (2001).

25. Folkers, J. P. *et al.* Self-Assembled Monolayers of Long-Chain Hydroxamic Acids on the Native Oxide of Metals. *Langmuir* **11,** 813–824 (1995).

26. Aitchison, H. *et al.* Self-Assembled Monolayers of Oligophenylenecarboxylic Acids on Silver Formed at the Liquid–Solid Interface. *Langmuir* **32,** 9397–9409 (2016).

27. Laibinis, P. E. *et al.* Comparison of the structures and wetting properties of self-assembled monolayers of n-alkanethiols on the coinage metal surfaces, copper, silver, and gold. *J. Am. Chem. Soc.* **113,** 7152–7167 (1991).

28. Alloway, D. M. *et al.* Tuning the Effective Work Function of Gold and Silver Using ω-Functionalized Alkanethiols: Varying Surface Composition through Dilution and Choice of Terminal Groups. *J. Phys. Chem. C* **113,** 20328–20334 (2009).

29. Pellerite, M. J., Dunbar, T. D., Boardman, L. D. & Wood, E. J. Effects of Fluorination on Self-Assembled Monolayer Formation from Alkanephosphonic Acids on Aluminum: Kinetics and Structure. *J. Phys. Chem. B* **107,** 11726–11736 (2003).

30. Gao, W., Dickinson, L., Grozinger, C., Morin, F. G. & Reven, L. Self-Assembled Monolayers of Alkylphosphonic Acids on Metal Oxides. *Langmuir* **12,** 6429–6435 (1996).

31. Caipa Campos, M. A. *et al.* Self-Assembled Functional Organic Monolayers on Oxide-Free Copper. *Langmuir* **27,** 8126–8133 (2011).

32. Lewington, T. A., Alexander, M. R., Thompson, G. E. & McAlpine, E. Characterisation of alkyl phosphonic acid monolayers self assembled on hydrated surface of aluminium. *Surf. Eng.* **18,** 228–232 (2002).

33. Hoertz, P. G., Niskala, J. R., Dai, P., Black, H. T. & You, W. Comprehensive Investigation of Self-Assembled Monolayer Formation on Ferromagnetic Thin Film Surfaces. *J. Am. Chem. Soc.* **130,** 9763–9772 (2008).

34. Volmer, M., Stratmann, M. & Viefhaus, H. Electrochemical and electron spectroscopic investigations of iron surfaces modified with thiols. *Surf. Interface Anal.* **16,** 278–282 (1990).

35. Woodward, J. T., Ulman, A. & Schwartz, D. K. Self-Assembled Monolayer Growth of Octadecylphosphonic Acid on Mica. *Langmuir* **12,** 3626–3629 (1996).

36. Magnussen, O. M. *et al.* Self-assembly of organic films on a liquid metal.

Nature **384,** 250–252 (1996).

37. Muskal, N., Turyan, I. & Mandler, D. Self-assembled monolayers on mercury surfaces. *J. Electroanal. Chem.* **409,** 131–136 (1996).

38. Jo, K., Yu, H.-Z. & Yang, H. Formation kinetics and stability of phosphonate self-assembled monolayers on indium–tin oxide. *Electrochim. Acta* **56,** 4828–4833 (2011).

39. Mekhalif, Z., Laffineur, F., Couturier, N. & Delhalle, J. Elaboration of Self-Assembled Monolayers of n-Alkanethiols on Nickel Polycrystalline Substrates: Time, Concentration, and Solvent Effects. *Langmuir* **19,** 637–645 (2003).

40. Mekhalif, Z., Riga, J., Pireaux, J.-J. & Delhalle, J. Self-Assembled Monolayers of n-Dodecanethiol on Electrochemically Modified Polycrystalline Nickel Surfaces. *Langmuir* **13,** 2285–2290 (1997).

41. Love, J. C. *et al.* Formation and Structure of Self-Assembled Monolayers of Alkanethiolates on Palladium. *J. Am. Chem. Soc.* **125,** 2597–2609 (2003).

42. Love, J. C., Wolfe, D. B., Chabinyc, M. L., Paul, K. E. & Whitesides, G. M. Self-Assembled Monolayers of Alkanethiolates on Palladium Are Good Etch Resists. *J. Am. Chem. Soc.* **124,** 1576–1577 (2002).

43. Li, Z., Chang, S.-C. & Williams, R. S. Self-Assembly of Alkanethiol Molecules onto Platinum and Platinum Oxide Surfaces. *Langmuir* **19,** 6744–6749 (2003).

44. Laiho, T. *et al.* Chemisorption of alkyl thiols and S-alkyl thiosulfates on Pt(111) and polycrystalline platinum surfaces. *Surf. Sci.* **584,** 83–89 (2005).

45. Devillers, S., Hennart, A., Delhalle, J. & Mekhalif, Z. 1-Dodecanethiol Self-Assembled Monolayers on Cobalt. *Langmuir* **27,** 14849–14860 (2011).

46. Pookpanratana, S., Lydecker, L. K., Richter, C. A. & Hacker, C. A. Self-assembled monolayers impact cobalt interfacial structure in nanoelectronic junctions. *J. Phys. Chem. C* **119,** 6687–6695 (2015).

47. Koide, Y. *et al.* Hot Microcontact Printing for Patterning ITO Surfaces. Methodology, Morphology, Microstructure, and OLED Charge Injection Barrier Imaging. *Langmuir* **19,** 86–93 (2003).

48. Tang, X., Schneider, T. W., Walker, J. W. & Buttry, D. A. Dimerized π-Complexes in Self-Assembled Monolayers Containing Viologens: An Origin of Unusual Wave Shapes in the Voltammetry of Monolayers. *Langmuir* **12,** 5921–5933 (1996).

49. Cavallini, M., Bracali, M., Aloisi, G. & Guidelli, R. Electrochemical STM Investigation of 1,8-Octanedithiol Self-Assembled Monolayers on Ag(111) in Aqueous Solution. *Langmuir* **15,** 3003–3006 (1999).

50. Steinrück, H.-G., Will, J., Magerl, A. & Ocko, B. M. Structure of n -Alkyltrichlorosilane Monolayers on Si(100)/SiO 2. *Langmuir* **31,** 11774–11780 (2015).

51. Nuzzo, R. G. & Allara, D. L. Adsorption of bifunctional organic disulfides on gold surfaces. *J. Am. Chem. Soc.* **105,** 4481–4483 (1983).

52. Henderson, J. I., Feng, S., Ferrence, G. M., Bein, T. & Kubiak, C. P. Self-assembled monolayers of dithiols, diisocyanides, and isocyanothiols on gold: 'chemically sticky' surfaces for covalent attachment of metal clusters and studies of interfacial electron transfer. *Inorganica Chim. Acta* **242,** 115–124 (1996).

53. Zhang, F. *et al.* Preparation of superhydrophobic films on titanium as effective corrosion barriers. *Appl. Surf. Sci.* **257,** 2587–2591 (2011).

54. Porter, M. D., Bright, T. B., Allara, D. L. & Chidsey, C. E. D. Spontaneously organized molecular assemblies. 4. Structural characterization of n-alkyl thiol monolayers on gold by optical ellipsometry, infrared spectroscopy, and electrochemistry. *J. Am. Chem. Soc.* **109,** 3559–3568 (1987).

55. Li, Z., Chang, S.-C. & Williams, R. S. Self-Assembly of Alkanethiol Molecules onto Platinum and Platinum Oxide Surfaces. *Langmuir* **19,** 6744–6749 (2003).

56. Tour, J. M. *et al.* Self-Assembled Monolayers and Multilayers of Conjugated Thiols, .alpha.,.omega.-Dithiols, and Thioacetyl-Containing Adsorbates. Understanding Attachments between Potential Molecular Wires and Gold Surfaces. *J. Am. Chem. Soc.* **117,** 9529–9534 (1995).

57. Fontaine, P. *et al.* Octadecyltrichlorosilane monolayers as ultrathin gate insulating films in metal-insulator-semiconductor devices. *Appl. Phys. Lett.* **62,** 2256–2258 (1993).

58. Smits, E. C. P. *et al.* Bottom-up organic integrated circuits. *Nature* **455,**

956–959 (2008).

59. Collman, J. P., Devaraj, N. K. & Chidsey, C. E. D. 'Clicking' Functionality onto Electrode Surfaces. *Langmuir* **20,** 1051–1053 (2004).

60. Yuan, Y. & Lee, T. R. Contact angle and wetting properties. *Springer Ser. Surf. Sci.* **51,** 3–34 (2013).

61. Laibinis, P. E. & Whitesides, G. M. Self-assembled monolayers of n-alkanethiolates on copper are barrier films that protect the metal against oxidation by air. *J. Am. Chem. Soc.* **114,** 9022–9028 (1992).

62. Sedev, R. V., Petrov, J. G. & Neumann, A. W. Effect of Swelling of a Polymer Surface on Advancing and Receding Contact Angles. *J. Colloid Interface Sci.* **180,** 36–42 (1996).

63. Binnig, G., Gerber, C., Stoll, E., Albrecht, T. R. & Quate, C. F. Atomic Resolution with Atomic Force Microscope. *Europhys. Lett.* **3,** 1281–1286 (1987).

64. Moores, B., Simons, J., Xu, S. & Leonenko, Z. AFM-assisted fabrication of thiol SAM pattern with alternating quantified surface potential. *Nanoscale Res. Lett.* **6,** 185 (2011).

65. Mendelsohn, R., Mao, G. & Flach, C. R. Infrared reflection-absorption spectroscopy: principles and applications to lipid-protein interaction in Langmuir films. *Biochim. Biophys. Acta* **1798,** 788–800 (2010).

66. Evans, S. D., Freeman, T. L., Flynn, T. M., Batchelder, D. N. & Ulman, A.

Raman spectroscopy of self-assembled mono- and multilayer films of alkanethiolate on gold. *Thin Solid Films* **244,** 778–783 (1994).

67. Foster, T. T., Alexander, M. R., Leggett, G. J. & McAlpine, E. Friction force microscopy of alkylphosphonic acid and carboxylic acids adsorbed on the native oxide of aluminum. *Langmuir* **22,** 9254–9259 (2006).

68. Greenler, R. G. Infrared Study of Adsorbed Molecules on Metal Surfaces by Reflection Techniques. *J. Chem. Phys.* **44,** 310–315 (1966).

69. Yang, H. *et al.* Self-assembled monolayer of NAD at silver surface: a Raman mapping study. *Surf. Sci.* **551,** 1–8 (2004).

70. Baer, D. R., Engelhard, M. H. & Lea, A. S. Introduction to Surface Science Spectra data on electron and x-ray damage: Sample degradation during XPS and AES measurements. *Surf. Sci. Spectra* **10,** 47–56 (2005).

71. McGuiness, C. L. *et al.* Molecular Self-Assembly at Bare Semiconductor Surfaces: Preparation and Characterization of Highly Organized Octadecanethiolate Monolayers on GaAs(001). *J. Am. Chem. Soc.* **128,** 5231–5243 (2006).

72. Shogen, S., Kawasaki, M., Kondo, T., Sato, Y. & Uosaki, K. Structural study of self-assembled monolayers of ferrocenylalkanethiols on gold by angleresolved X-ray photoelectron spectroscopy. *Appl. Organomet. Chem.* **6,** 533–536 (1992).

73. Azzaroni, O. *et al.* Electrodesorption Potentials of Self-Assembled Alkanethiolate Monolayers on Copper Electrodes. An Experimental and

Theoretical Study. *J. Phys. Chem. B* **107,** 13446–13454 (2003).

74. Wen, K. *et al.* Postassembly Chemical Modification of a Highly Ordered Organosilane Multilayer: New Insights into the Structure, Bonding, and Dynamics of Self-Assembling Silane Monolayers. *ACS Nano* **2,** 579–599 (2008).

75. Wolf, K. V., Cole, D. A. & Bernasek, S. L. High-Resolution TOF-SIMS Study of Varying Chain Length Self-Assembled Monolayer Surfaces. *Anal. Chem.* **74,** 5009–5016 (2002).

76. Quiñones, R., Raman, A. & Gawalt, E. S. An approach to differentiating between multi- and monolayers using MALDI-TOF MS. *Surf. Interface Anal.* **39,** 593–600 (2007).

77. Jabarullah, N. H. *et al.* Superhydrophobic SAM Modified Electrodes for Enhanced Current Limiting Properties in Intrinsic Conducting Polymer Surge Protection Devices. *Langmuir* **31,** 6253–6264 (2015).

78. Ko, B. S. *et al.* Effect of Surface Composition on the Adsorption of Photosystem I onto Alkanethiolate Self-Assembled Monolayers on Gold. *Langmuir* **20,** 4033–4038 (2004).

79. Brandani, P. & Stroeve, P. Kinetics of Adsorption and Desorption of PEO–PPO–PEO Triblock Copolymers on a Self-Assembled Hydrophobic Surface. *Macromolecules* **36,** 9502–9509 (2003).

80. Fendler, J. H. Chemical Self-assembly for Electronic Applications. *Chem. Mater.* **13,** 3196–3210 (2001).

81. Jiang, X., Ferrigno, R., Mrksich, M. & Whitesides, G. M. Electrochemical Desorption of Self-Assembled Monolayers Noninvasively Releases Patterned Cells from Geometrical Confinements. *J. Am. Chem. Soc.* **125,** 2366–2367 (2003).

82. Pham, T. *et al.* Well-ordered self-assembled monolayer surfaces can be used to enhance the growth of protein crystals. *Colloids Surfaces B Biointerfaces* **34,** 191–196 (2004).

83. Banno, N., Nakanishi, T., Matsunaga, M., Asahi, T. & Osaka, T. Enantioselective Crystal Growth of Leucine on a Self-Assembled Monolayer with Covalently Attached Leucine Molecules. *J. Am. Chem. Soc.* **126,** 428–429 (2004).

84. Jiang, P., Liu, Z.-F. & Cai, S.-M. Growing Monodispersed PbS Nanoparticles on Self-Assembled Monolayers of 11-Mercaptoundecanoic Acid on Au(111) Substrate. *Langmuir* **18,** 4495–4499 (2002).

85. Wilbur, J. L., Kumar, A., Biebuyck, H. A., Kim, E. & Whitesides, G. M. Microcontact printing of self-assembled monolayers: applications in microfabrication. *Nanotechnology* **7,** 452–457 (1996).

86. Chidsey, C. E. & Murray, R. W. Electroactive polymers and macromolecular electronics. *Science* **231,** 25–31 (1986).

87. Schilardi, P. L., Azzaroni, O. & Salvarezza, R. C. A Novel Application of Alkanethiol Self-Assembled Monolayers in Nanofabrication: Direct Molding and Replication of Patterned Conducting Masters. *Langmuir* **17,**

2748–2752 (2001).

88. Boyen, H.-G. *et al.* Local density of states effects at the metal-molecule interfaces in a molecular device. *Nat. Mater.* **5,** 394–399 (2006).

89. Weitz, R. T. *et al.* Highly Reliable Carbon Nanotube Transistors with Patterned Gates and Molecular Gate Dielectric. *Nano Lett.* **9,** 1335–1340 (2009).

90. Stoliar, P. *et al.* Charge Injection Across Self-Assembly Monolayers in Organic Field-Effect Transistors: Odd–Even Effects. *J. Am. Chem. Soc.* **129,** 6477–6484 (2007).

91. Bobbert, P. A., Sharma, A., Mathijssen, S. G. J., Kemerink, M. & de Leeuw, D. M. Operational Stability of Organic Field-Effect Transistors. *Adv. Mater.* **24,** 1146–1158 (2012).

92. Briseno, A. L. *et al.* Oligo- and Polythiophene/ZnO Hybrid Nanowire Solar Cells. *Nano Lett.* **10,** 334–340 (2010).

93. Casalini, S., Bortolotti, C. A., Leonardi, F. & Biscarini, F. Self-assembled monolayers in organic electronics. *Chem. Soc. Rev.* **46,** 40–71 (2017).

94. Baibich, M. N. *et al.* Giant magnetoresistance of (001)Fe/(001)Cr magnetic superlattices. *Phys. Rev. Lett.* **61,** 2472–2475 (1988).

95. Barnaś, J., Fuss, A., Camley, R. E., Grünberg, P. & Zinn, W. Novel magnetoresistance effect in layered magnetic structures: Theory and experiment. *Phys. Rev. B* **42,** 8110–8120 (1990).

96. Parkin, S. S. P. Giant Magnetoresistance in Magnetic Nanostructures. *Annu. Rev. Mater. Sci.* **25,** 357–388 (1995).

97. Julliere, M. Tunneling between ferromagnetic films. *Phys. Lett. A* **54,** 225–226 (1975).

98. Miyazaki, T. & Tezuka, N. Giant magnetic tunneling effect in Fe/Al2O3/Fe junction. *J. Magn. Magn. Mater.* **139,** L231–L234 (1995).

99. Liu, H. *et al.* Giant tunneling magnetoresistance in epitaxial $Co_2MnSi/MgO/Co_2MnSi$ magnetic tunnel junctions by half-metallicity of Co_2MnSi and coherent tunneling. *Appl. Phys. Lett.* **101,** 132418 (2012).

100. Chen, E. *et al.* Advances and Future Prospects of Spin-Transfer Torque Random Access Memory. *IEEE Trans. Magn.* **46,** 1873–1878 (2010).

101. Parkin, S. & Yang, S.-H. Memory on the racetrack. *Nat. Nanotechnol.* **10,** 195–198 (2015).

102. Sanvito, S. Molecular spintronics. *Chem. Soc. Rev.* **40,** 3336–3355 (2011).

103. Dediu, V., Murgia, M., Matacotta, F. C., Taliani, C. & Barbanera, S. Room temperature spin polarized injection in organic semiconductor. *Solid State Commun.* **122,** 181–184 (2002).

104. Xiong, Z. H., Wu, D., Valy Vardeny, Z. & Shi, J. Giant magnetoresistance in organic spin-valves. *Nature* **427,** 821–824 (2004).

105. Sanvito, S. Molecular spintronics: The rise of spinterface science. *Nat. Phys.* **6,** 562–564 (2010).

106. Galbiati, M. *et al.* Spinterface: Crafting spintronics at the molecular scale. *MRS Bull.* **39,** 602–607 (2014).

107. Petta, J. R., Slater, S. K. & Ralph, D. C. Spin-dependent transport in molecular tunnel junctions. *Phys. Rev. Lett.* **93,** 136601 (2004).

108. Wang, W. & Richter, C. A. Spin-polarized inelastic electron tunneling spectroscopy of a molecular magnetic tunnel junction. *Appl. Phys. Lett.* **89,** 153103–153105 (2006).

109. Bowen, M. *et al.* Using half-metallic manganite interfaces to reveal insights into spintronics. *J. Phys. Condens. Matter* **19,** 315208 (2007).

110. Tatay, S. *et al.* Self-Assembled Monolayer-Functionalized Half-Metallic Manganite for Molecular Spintronics. *ACS Nano* **6,** 8753–8757 (2012).

111. Galbiati, M. *et al.* Unveiling self-assembled monolayers' potential for molecular spintronics: Spin transport at high voltage. *Adv. Mater.* **24,** (2012).

2 Self-assembled monolayers on Permalloy

2.1. Introduction

One of the main objectives of this thesis was the development of functionalization protocols for FM surfaces. In a first step, we decided to undertake the study of Permalloy (Py) because it is a common material used in spintronics, for which no functionalization had been reported so far in literature.

Py is a FM nickel-iron alloy, composed of about around 80% of nickel and 20% of iron, characterized by having a Curie temperature of 723K, high magnetic permeability, small coercivity, near zero magnetostriction and significant anisotropic magnetoresistance (AMR).[1,2] It is commercially available and it is commonly used in spintronic devices like hard disk magnetic recording heads or magnetoresistive random-access memories (MRAM).[3] Under air atmosphere, Py reacts developing a thin passivating layer composed of a mixture of iron and nickel oxides and hydroxides, which protects the bulk from further oxidation. This behavior is common to other metals like aluminum,[4] cobalt[5] or copper.[6]

The exact nature of Py oxide depends on the oxidation conditions, e.g.: oxygen pressure,[7] temperature,[8] atmospheric conditions[9] or nature of the oxidation process (electrochemical[10] or plasma oxidation[11]). From the magnetic point of view, this oxide is an antiferromagnet (AF) with a Neel temperature of 193K. Below this temperature, the presence of the AF layer results in effective exchange bias interactions with the undelaying bulk FM Py.[12,13]

As discussed in Chapter 1, the functionalization of transition metal oxides, such aluminium,[14] titanium[15] or chromium[16] oxides with SAMs has been traditionally based on the use of alkylphosphonic acids (APAs),[17] because phosphonic acids have been found to bind strongly to metal oxide surfaces and therefore are preferred over carboxylic acids.[18] Once grafted on the surface, these layers; if organized in patterns, can act as etching resist, protecting the surface and giving rise to microstructures.[19] Regarding FM metals, there is one example by Quiñones *et al.*[20] in 2008, that reports the functionalization of nickel oxide with a family of APAs, from octyl to octadecyl alkyl chains, using two different methods, the traditional immersion in solution and a novel spray coating technique, which relies on spraying the solution with an aerograph to reduce the deposition time. However, as pointed out above, neither the functionalization of Py, nor of its oxide, have been described in literature. In this chapter, we will present the functionalization of Py oxide surface with a family of APAs. The formed monolayers have been characterized by wCA, AFM, XPS, IRRAS and XRR. Additionally, the effect of the functionalization on the magnetic properties of the substrate has been carried out by means of magneto-optical Kerr effect spectroscopy (MOKE). Regarding their potential applicability, they have been prepared as patterned microstructures on the

surface using microcontact printing (μCP). Thanks to the high quality of the APA SAMs, they have been used as resistive masks towards etching agents. Finally, we will pointed out, how the growth of these SAMs has been determinant for the successful formation of a surface metal organic framework (surMOF) on a FM surface.

2.2. Results and discussion

2.2.1. Influence of the surface pre-treatment

As has been mentioned before, the composition of the outermost oxide layer in Py films depends on the oxidation conditions. In order to study the grafting of organic molecules on Py, it is important to investigate the chemical species present at the surface of the Py films and to understand if significant modifications after different cleaning/activation treatments take place. To fulfill this goal XPS, XRR and AFM analysis were performed.

The XPS survey spectra of a 40 nm Py film thermally evaporated on a silicon native oxide substrate (red), along with that of the same film after 60s Ar^+ milling (grey) are displayed on Figure 1. The first spectrum shows the presence of Ni, Fe, O and adventitious C, while the second one displays exclusively the presence of Ni and Fe, which confirmed that Ar^+ milling was successful in removing the native oxide, reaching the bulk and confirming that under the native oxide layer, unoxidized Py is still present.

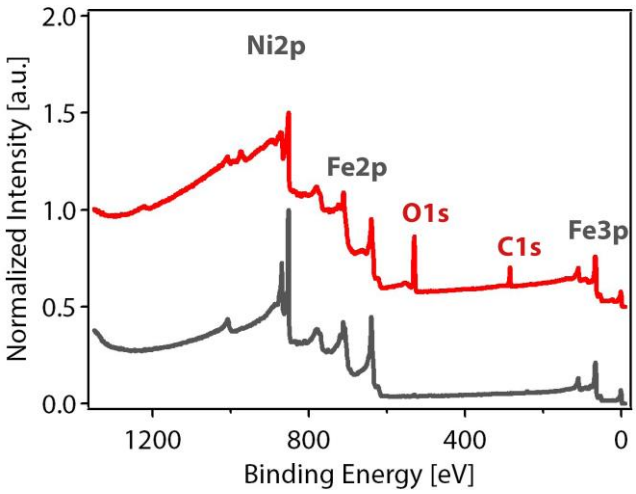

Figure 1 - XPS survey spectra of 40 nm air exposed Py sample (red) and after Ar+ milling (grey).

The High-resolution spectra at the Ni2p$_{3/2}$ and Fe3p$_{3/2}$ edges of the oxidized (red) and milled (gray) samples are displayed in Figure 2. Despite the fact that the spectrum at the Fe3p edge is less intense than at the Fe2p edge, during this study we focused on it, because the Fe2p edge strongly overlaps with Ni LMM Auger peaks, located between 706-709 eV. For the milled sample, both Ni and Fe spectra are consistent with the presence of the elements in their metallic states: a sharp peak at 852.6 and a satellite peaking at 858.6 eV compose the nickel signal,[21] while in the case of iron, the spectrum is characterized by an unresolved signal peaking at approximately 52.8 eV.[22,23] However, high-resolution Ni2p$_{3/2}$ and Fe3p$_{3/2}$ spectra (red line, Figure 2) of the air oxidized Py sample show signals coming from metallic Ni and Fe along with a contribution of species in higher oxidation states peaking above 855 eV and 56 eV respectively (Figure 2).

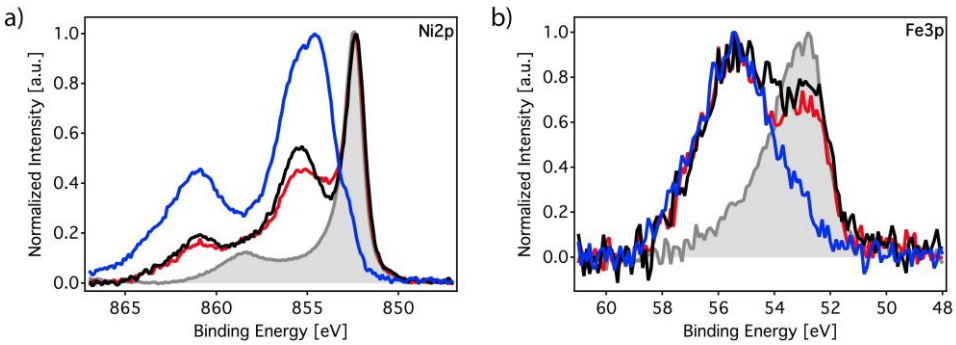

Figure 2 - High-resolution XPS spectra at the Ni2p$_{3/2}$ (a) and Fe3p$_{3/2}$ (b) edges of Py films subjected to different treatments: Ar$^+$ milling (reference, gray), air oxidation (no plasma, red), H$_2$ plasma (black), O$_2$ plasma (blue).

Next, we studied the effect of hydrogen and oxygen plasma treatments on our Py films. These kind of treatments have been commonly used on other oxides like alumina, with the twofold aim of cleaning the surface and increasing the density of binding sites thus promoting SAM formation.[24] XPS measurements revealed that the surface composition of O_2 and H_2 plasma–treated samples is significantly affected by this process. These changes are appreciable in the Ni2p$_{3/2}$ and Fe3p$_{3/2}$ spectra (Figure 2, black and blue lines) and especially in the O1s high-resolution XPS spectrum (Figure 3).

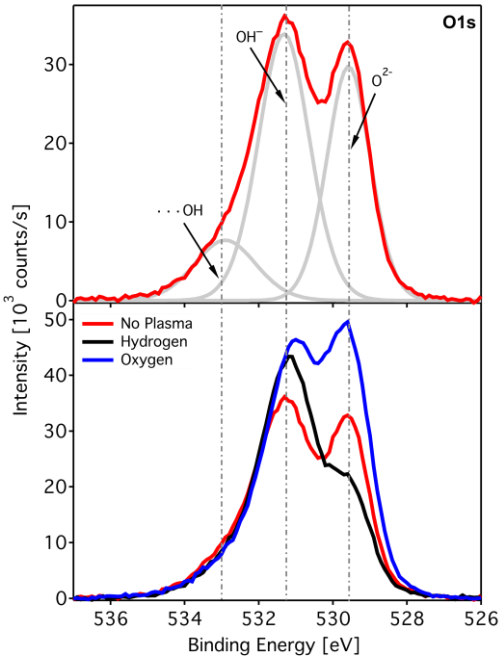

Figure 3 - Top: Deconvoluted high-resolution O1s XPS spectrum of an air oxidized Py film (red line) without any additional plasma treatment. Bottom: The upper spectrum is compared with those of Py films subjected to H_2 (black) and O_2 (blue) plasmas.

The top part of Figure 3 shows the O1s high-resolution XPS spectra of an air oxidized (no plasma) sample. In agreement with previous reports, the total spectrum results from the contribution of different oxygen species present in the sample: bulk (O^{2-}, 529.6 eV), hydroxyl (OH^-, 531.2 eV) and weakly bound oxygen species and contamination (532.9 eV).[25,22,26]

After the hydrogen plasma treatment, changes in the shape of the O1s spectrum are evident, with an increase of the signal coming from hydroxyl groups at the expense of that of bulk oxygen. This is consistent with the transformation of some metal oxide into hydroxide species. This marked

increase of the hydroxyl peak has not been observed in the case of the oxygen plasma treated sample. Nevertheless, in this later case, an overall increase in the O1s signal with respect to the non-treated sample is detected. These changes are accompanied by the disappearance of the metallic iron and nickel contributions in the Ni2p and Fe3p spectra (Figure 2, blue line) and point to the formation of a thicker Py oxide as a result of the oxygen plasma treatment.

We performed XRR measurements to evaluate the oxide thickness after the plasma treatments. The collected reflectivity curves are shown in Figure 4a; the model used to fit the curves is represented in Figure 4b. We fitted the data to a three-slab structure to obtain the density (ρ) and the thickness (T) of the Py and the Py oxide (PyOx) layers.

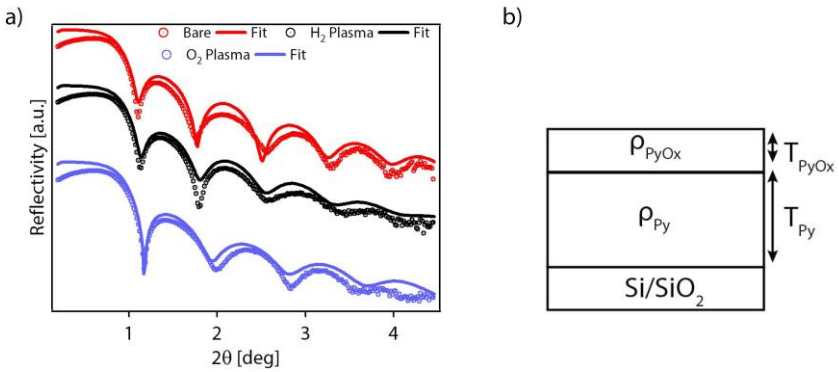

Figure 4 – a) XRR reflectograms of Py surface subjected to different treatments: bare sample (red dots), H_2 plasma (black dots) and O_2 plasma (blue dots). b) Model used to fit the curves.

The obtained results are listed in Table 1. These values seem to confirm the increase in the oxide thickness after the O_2 plasma treatment, while in the H_2 plasma treated sample no effective change is appreciable.

Table 1 – Parameters obtained from the fittings of XRR data of Py samples subjected to different treatments: ρ is the density and T is the thickness of each layer.

Sample	ρ_{PyOx} [g/cm^3]	T_{PyOx} [nm]	ρ_{Py} [g/cm^3]	T_{Py} [nm]
Bare	6.85	1.8	8.6	8.2
H_2 Plasma	6.74	1.7	8.6	8.3
O_2 Plasma	7.61	2.9	8.6	7.1

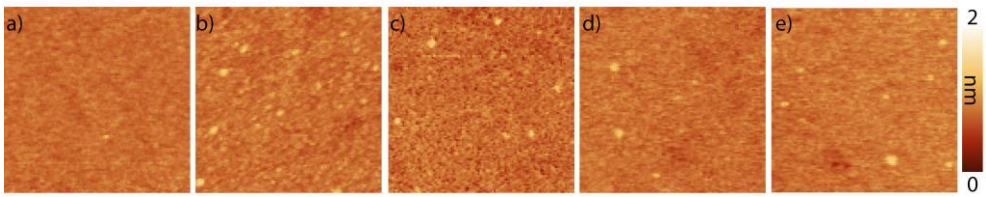

Figure 5 - AFM topographic images (1x1 μm^2) of Py substrates after different plasma treatments: a) air oxidized Py substrate, b) Weak H_2 Plasma, c) Strong H_2 Plasma, d) Weak O_2 Plasma, e) Strong O_2 Plasma.

Finally, we checked by AFM, the morphology of the treated samples (Figure 5). In spite of the difference in composition, plasma treatments do not lead the appreciable changes in the morphology of the surface with root mean square (RMS) roughness values around 0.16 nm, comparable to that of the air oxidized sample.

2.2.1 Preparation of SAMs

In the second part of our study we investigated how APAs of different carbon chain lengths ($CH_3(CH_2)_{n-1}PO_3H$ = CnP; n being number of C atoms) are anchored on Py substrates. We have used $w\theta_{CA}$ measurements to evaluate the extent and quality of the formed SAMs. Due to the hydrophobic character of alkyl chains used in this study, an increase in $w\theta_{CA}$ can be directly related with an

improvement of the quality of the SAM. During control experiments, we used Py samples exposed to the same surface pre-treatments but dipped in neat solvent as references. According to the literature, the best reported conditions to form good quality APAs SAMs over metal oxide surface were the use of 2 mM APA 2-propanol solutions.[27,28] In table 2 the $w\theta_{CA}$ values obtained using that functionalization conditions for the each different pretreatment are reported.

Table 2 - $w\theta_{CA}$ values for samples subjected to different treatments and functionalized with different APAs. Ø is the neat solvent.

Sample	$w\theta_{AA}$ [°]	$w\theta_{RA}$ [°]	Sample	$w\theta_{AA}$ [°]	$w\theta_{RA}$ [°]	Sample	$w\theta_{AA}$ [°]	$w\theta_{RA}$ [°]
Bare	40	12	**H_2 Plasma**	22	10	**O_2 Plasma**	18	10
Ø	45	15	**H_2-Ø**	48	19	**O_2-Ø**	40	12
C12P	90	77	**H_2-C12P**	107	80	**O_2-C12P**	44	17
C14P	94	80	**H_2-C14P**	109	87	**O_2-C14P**	46	19
C16P	98	85	**H_2-C16P**	112	92	**O_2-C16P**	52	20
C18P	100	87	**H_2-C18P**	116	95	**O_2-C18P**	50	21

As can be seen, the $w\theta_{CA}$ values of APA functionalized samples are always higher than those for the corresponding reference samples. In particular, $w\theta_{CA}$ values of the SAMs formed on H_2 plasma treated Py samples are higher than those measured for SAMs on O_2 or air oxidized samples. Moreover, they are comparable with those obtained by Allara *et al.*,[29] or Pellerite *et al.*[30] on alumina oxide or Spori *et al.* on titanium oxide.[31] We also observed that the functionalized substrates exhibit low hysteresis of the contact angle, from 27° for C12P to 21° for of C18P, which reflects the good quality of the formed SAMs. We attribute this behavior to the fact that, according to XPS, H_2 plasma promotes the formation of metal hydroxides that probably favors the formation of surface bound phosphoric esters during the grafting process.[32,33]

Therefore, H_2 plasma treated samples will be used through the rest of the chapter.

Kinetics studies. We studied the kinetics of the self-assembly process at room temperature for the C12P and C18P SAMs, and modeled the evolution of the $w\theta_{CA}$ as function of time. We prepared a set of samples treated with H_2 plasma and immersed them in an APA solution for reaction times ranging from 1 second up to 16 hours.

Cassie's Law[34] states that the θ_{CA} of a liquid on a composite surface can be obtained from the area fraction and the contact angles of each component,

$$\cos\theta_{CA} = f_1 \cos w\theta_1 + f_2 \cos w\theta_2 \qquad \text{[Eq.1]}$$

where $w\theta_1$ is the contact angle and f_1 is the area fraction for component 1 and $w\theta_2$ is the contact angle and f_2 is the area fraction for component 2. Accepting that the Py-APA system follows Cassie's law, we can consider that Py is component one and APA SAM is component 2.[34] Taking into account that $w\theta_{Py}$ = 30° and cos $w\theta_{Py} \approx 1$, the surface coverage, Γ - defined as the number of adsorbed molecules on a surface divided by the number of molecules in a filled monolayer on that surface - can be estimated at a given functionalization time as:

$$\Gamma = \frac{1 - \cos w\theta_t}{1 - \cos w\theta_\infty} \qquad \text{[Eq.2]}$$

where $w\theta_t$ is the measured contact angle at time t and $w\theta_\infty$ is the measured contact angle for a fully functionalized surface. The measured coverage values as function of time are represented in Figure 6.

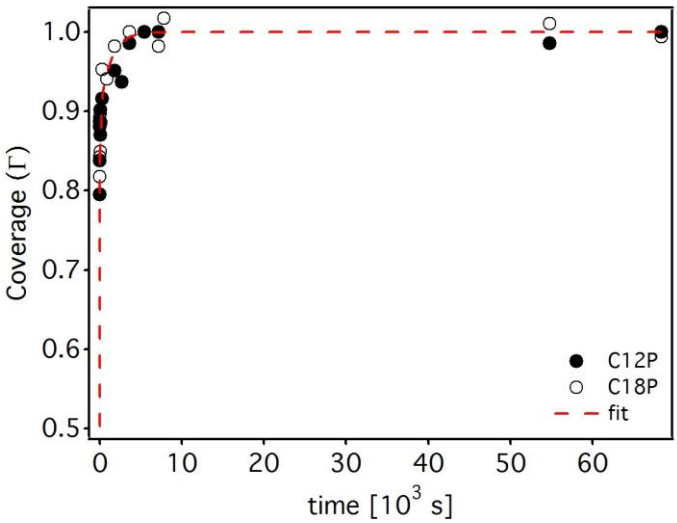

Figure 6 - Coverage as a function of time for a Py substrate functionalized with 2 mM C12P (solid circle) and C18P (hollow circle) 2-propanol solutions. Data have been fitted to a biexponential Langmuir isotherm (dashed red line).

As can be seen, no significant differences in coverage as a function of time are detected between C12P and C18P. First, we tried to model the data using a Langmuir isotherm with a single rate constant:

$$\Gamma = 1 - e^{-kCt} \qquad \text{[Eq.3]}$$

In this equation, again Γ is the surface coverage, *k* is the kinetic absorption constant, *C* is the concentration of the APA and *t* is the dipping time. However,

we were unable to describe our data with Eq.3. This simple model considers irreversible binding to the surface, only takes into account the number of the available sites on the surface and that the molecules adsorb into an immobile state without interactions with adjacent sites. As a result, it has shown to be insufficient to described the behavior observed in Figure 6.[35] To be able to build an effective adsorption model for our system, we were forced to consider a biexponential function (Eq. 4 and dashed line in Figure 6), that describes the formation of the monolayer as two cooperative processes:[36,37]

$$\Gamma = 1 - ae^{-k_1 Ct} - (1-a)e^{-k_2 Ct} \qquad \text{[Eq.4]}$$

The difference of several orders of magnitude in the two k values obtained after the fitting (k_1 = 1400 $M^{-1}s^{-1}$ and k_2 = 0.4 $M^{-1}s^{-1}$) can be rationalized as follows: Initial growth (k_1) is fast due to high availability of reaction sites. However, as time goes by, further growth is quenched. The slowing of the process may be caused by several factors, for example the hindering of reaction sites by the molecules that are already grafted, or the presence of physisorbed solvent molecules. The diffusion of the incoming molecules involves a rearrangement of the molecules, and the approaching of the entering surfactant molecules requires higher activation energy; all this is reflected in the smaller value of the second-rate constant.

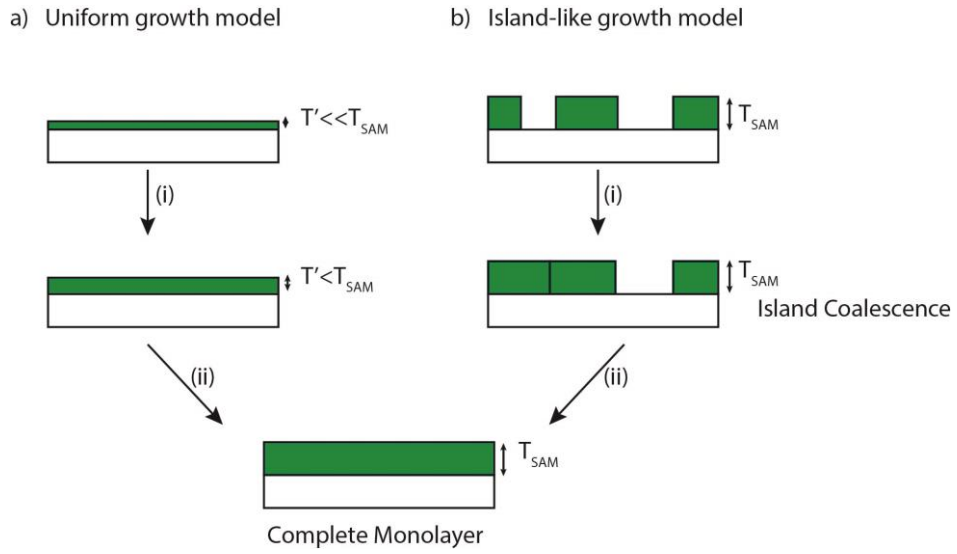

Figure 7 - SAM growth models: a) Uniform growth model: a complete monolayer is formed and the thickness increases synchronously as a function of time (i-ii). b) Island-like growth model: the molecules arrange themselves into discrete domains: (i) when two domains come in contact, coalescence takes place forming a bigger domain, which continues to grow until a complete monolayer is formed (ii). The thickness is maintained through the self-assembly.

Growth mechanism. Two main growth models have been reported for SAMs, as represented in Figure 7, namely the uniform growth (Figure 7a) and the island-like growth (Figure 7b). In the first one, a liquid-like, disordered film with molecules lying flat to the surface is formed all over the surface (SAM thickness at a given time is lower than the final thickness T'<<T, figure 7a,i); as the grafting process goes on and the coverage increases, more molecules are incorporated to the assembly, which is eventually converted into the final, highly ordered film structure, with the expected final SAM thickness (T, Figure 7a,ii). In contrast, for the second model, islands of densely packed molecules with a local structure similar to the complete monolayers are formed from the beginning of the assembly process (Figure 7b,i). When coverage increases,

these islands grow laterally and when they enter in contact with another one, they join to form larger aggregates (coalescence process), (Figure 7b,ii). This process continues until a complete monolayer is formed. For example, Woodward *et al.* performed AFM measurements on quenched mica substrates functionalized with APAs during the SAM growth, and demonstrated that the formation proceeded by nucleation, growth and coalescence of submonolayer islands.[38] A similar behavior was observed by Gawalt *et al.* while functionalizing titanium oxide.[15] On the other hand, Helmy et al.[36] studied the functionalization of titanium oxide with APA by means of IRRAS, monitoring the position of the methylene stretching and observed that in the early stage of the reaction, molecules were randomly distributed on the surface, while as the coverage increased, the order in the monolayer gradually increased until reaching the final highly ordered state.

In order to investigate if the growing mechanism of APAs on Py fits into one of the above cases, we imaged samples treated with 2 mM C18P 2-propanol solutions for short periods of time (less than 1 minute, or 85% coverage according to Figure 6) using AFM. This is represented in Figure 8.

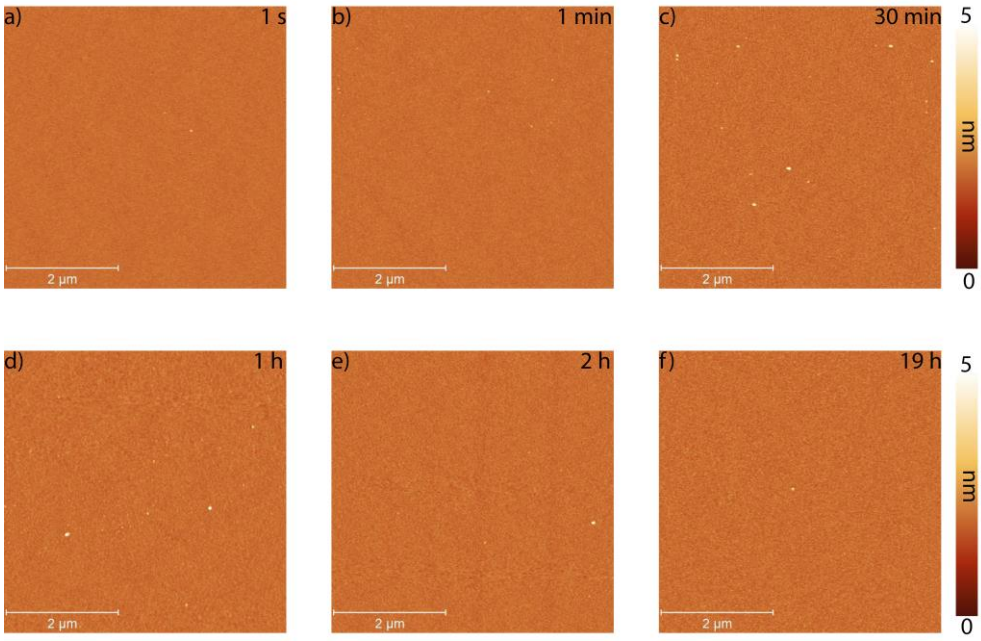

Figure 8 – (a-f) AFM images of a functionalized Py substrate with C18P took at different times.

Samples did not show evidence of island-like features. Instead, homogenous surfaces were imaged suggesting the presence of surfactant molecules randomly distributed on the surface according to a uniform growth mechanism.[39,40]

2.2.2 Structural Characterization

Once the optimum conditions for APA SAMs growth on Py were settled, and the mechanism and kinetics of the process clarified, we continued with their structural characterization. For that purpose, we used several surface based characterization techniques to shine light on their internal structure.

AFM imaging. Tapping mode AFM topography images of 15 nm H_2 plasma treated Py samples immersed for 16h in neat solvents or in solutions of APA with different chain lengths, were routinely performed and are shown in Figure 9. Noticeably, the growing process took part without a substantial increase in surface roughness. The RMS values measured using AFM for fully covered samples (approx. 0.28 nm) were slightly above to that of a Py substrate immersed in neat solvent during the same amount of time (RMS ≈ 0.18 nm).

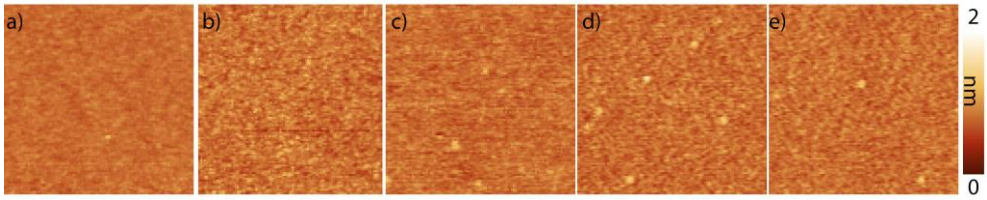

Figure 9 - AFM topographic images (1x1 μm²) of H_2 plasma treated Py substrates: a) neat solvent, b) C12P SAM, c) C14P SAM, d) C16P SAM, e) C18P SAM.

Mass spectrometry. CnP (n=12, 14, 16, 18) SAMs on 15 nm Py were analyzed by MALDI-TOF spectrometry (Figure 10) in order to prove the presence and integrity of the molecule on the Py substrate. Last developments in instrumentation have permitted to apply this technique to the detection of thin films and SAMs and even to differentiate between monolayer and multilayer formation on surfaces.[41] For n= 12-16, peaks corresponding to the $[CnPH]^+$ molecular ions were visible at the right mass-to-charge ratio. In the case of the C18P monolayer, this species cannot be clearly identified without ambiguity as a result of interfering peaks coming from the polymer matrix used during the experiments. Quiñones et *al.*, functionalized nickel oxide with APA, and characterized the resulting SAMs using MALDI-TOF.[20] They observed the

presence of signals arising from dimer plus one hydrogen (m/z=672, for C18P dimer) formed during the assembly process. They correlated this signal with the presence of multilayers in their films.[20,41] In our case, we did not observe peaks correlated to dimers, but exclusively peaks associated with the molecular ion. This suggests that single layer APA films are formed over Py, as will be later confirmed using XRR.

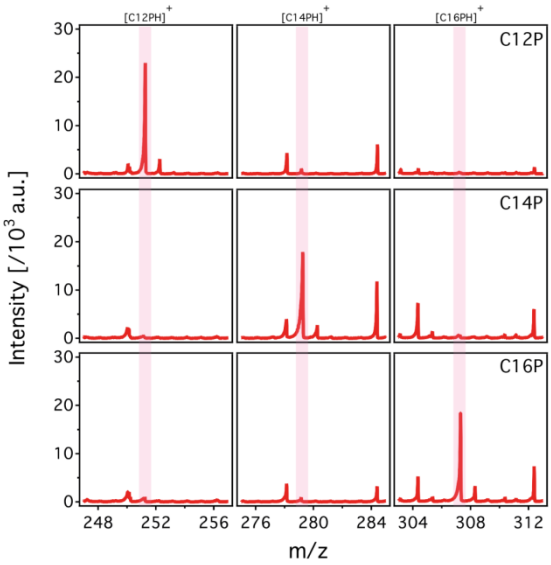

Figure 10 - MALDI-TOF spectra measured for C12P (Mw=250.31), C14P (Mw=278.37) and C16P (Mw=306.42) SAM-functionalized Py substrates.

Infrared spectroscopy. Next, we used IRRAS to further confirm the presence of the molecules on the surface and to estimate the degree of order and the tilt of the alkyl chains in the SAMs.

Figure 11 shows the C-H stretching region of the corresponding spectra for the two extremes of alkylphosphonate SAMs used in this work: C12P (red line) and

C18P (black line). Four peaks are identified in the spectra of APA SAMs on Py, which can be assigned from left to right to the CH_3as (~2965 cm^{-1}), CH_2as (~2924 cm^{-1}), CH_3sy (~2879 cm^{-1}) and CH_2sy (~2854 cm^{-1}) vibrations. Nevertheless, in some cases the CH_3sy peak was not observed due to its low intensity and intrinsic noise in the measurements. It is well known that the position of the methylene peaks gives information about the degree of order in the molecular layer: the higher the energy, the lower the order.[42] As shown in Figure 11, methylene asymmetric and symmetric peaks show a gradual red shift when going from C12P (2927 and 2856 cm^{-1}) to C18P SAM (2923 and 2852 cm^{-1}) with intermediate values for alkyl chains of intermediate length (Figure 12a).[30,43] These values indicate an evolution from a more liquid-like assembly in the shorter chains to a more crystalline structure in the longer chains, even though values are slightly above those reported for fully crystalline state (<2920 and 2850 cm^{-1}).

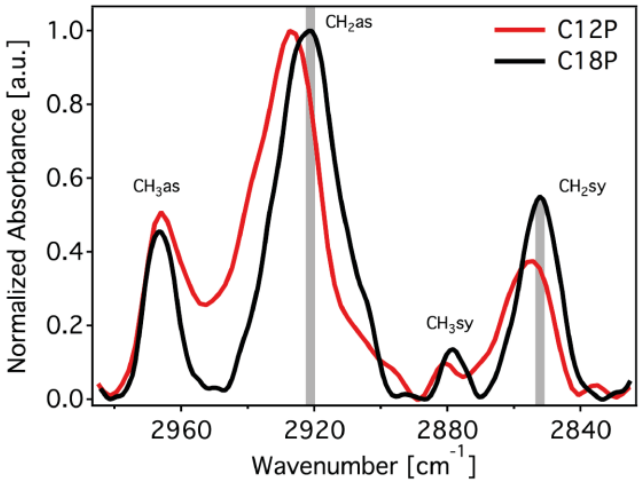

Figure 11 - IRRAS spectra of the region corresponding to the alkyl C-H stretching. C12P (red) and C18P (black) SAM-functionalized substrates. Vertical gray lines are a reference for the eye and mark the position of C18P methylene vibrations.

Additional information about the tilt angle (α) of the alkyl chain with respect to the surface normal was obtained from the peak intensity ratios of the methylene and methyl asymmetric stretches.[44] As described by Greenler in reference 44, the relation between α and the relative intensities of the CH_2as and CH_3as peaks is given by:[43,14]

$$I(CH_2)/I(CH_3) = (2/3)\cdot m\cdot[\cos^2(90-\alpha)/\cos^2(35-\alpha)] \qquad [Eq.5]$$

where *I* is the peak intensity, *m* is the number of methylene units in the chain and α is the tilt angle in degrees. The angles 90° and 35° are geometrical constants derived from the direction of the relevant stretches with respect to the long molecular axis.

Table 3 - Tilt angles [°] and thicknesses [Å] of different APA SAMs on Py estimated from the IRRAS spectra.

Number of C	Tilt angle [°]	IR Thickness [Å]
18	23	22
16	24	19
14	27	16
12	31	14

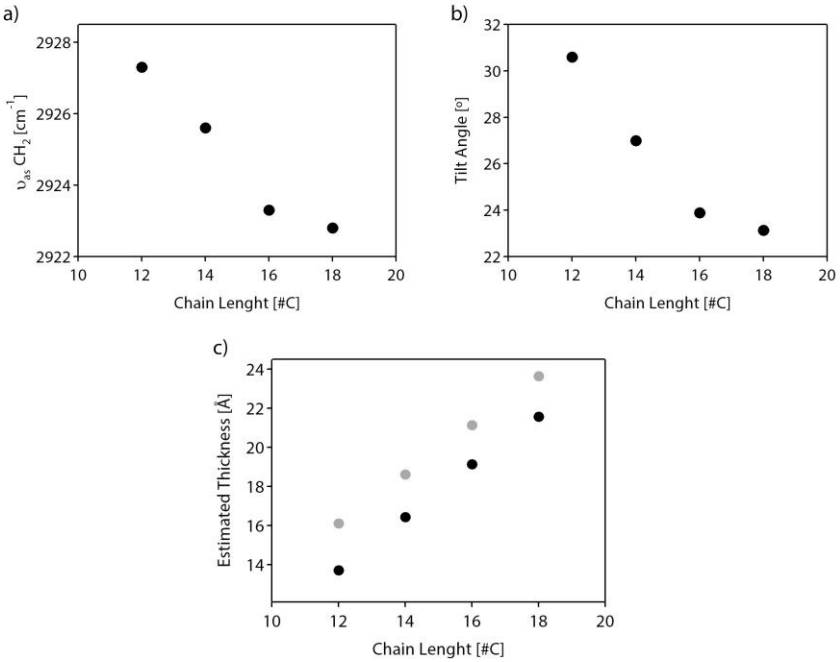

Figure 12 - Data analysis of the IRRAS measurements: (a) Position of the C-H bond antisymmetric strecth for alkylphosphonic acids of different chain length. (b) Estimated chain tilt angle (α) with respect to the surface normal of alkyl phosphonic acids of different chain length. (c) Estimated thicknesses from IRRAS spectra of monolayers with different chain length (black dots) and calculated thicknesses for vertical aligned all trans configuration (gray dots).

As summarized in table 3 and Figure 12b, the tilt angles progressively change from 31° (C12P) to 23° (C18P) when the chain length increases, in good agreement with previous observations. For example, Spori *et al.* reported a change in tilt angle of APA SAMs on titania from approximately 45° to 30 ° when increasing the phosphonic chain length from twelve to eighteen carbons[31] and Levine *et al.* on alumina from 33 ° to 26 ° when going from eight to sixteen carbons.[45]

The theoretical thickness of a perfectly stretched (all-trans) APA SAM as function of the tilt angle (assuming a tridentate binding to the surface), bond angles of 109.5° and bond-lengths of 1.78 Å C-P, 1.55 Å P-O, 1.54 Å C-C (Figure 13), can be described according to Eq. 6 :

$$T[Å] = 2.30 + ((n/2)-1)\cdot 2.51\cdot\cos(\alpha) + 1.54\cdot\cos(\alpha+35.25) \qquad [Eq.6]$$

being *n* the number of C atoms in the chain and α the tilt angle. From the tilt angles obtained from the IR analysis (Table 3 and eq. 6) we can estimate SAM thicknesses for different chain lengths (Table 3 and Figure 12c). One can see that the difference between the experimental and the theoretical thickness of the formed SAMs is roughly of 2 nm, which is in good agreement with the observed tilt angles.

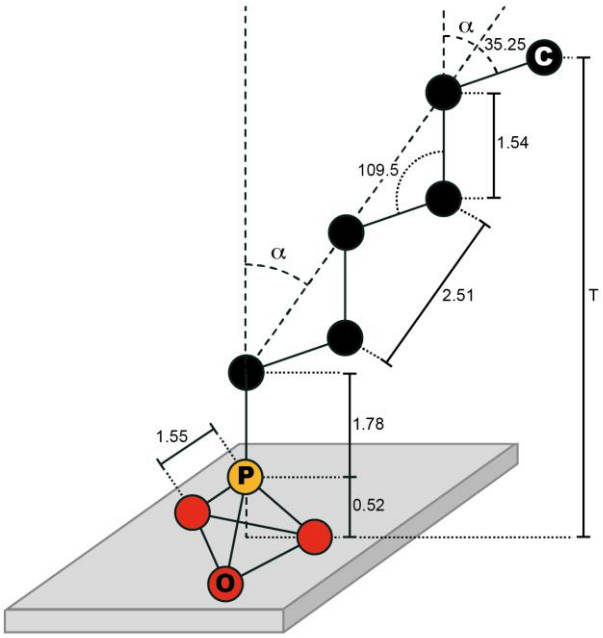

Figure 13 - Sketch of an alkylphosphonic acid anchored to the surface through a tridentate binding. Angles and bond distances used to estimate the theoretical thickness of a SAM are included.

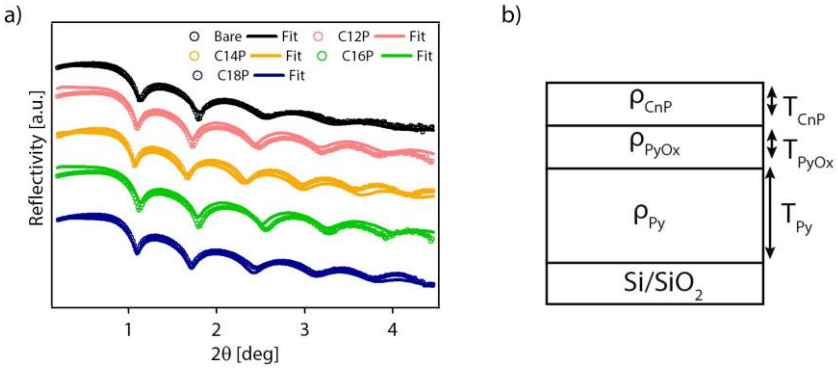

Figure 14 - a) XRR reflectograms of Py surface subjected to H_2 plasma (black dots) and then functionalized with CnP : C12P (pink dots), C14P (orange dots), C16P (green dots) and C18P (purple dots). b) Model used to fit the curves (solid lines in (a)).

X-Ray Reflectivity. XRR was used to confirm the calculated film thicknesses and estimate SAM densities (ρ). XRR spectra of the functionalized CnP Py samples, are showed in Figure 14a. The reflectograms have been modeled using a three-slab model (SAM/Oxide/Metal) displayed in Figure 14b, where the monolayers density (ρ) is kept constant throughout all the film.

As observed in figure 14, when going from shorter to longer chain lengths the film thickness increases (the thicker film, the shorter period of the oscillations) The measured average film density is $\rho_{av} \approx 0.78$ g/cm^3 and the thicknesses (T) are those reported in Table 4. For the calculation, we fixed the PyOx and Py densities to 8.6 g/cm^3, according to the values reported in Table 1.

Table 4 - Densities and thickness obtained from the fitting of data represented in Figure 13 to a the three slab model. * indicates which parameters were fixed during the fitting.

Sample	ρ_{CnP} [g/cm^3]	T_{CnP} [nm]	ρ_{PyOx} [g/cm^3]*	T_{PyOx} [nm]*	ρ_{Py} [g/cm^3]*	T_{Py} [nm]
Bare	-	-	6.74	1.7	8.6	13.3
C12P	0.78	1.5	6.74	1.7	8.6	11.8
C14P	0.78	1.7	6.74	1.7	8.6	11.6
C16P	0.78	2.0	6.74	1.7	8.6	11.3
C18P	0.78	2.5	6.74	1.7	8.6	10.8

Considering the films formed by a P atom and an alkyl chain, the area per molecule ($ApM = Mw/(\rho_{av} \cdot T \cdot N_A) \cdot 10^{24}$ can be estimated to be 24.5 Å^2 for a C18P

film (Mw = 284.46 and Z = 160) and 26.5 Å^2 (Mw = 230.30 and Z = 112) for a C12P film. These values are not very far from those reported for other model systems: alkylsiloxanes on silicon (21 Å^2),[39] thiols on gold (21.7 Å^2),[46] or alkylphosphonic acids on alumina (28-57 Å^2) this results further supports the good quality of the assembled films.[45]

XPS measurements. High resolution P2p XPS spectrum of a C18P functionalized Py sample, shows the presence of phosphorous (Figure 15), confirming the successful grafting of the molecules on the surface. Moreover, the adsorption of SAMs of increasing chain lengths resulted in a progressive attenuation of the different substrate core level signals.

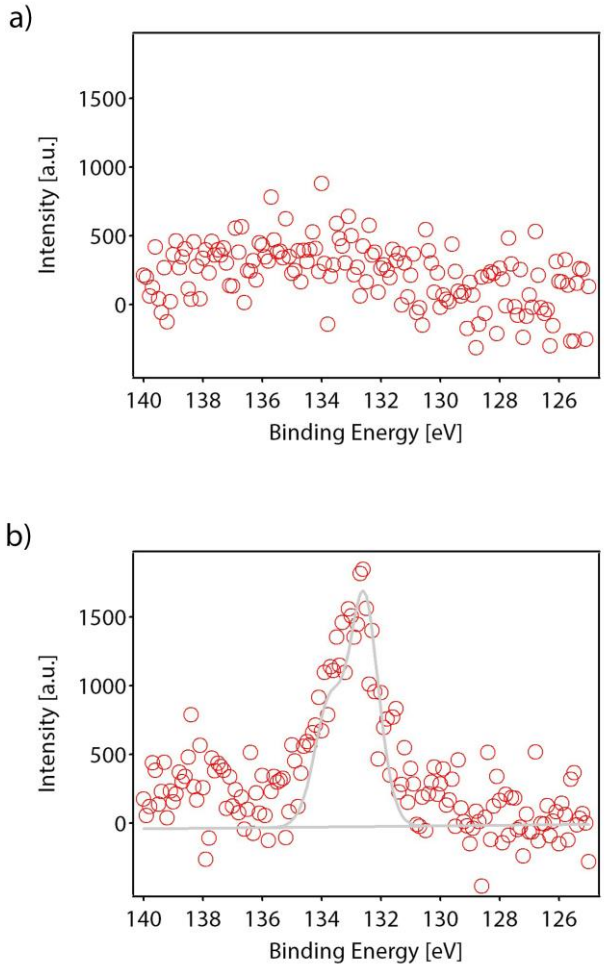

Figure 15 - P2p3/2 XPS spectra of: (a) bare Py substrate. (b) C18P SAM on Py.

The thickness increase with the respect of C12P ($T\text{-}T_{12}$), can be estimated using the following formula:[47]

$$(T\text{-}T_{12}) = \lambda \cos\theta \ln (I_n / I_{12}) \qquad [Eq.7]$$

where *I* is the intensity of the measured signal, *T* the thickness of the film, T_{12} the thickness of the C12P SAM, *n* refers to the number of carbon atoms in a

given measured alkyl chain, θ is the angle between the X-Ray source and the sample and λ the attenuation length of the photoelectrons through the hydrocarbon layer.

We used the intensity values of the Ni2p signal to obtain the thickness increase per methylene group (*d*) for each of the studied APA, Figure 16 a. The value of λ was set to 35.4 Å as estimated using the empirical equation reported by Bain and Whitesides.[48]

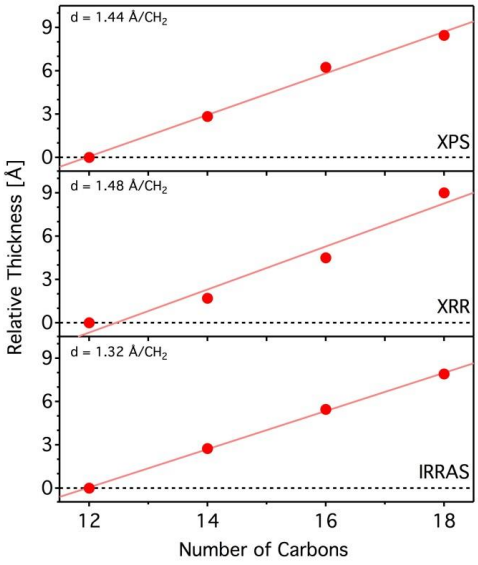

Figure 16 - Relative thickness of APA monolayers formed on Py as determined from XPS, XRR and IRRAS.

Figure 16 compares the thickness increase as function of the number of carbons estimated using XPS, XRR (Table 4) and IRRAS (Table 3) data. From this data, the d can be calculated from a linear fit of the measured relative thicknesses with respect to the number of carbons in the alkyl chain. The XPS

value 1.44 Å/CH_2, is in agreement with the d values reported in Table 3 and Table4 and calculated from XRR (1.48 Å/CH_2, Figure 16b) and IRRAS measurements (1.32 Å/CH_2, Figure 16c). All those values are higher than 1.26 Å/CH_2, the value expected for a perpendicular fully extended alkyl chain with C-C distances equal to 1.54 Å. This fact reflects the progressive reduction of the monolayer tilt angles when going towards longer chain lengths.

2.2.3 Magnetic characterization of modified substrates

One of the most valuable properties of Py is its FM behavior at room temperature. This is the reason why the study of its magnetism before and after the SAM formation is important. In order to characterize the magnetic properties of the Py films, we took advantage of magneto-optical Kerr effect (MOKE) spectroscopy.[49] This technique has a very high surface sensitivity and is able to register hysteresis loops of a magnetic sample by measuring the rotation in the polarization plane (Kerr rotation) of the light reflected on the surface.

The Py oxide behaves at room temperature as a paramagnet and it does not affect the magnetic behavior of the underlying Py film. Below 195 K, (Neel T) the Py oxide undergoes a long-range AF ordering. This results in an exchange bias interaction between the AF oxide and the FM Py layer, which induces an enhancement of coercive field in the magnetic hysteresis loop.[12,13,50]

We prepared a set of Py samples subjected to different treatments, as represented in Figure 17: an O_2 and H_2 plasma-treated samples (red and blue), a H_2 plasma-treated sample that was then functionalized with an APA SAM

(green), an air-oxidized sample without any further treatment (gray) and a gold-capped Py sample that was used as a reference (black).

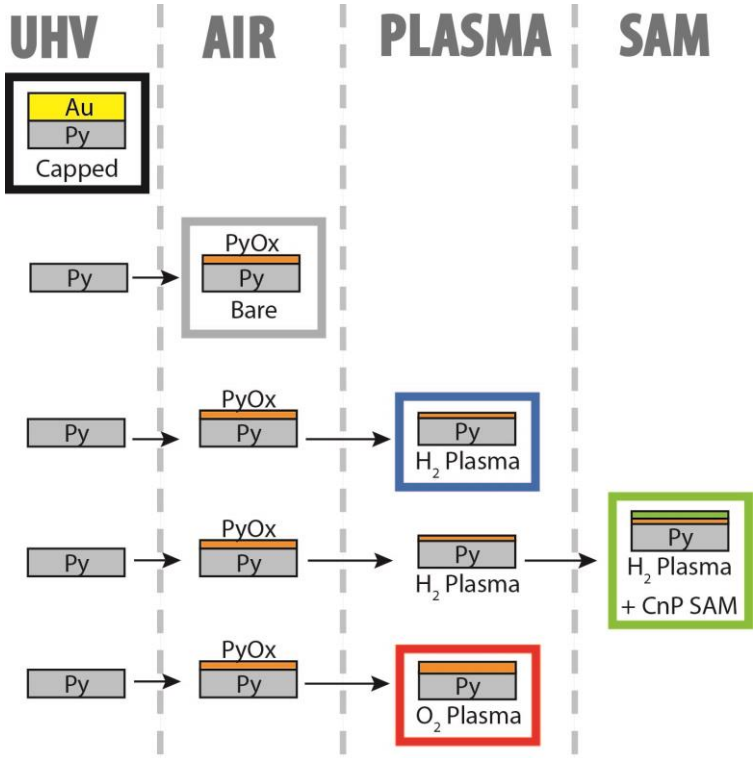

Figure 17 - Preparation of the different samples used for the MOKE measurements.

In Figure 18 the hysteresis curves recorded using MOKE at 22 K (top) after field cool at 325 mT and at room temperature (bottom) are shown.

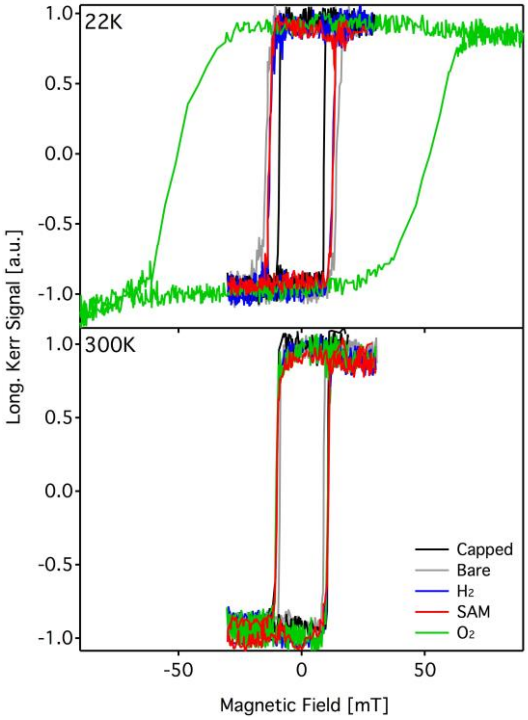

Figure 18 - Low temperature (top) *vs* room temperature (bottom) magnetization (measured using MOKE technique) recorded for a non-oxidized gold-capped Py sample (Capped) and air oxidized (Bare), pre-treated with hydrogen plasma (H_2), pre-treated with hydrogen plasma and APA functionalized (SAM) and pre-treated with oxygen plasma (O_2) samples.

All the samples show a similar coercive field of about 9 mT at room temperature (Figure 18). In contrast, well below the Neél temperature of the AF oxide, the samples show an increase in coercivity. The coercive field values are 50 mT for the oxygen treated sample, ca. 13 mT for the hydrogen treated samples and 14 mT for the air oxidized sample. No appreciable increase in coercivity has been observed for the gold protected sample (9 mT). The magnitude of the effect is larger for the oxygen, in accordance with the presence of a thicker oxide layer in this sample (Table 1). This result points out

that the SAM formation process preserves the integrity of the native oxide layer and that the magnetic properties of the Py film are unaltered after the grafting process.

2.2.4 APA SAMs Applications

As resist agents. The fabrication of microstructures using patterned SAMs as nanometric etch-resistant masks has been used successfully in nanoelectronics and nanofabrication. SAMs can be locally formed by means of microcontact printing lithography (μCP). This soft lithography uses the relief patterns on a master stamp to transcribe patterns of an ink (e.g. a SAM) through conformal contact on the surface of a substrate. As pointed out above, each kind of substrate needs a specific derivatized molecule. Thus, alkanethiols have been commonly used on metals, while acid-functionalized molecules as carboxylic or phosphonic acids have been chosen for metal oxides like aluminum and glass. However, patterned SAMs on Py have never been fabricated[51] despite the fact that, arrays and films of different shapes and structures of Py have been intensively studied during the last years, due to their interest in nanomagnetism[52] and in storage technologies.[53] In this scenario, we tested APA SAMs on Py as potential resists to fabricate nanostructured substrates.

In order to prepare the polymeric stamp, we used a compact disc (CD) as mold due to its periodic pattern of stripes. After removing the protective coating of the CD, a polydimethylsiloxane (PDMS) solution was spin-coated on it and annealed in air atmosphere. The PDMS stamp was then piled off, and after being soaked with a fresh APA solution, it was used to transfer SAMs patterns

onto hydrogen activated Py surfaces. Although, the APA isopropanolic solution, used for the preparation of SAMs by immersion method, gave rise to non-homogeneous SAM deposition, when we substituted isopropanol as ink media with diethylene glycol (a solvent of higher density and lower vapor pressure ending), well defined and compact SAM patterns were obtained. We used contact mode AFM to obtain the friction image (Figure 19a), because the nanometric thick features were not distinguishable from the non-patterned regions. After performing an etching of the Py with glycolic acid (GA), bare Py regions were attacked while the APA SAM protected regions remained intact. The high control of the spreading effect during SAM formation is highlighted by the sub-micrometric size of the developed structures (Figure 19b and 19c).

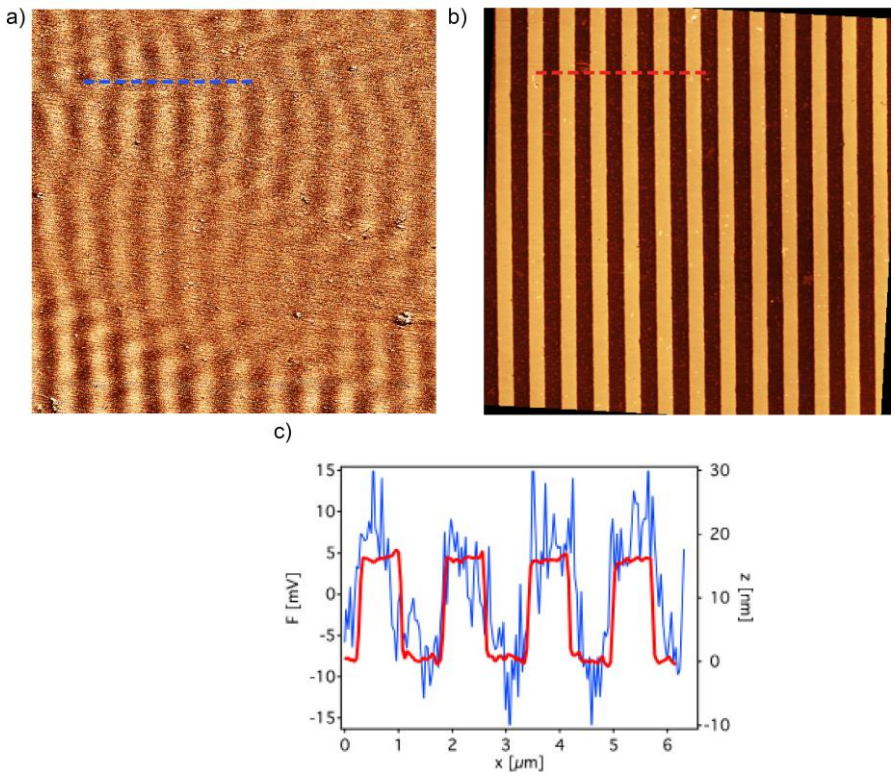

Figure 19 - a) Friction AFM image of 15 µm² of C18P SAM stripes patterned on a ~16 nm thick Py substrate, taken before etching. b) Topographic AFM image of sample showed in (a) after the etching treatment. c) Height profile corresponding from the blue line in (a) and the red line in (b).

As layer by layer templates. Later on, our group reported the use of the methodologies described in this chapter to template the layer-by-layer (LbL) growth of NASF-1 films, a surface metal organic framework (surMOF) on Py films.[54] By directing MOF transfer with APA SAMs, very smooth, homogeneous, highly oriented and ultrathin films across millimeter-scale areas were achieved that display moderate conductivity likely due to electron hopping. Here, the SAM was key for directing the transfer.

2.3 Conclusions

The successful and optimized formation of SAMs based on APAs has been accomplished on oxidized Py surfaces for the first time. It has been demonstrated that a crucial and critical point is the use of hydrogen plasma as pre-treatment. This plasma, instead of acting as a reducing agent for the oxide, promoted the formation of metal hydroxides, as analyzed by XPS, that assist the binding of the phosphonic acid groups during the grafting process and determines the successful formation of high quality SAMs.

Detailed structural characterization of the monolayers has been performed by means of different techniques. According to wCA, XPS, MALDI-TOF and XRR, the APA SAMs formed on Py are comparable to other well-studied systems in terms of quality. Additional magneto-optical measurements have been carried out to discard any possible modification of the magnetic behavior of the Py film during the SAM growth, which would rule out its later application.

The use of microcontact printing, a soft lithographic technique, has allowed the formation of well-defined SAM patterns on Py. The quality of this printed SAM guarantees its use as protecting layer when exposing Py to an etching agent, giving rise to a wet chemical approach for line-of-sight patterning of Py surfaces. This result is very relevant for the interest of these hybrid interfaces in nanomagnetism and their potential applications like circuitry or storage technologies.

This work extends the already large number of utilities of Py, with the controllable modification of its surface by well-organized, strongly attached molecular units. We have also demonstrated that by directing MOF transfer with APA SAMs, very smooth, homogeneous, highly oriented and ultrathin surMOF films on ferromagnetic surfaces can be obtained.

.

2.4. References

1. Nahrwold, G. *et al.* Structural, magnetic, and transport properties of Permalloy for spintronic experiments. *J. Appl. Phys.* **108,** 13907 (2010).

2. Davis, J. R. *Nickel, cobalt, and their alloys*. (ASM international, 2000).

3. Rao, S. S. *et al.* Positive exchange bias in epitaxial permalloy/MgO integrated with Si (100). *Curr. Opin. Solid State Mater. Sci.* **18,** 140–146 (2014).

4. Ishihara, Y., Itou, N., Kimijima, T. & Hirano, T. Clean aluminum oxide formation on surface of aluminum cylinder in an ultraclean gas-sampling system. *J. Vac. Sci. Technol. A Vacuum, Surfaces, Film.* **17,** 3139–3143 (1999).

5. Smardz, L., Köbler, U. & Zinn, W. Oxidation kinetics of thin and ultrathin cobalt films. *J. Appl. Phys.* **71,** 5199–5204 (1992).

6. Li, J., Mayer, J. W. & Colgan, E. G. Oxidation and protection in copper and copper alloy thin films. *J. Appl. Phys.* **70,** 2820–2827 (1991).

7. Lee, W.-Y. Oxidation Studies of Permalloy Films by Quartz Crystal Microbalance, AES, and XPS. *J. Electrochem. Soc.* **124,** 1747–1751 (1977).

8. Fitzsimmons, M. R., Silva, T. J. & Crawford, T. M. Surface oxidation of Permalloy thin films. *Phys. Rev. B* **73,** 14420 (2006).

9. Brückner, W. *et al.* Oxidation of NiFe(20 wt.%) thin films. *Mater. Sci. Eng. B* **86,** 272–275 (2001).

10. Dagan, G. Passivation of Permalloy Thin Films. *J. Electrochem. Soc.* **139,** 1855–1861 (1992).

11. Hsiao, R. & Mauri, D. Plasma-induced surface segregation and oxidation in nickel-iron thin films. *Appl. Surf. Sci.* **157,** 185–190 (2000).

12. Hagedorn, F. B. Exchange anisotropy in oxidized permalloy thin films at low temperatures. *J. Appl. Phys.* **38,** 3641–3645 (1967).

13. Hagedorn, F. B. Anomalous Hysteresis Loops in Permalloy Thin Films near 4.2°K. *J. Appl. Phys.* **38,** 1362–1363 (1967).

14. Thissen, P., Valtiner, M. & Grundmeier, G. Stability of Phosphonic Acid Self-Assembled Monolayers on Amorphous and Single-Crystalline Aluminum Oxide Surfaces in Aqueous Solution. *Langmuir* **26,** 156–164 (2010).

15. Gawalt, E. S., Avaltroni, M. J., Koch, N. & Schwartz, J. Self-Assembly and Bonding of Alkanephosphonic Acids on the Native Oxide Surface of Titanium. *Langmuir* **17,** 5736–5738 (2001).

16. Raman, A. *et al.* Understanding Organic Film Behavior on Alloy and Metal Oxides. *Langmuir* **26,** 1747–1754 (2010).

17. Gao, W., Dickinson, L., Grozinger, C., Morin, F. G. & Reven, L. Self-Assembled Monolayers of Alkylphosphonic Acids on Metal Oxides. *Langmuir* **12,** 6429–6435 (1996).

18. Badia, A., Lennox, R. B. & Reven, L. A Dynamic View of Self-Assembled

Monolayers. *Acc. Chem. Res.* **33,** 475–481 (2000).

19. Zschieschang, U., Halik, M. & Klauk, H. Microcontact-Printed Self-Assembled Monolayers as Ultrathin Gate Dielectrics in Organic Thin-Film Transistors and Complementary Circuits. *Langmuir* **24,** 1665–1669 (2008).

20. Quiñones, R., Raman, A. & Gawalt, E. S. Functionalization of nickel oxide using alkylphosphonic acid self-assembled monolayers. *Thin Solid Films* **516,** 8774–8781 (2008).

21. Grosvenor, A. P., Biesinger, M. C., Smart, R. S. C. & McIntyre, N. S. New interpretations of XPS spectra of nickel metal and oxides. *Surf. Sci.* **600,** 1771–1779 (2006).

22. Pollak, R. A. & Bajorek, C. H. Surface composition and chemistry of evaporated Permalloy films observed by x–ray photoemission spectroscopy and by Auger electron spectroscopy. *J. Appl. Phys.* **46,** 1382–1388 (1975).

23. McIntyre, N. S. & Zetaruk, D. G. X-ray photoelectron spectroscopic studies of iron oxides. *Anal Chem* **49,** 1521–1529 (1977).

24. Otto, C. *et al.* Physical Methods for Cleaning and Disinfection of Surfaces. *Food Eng. Rev.* **3,** 171–188 (2011).

25. Rajalingam, S., Devillers, S., Dehalle, J. & Mekhalif, Z. A two step process to form organothiol self-assembled monolayers on nickel surfaces. *Thin Solid Films* **522,** 247–253 (2012).

26. Lee, W. Effects of Oxidation on the Atmospheric Corrosion of Permalloy Films. *J. Electrochem. Soc.* **126,** 1533–1539 (1979).

27. Hannon, J. B., Afzali, A., Klinke, C. & Avouris, P. Selective placement of carbon nanotubes on metal-oxide surfaces. *Langmuir* **21,** 8569–8571 (2005).

28. Zschieschang, U. *et al.* Mixed Self-Assembled Monolayer Gate Dielectrics for Continuous Threshold Voltage Control in Organic Transistors and Circuits. *Adv. Mater.* **22,** 4489–4493 (2010).

29. Allara, D. L. & Nuzzo, R. G. Spontaneously organized molecular assemblies. 1. Formation, dynamics, and physical properties of n-alkanoic acids adsorbed from solution on an oxidized aluminum surface. *Langmuir* **1,** 45–52 (1985).

30. Pellerite, M. J., Dunbar, T. D., Boardman, L. D. & Wood, E. J. Effects of Fluorination on Self-Assembled Monolayer Formation from Alkanephosphonic Acids on Aluminum: Kinetics and Structure. *J. Phys. Chem. B* **107,** 11726–11736 (2003).

31. Spori, D. M. *et al.* Influence of Alkyl Chain Length on Phosphate Self-Assembled Monolayers. *Langmuir* **23,** 8053–8060 (2007).

32. Giza, M., Thissen, P. & Grundmeier, G. Adsorption Kinetics of Organophosphonic Acids on Plasma-Modified Oxide-Covered Aluminum Surfaces. *Langmuir* **24,** 8688–8694 (2008).

33. Chockalingam, M., Darwish, N., Le Saux, G. & Gooding, J. J. Importance

of the Indium Tin Oxide Substrate on the Quality of Self-Assembled Monolayers Formed from Organophosphonic Acids. *Langmuir* **27,** 2545–2552 (2011).

34. Cassie, A. B. D. & Baxter, S. Wettability of porous surfaces. *Trans. Faraday Soc.* **40,** 546 (1944).

35. Schreiber, F. Structure and growth of self-assembling monolayers. *Prog. Surf. Sci.* **65,** 151–256 (2000).

36. Helmy, R. & Fadeev, A. Y. Self-Assembled Monolayers Supported on TiO_2: Comparison of $C_{18}H_{37}SiX_3$ (X = H, Cl, OCH_3), $C_{18}H_{37}Si(CH_3)_2Cl$, and $C_{18}H_{37}PO(OH)_2$. *Langmuir* **18,** 8924–8928 (2002).

37. Major, R. C. & Zhu, X. Y. Two-Step Approach to the Formation of Organic Monolayers on the Silicon Oxide Surface. *Langmuir* **17,** 5576–5580 (2001).

38. Woodward, J. T. & Schwartz, D. K. In Situ Observation of Self-Assembled Monolayer Growth. *J. Am. Chem. Soc.* **118,** 7861–7862 (1996).

39. Wasserman, S. R. *et al.* The structure of self-assembled monolayers of alkylsiloxanes on silicon: a comparison of results from ellipsometry and low-angle x-ray reflectivity. *J. Am. Chem. Soc.* **111,** 5852–5861 (1989).

40. Carraro, C., Yauw, O. W., Sung, M. M. & Maboudian, R. Observation of Three Growth Mechanisms in Self-Assembled Monolayers. *J. Phys. Chem. B* **102,** 4441–4445 (1998).

41. Quiñones, R., Raman, A. & Gawalt, E. S. An approach to differentiating

between multi- and monolayers using MALDI-TOF MS. *Surf. Interface Anal.* **39,** 593–600 (2007).

42. Ulman, A. Formation and Structure of Self-Assembled Monolayers. *Chem. Rev.* **96,** 1533–1554 (1996).

43. Tillman, N., Ulman, A., Schildkraut, J. S. & Penner, T. L. Incorporation of phenoxy groups in self-assembled monolayers of trichlorosilane derivatives. Effects on film thickness, wettability, and molecular orientation. *J. Am. Chem. Soc.* **110,** 6136–6144 (1988).

44. Greenler, R. G. Infrared Study of Adsorbed Molecules on Metal Surfaces by Reflection Techniques. *J. Chem. Phys.* **44,** 310–315 (1966).

45. Levine, I. *et al.* Molecular Length, Monolayer Density, and Charge Transport: Lessons from Al–AlOx/Alkyl–Phosphonate/Hg Junctions. *Langmuir* **28,** 404–415 (2012).

46. Dubois, L. Synthesis, Structure, and Properties of Model Oraganic Surfaces. *Annu. Rev. Phys. Chem.* **43,** 437–463 (1992).

47. Folkers, J. P. *et al.* Self-Assembled Monolayers of Long-Chain Hydroxamic Acids on the Native Oxide of Metals. *Langmuir* **11,** 813–824 (1995).

48. Bain, C. D. & Whitesides, G. M. Attenuation lengths of photoelectrons in hydrocarbon films. *J. Phys. Chem.* **93,** 1670–1673 (1989).

49. Rao, S. G. MOKE study of hybrid magnetic thin films: Permalloy on

molecular self-assembled monolayer. *Appl. Surf. Sci.* **258,** 5195–5199 (2012).

50. Nogués, J. *et al.* Exchange bias in nanostructures. *Phys. Rep.* **422,** 65–117 (2005).

51. Burdinski, D., Saalmink, M., van den Berg, J. P. W. G. & van der Marel, C. Universal Ink for Microcontact Printing. *Angew. Chemie Int. Ed.* **45,** 4355–4358 (2006).

52. Kohno, H. & Tatara, G. in *Nanomagnetism and Spintronics* 189–229 (Elsevier, 2009). doi:10.1016/B978-0-444-53114-8.00005-4

53. Mao, S. Tunneling magnetoresistive heads for magnetic data storage. *J. Nanosci. Nanotechnol.* **7,** 1–12 (2007).

54. Rubio-Giménez, V. *et al.* High-Quality Metal–Organic Framework Ultrathin Films for Electronically Active Interfaces. *J. Am. Chem. Soc.* **138,** 2576–2584 (2016).

3 Functionalization of metallic ferromagnetic surfaces

3.1. Introduction

In the previous chapter, we have used SAMs to functionalize passivated FM surfaces. However, when a ferromagnet gets oxidized it can lose its surface spin polarization properties and becomes useless as spin injecting electrode in spintronic devices. Moreover, the oxide decouples the SAM and the FM metal and prevents the use of SAM to tailor surface spin properties,[1] and lowers the device performance.[2,3]

Focusing on spintronic applications as one of the main goals of this thesis, in this chapter we will go one step further and SAMs will be grafted directly on FM metallic surfaces. In the literature, alkanethiols have been extensively used to modify metallic surfaces like gold,[4] but due to the difficulty to avoid their air oxidation problems, the functionalization of metals like silver[5] or copper[6] is far less extensive and there are only few works that face the direct assembly of SAMs on FM metals like cobalt,[7] iron[8] or nickel[9] and their alloys.

Different strategies have been reported that describe the formation of SAMs directly on bare FM metals. These methods could be divided in two groups: (i) Strategies that avoid the formation of the oxide layer, and (ii) strategies that recover the bare metal after removing the oxide layer.

(i) Strategies that avoid the formation of the oxide layer:

One of them is the use of vapor phase techniques to prevent the air exposure of these materials. In this case, the FM material is prepared using ultra-high vacuum techniques (UHV) (Figure 1a,i), then the molecule deposition is done without exposing the sample to the air under reduced pressure (Figure 1a,ii) or via vapor phase deposition under inert conditions. This limits the choice of molecules to those having high vapor pressure. Notice that, if the UHV chamber is directly connected to a glove box (inert atmosphere, Figure 1b,ii), one can also form the SAM in solution. If the SAM does not protect the substrate from reoxidation, the rest of layers and the top electrode must also be deposited without breaking the inert atmosphere (Figure 1a-1b,iii) to form the spintronic device. This approach have been used to functionalize a fresh sputtered cobalt samples,[10] which were transferred from the sputtering system to a glove box, and then exposed to a dodecanethiol solution for 16 hours, after which SAM growth was observed.

A new approach recently reported to avoid the formation of native oxide is the so-called **template stripping (TS)** method. It involves the evaporation under UHV of a thin metal film on native silicon oxide surface or gold that is used as

template. In the next step a rigid support, for example a glass substrate, is glued against the metal so that a stack is formed by support/glue/metal. Next, the support is stripped from the template giving a clean and oxide free metal surface because up to this point, the bottom metal surface is in contact with the template and protected from the ambient environment. This approach was used by Kumar *et al.*[11] to form an alkanethiol SAM on a nickel surface. They evaporated a nickel film onto a perfluoroalkylsilane SAM modified silicon oxide surface. This SAM was used in order to minimize the interaction between the nickel and the bare silicon oxide surface, rendering easier the stripping process. In order to avoid the nickel oxidation, TS was performed inside a glove box. After this step, the TS nickel surface was exposed to a 3 mM ethanolic alkanethiol solution and after 16 h the functionalization was completed. S2p XPS analysis of the modified surface proved the presence of the metal-thiolate bonds, without detecting any oxygen. The monolayer thickness and tilt angle was also estimated, using angle resolved XPS, to be respectively 1.74 nm and 36°, which is in good agreement with previous reported results.[8,9]

(ii) Strategies that recover the bare metal after removing the oxide layer:

As an alternative strategy, the substrate once deposited is exposed to air and its surface oxidizes. In order to functionalize the metallic surface, it is mandatory to remove the oxide layer (Figure 1c,iiia), prior to the SAM formation (Figure 1,iiic). Oxide removal is usually carried out in inert atmosphere, using dry or wet etching methods.

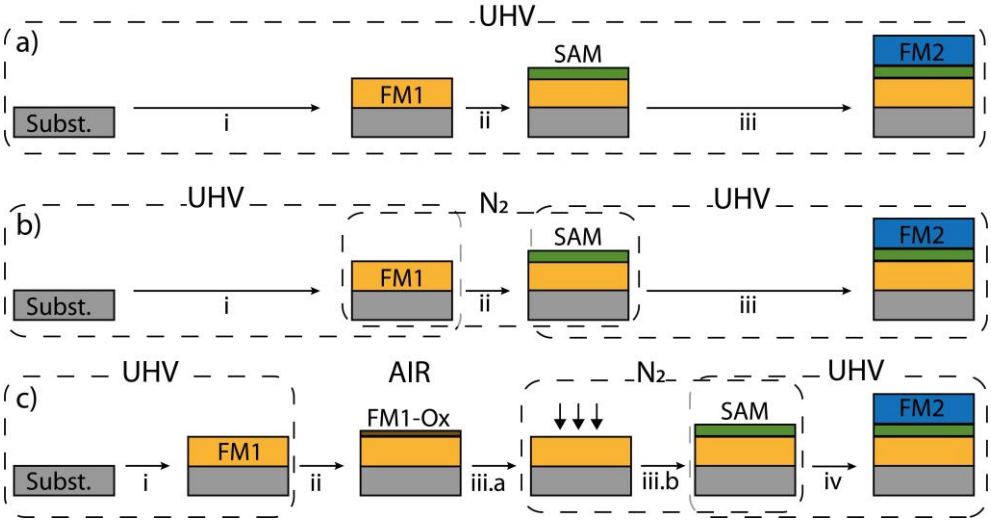

Figure 1 – Schematic representation of the fabrication of SAM-based spintronic devices. a) UHV route : i) bottom electrode deposition; ii) SAM formation; iii) top electrode deposition. b) UHV + GB route: i) bottom electrode deposition; ii) SAM formation in inert atmosphere; iii) top electrode deposition. c) Alternative route: i) bottom electrode deposition; ii) air exposure and oxide formation; iiia) oxide removal and SAM formation (iiib) in inert atmosphere; iv) top electrode deposition.

The first example found in literature that describes this strategy was presented by Vogt *et al.*[12] in 1997. This work reports the gas-phase adsorption of 11-mercaptoundecanoic acid on the surface of Ni crystal, which was cleaned using sputtering, to remove the oxide and the contaminants. The molecule, that has a residual vapor pressure lower than 10^{-3} Torr, was heated at 25° during 16 hours to perform the functionalization. The formed monolayer was attached by the sulfur atom to the surface, as confirmed by the S2p XPS spectrum, which presents the characteristic peak for metal-alkanethiolates at 161.8 eV. No oxygen was detected, suggesting an oxide-free nickel surface. Moreover, from the C1s spectrum no interaction between the carboxyl end of the SAM and the nickel surface was observed.

A different methodology is a wet approach, based on the **electrochemical reduction of the passivating oxide** and then the consecutive exposition of the metallic surface to the surfactant solution under inert atmosphere. In a pioneering work Mekhalif *et al.*[9] showed that it is possible to grow alkanethiol SAMs over nickel by performing an electrochemical reduction pretreatment in a perchlorate aqueous solution, prior to the exposition (in inert atmosphere) of the surface to the ethanolic dodecanethiol (C12S) solution. This fact was confirmed comparing the S2p XPS spectrum of electrochemical treated and polished nickel surfaces, both exposed to an ethanolic solution of dodecanethiol. Modified polished nickel showed complex S2p signals that were assigned to a mixture of sulfinates and sulfonates species. The electrochemical treated nickel sample only showed the characteristic doublet, assigned to the metal-thiolate bond. Hoertz *et al.*[8] used the same methodology to functionalize with hexadecanethiol the electroreduced surface of cobalt, iron and nickel. The formation of high quality alkanethiolate SAMs and their stability were confirmed by XPS. The S2p XPS spectrum, recorded after 9 days of air exposure, showed that the quality of the monolayers decreased. Thus a complex signal at 167 eV was observed, pointing out that new oxidized sulfur species were generated on the surface, which were absent in the spectrum collected just after the functionalization.

Electrochemical methods are mostly carried out in aqueous media, and this makes their implementation into inert glove-box atmosphere difficult. To avoid the use of aqueous based electrochemical etching, such as the ones described above, organic solvent-based **wet chemical etching** methods have also been developed.

Rajalingam *et al.*, [13] reported the use of hydrazine as etching agent. In their work, they exposed an oxidized nickel substrate to an alkaline hydrazine solution heated at 80 °C for five minutes. After this time the substrate was transferred to a dodecanethiol ethanolic solution and kept under argon atmosphere for 6 hours. The formation of alkanethiol SAM was monitored by means of XPS using the characteristic metal-thiolate peak at S2p spectrum. AFM measurements showed that the surface roughness decreases from 15 nm (in the bare substrate) to 11 nanometers. However, there is not any reference in the text about the selectivity of the etching methods towards nickel oxide or metallic nickel.

Similar wet chemical etching approaches have been used also to recover easily oxidizable metals different from FM ones. Caipa Campos *et al.*,[14] reported the use of glycolic acid to pre-treat a copper surface. In their report, they used a 10% ethanolic solution of EKC 570, a commercial post etch residue remover of DuPont that consists of a 70% w/v mixture of glycolic acid and ethanol. The copper surface was exposed to this solution for five minutes and then transferred to a decanethiol ethanolic solution under argon atmosphere. Hydrophobic $w\theta_{CA}$ were observed after the functionalization and XPS confirmed the presence of the metal-thiolate species in the S2p spectrum.

To sum up, dry methods, electrochemical reduction,[8,9] and wet chemical etching[13,14] have proved to be effective approaches to get rid of native oxide layers prior to the SAM formation. However, the first method requires of expensive equipment that is not always available, and the last methods share some inconveniences because, etching rate depends on the conditions used,

and more important, they do not present selectivity. Moreover, electrochemical etching tends to increase the surface roughness, which is an inconvenient because defects in molecular tunneling junctions, such as pinholes, need to be minimized to ensure good quality tunneling. Besides, most of the above methods are not compatible with the lithography techniques required to form reduced area contacts suitable to integrate SAMs into spintronic devices.

In this scenario, and taking into account the scope of this thesis (integration of a SAM as FM interface modifier and spacer in working spintronic devices), the chosen SAM growth approach has to permit the formation of oxide free and low roughness FM films down to nanometric thicknesses, while being compatible with lithography methods to build nanocontacts. Therefore, the performance of an optimized wet chemical etching under inert atmosphere seemed to be the best option, in this thesis we will use this approach to study SAM functionalization of cobalt (Co) and Permalloy (Py).

3.2. Results and discussion

3.2.1. Wet chemical etching studies

As highlighted above, we wanted to develop a novel method to etch selectively the oxide of FM surfaces without affecting the metallic bulk. Based on the reported wet chemical etching studies on nickel[13] and copper,[14] we identified hydrazine and glycolic acid as the most promising candidates for this purpose.

Inspired by Rajalingam's study on nickel hydrazine etching,[13] we decided to test if it was possible to extend this methodology to Co substrates. We first recorded the XRR reflectogram of a 12 nm Co film deposited on a silicon substrate, then the sample was exposed to a 10 % w/v hydrazine ethanolic solution under ambient conditions for 20 minutes and washed with fresh ethanol. Finally, the XRR reflectogram was recorded again (Figure 2a). Spectra were fitted using the two-slab model displayed in Figure 2c and the fitting results are reported in Table 1. As can be seen, after 20 min, hydrazine had only etched 1 nm of the film, when originally 2 nm was the estimated thickness of the Co oxide.

In the Rajalingam's paper authors describe the heating of the oxidized nickel sample at 80ºC in a basic hydrazine solution for 5 minutes, giving rise to a surface roughness decrease from 15 nm to 11 nm, but no AFM images are shown. Under the conditions described above, we observed through AFM (Figure 2b) that even at room temperature, the Co surface resulted heavily damaged with cracks going 5 nm into the Co surface. We attribute this to the

poor Co/Co oxide etching selectivity. Therefore, we discarded the potential use of hydrazine as suitable Co etching agent.

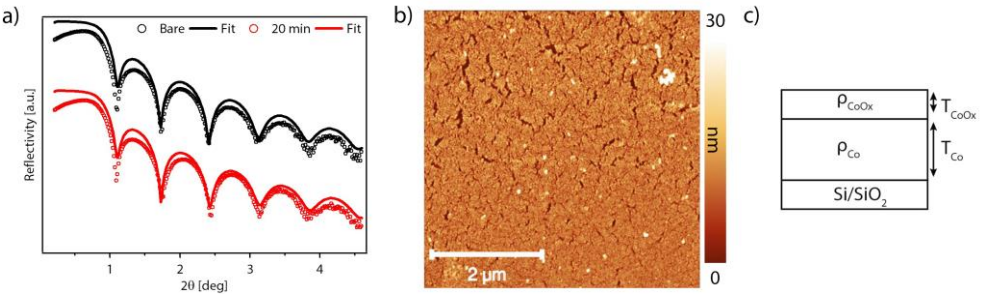

Figure 2 – Co sample treated with hydrazine: a) XRR reflectograms before and after the treatment. b) Topographic AFM image of the surface taken after the treatment. c) Model used to fit the reflectograms in a.

Table 1 - Fittings from XRR measurements according to the model shown in Figure 2c.

Sample	ρ_{CoOx} [g/cm^3]	T_{CoOx} [nm]	ρ_{Co} [g/cm^3]	T_{Co} [nm]
Before	6.11	2	8.6	10
After Hydrazine	6.10	1	7.9	10

Next, following Campos' work, we decided to test the effect of the glycolic acid (GA).[14] We exposed a 14 nm Co film to a 10 % w/v ethanolic solution of GA for 26 minutes under ambient conditions. We recorded XRR of the film, before and after the treatment (Figure 3a). Reflectograms showed that after 26 minutes of exposure to GA no trace of Co was left.

In order to understand how the GA was affecting the Co surface, we exposed a set of 3 Co surfaces to the same etching treatment following three different

approaches: Approach A: The etching was carried out in air atmosphere (Co-Ox). Approach B: The etching was performed in a glove box atmosphere (Co-GB) and approach C: Several etching air exposure cycles were repeated (Co-GB-stepped). The results of these experiments are represented in Figure 3.

Approach A (Co-Ox): We exposed five air oxidized Co samples to GA under ambient conditions from 0 to 26 minutes and measured the correspondent XRR reflectograms. Results are represented in Figure 3a. At a glance, it is possible to observe that fringe spacing, which depends on the thickness, decreases with time. The thicknesses after the GA treatment were calculated from the fitting of the refractograms, and are presented in Figure 3b. As can be seen, thickness linearly decreases with time. Fitting of the data to a line gives an etching speed of approximately 0.6 nm/min.

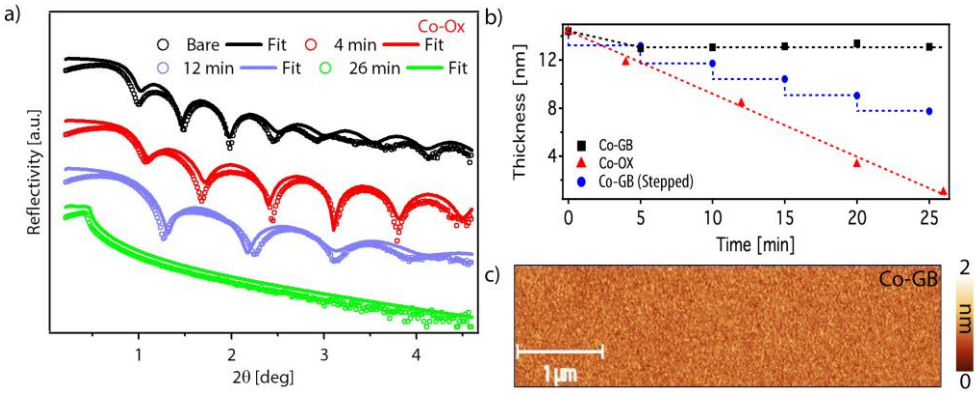

Figure 3 - Etching studies on Co samples: a) Reflectograms of Co-Ox samples exposed to GA for different times under ambient conditions (approach A). b) Co thickness measured in Co samples exposed to GA etching following different approaches: etching performed inside a glove box (Co-GB, approach B, black), and (Co-GB stepped, approach C, blue). c) Topographic AFM image under ambient conditions of a Co sample after 26 minutes of etching inside the glove box (Co-GB).

*Approach B (*Co-GB*):* We performed etching studies inside a glove box. We exposed a set of 5 samples to an anhydrous ethanolic GA solution from 0 to 25 min. We took out the samples at different times and measured the corresponding XRR reflectograms ex-situ under ambient conditions (Figure 3b, Co-GB, black line). We observed that, in this case, the thickness decreases, reaching a stable value after 5 min. The measured thickness reduction of 2 nm, is comparable with the native Co oxide thickness reported in the literature.[15] Moreover, we examined the topography of the sample by AFM, (figure 3c). The surface of a sample exposed to GA for 25 min shows a smooth and clean surface, without any signal of surface damage. This points out that under inert atmosphere the etching is performed selectively on the oxide and does not affect the bulk of the material.

Approach C: An air oxidized Co surface was exposed to GA for five minutes inside a glove box; then, the sample was took off from the glove box for at least 30 min, the XRR data collected, and was put back into the glove box for the next 5 minutes of GA exposition. As can be seen in Figure 3b, we observe that after each GA-air cycle, thickness decreases in 2nm steps. These results can be rationalized as follows: GA etched exclusively the oxide; once the etched sample is exposed to the air, a new oxide layer grows again. When the GA treatment is repeated, the fresh oxide is again etched away. This result is useful to explain what happens in the approach A: The GA selectively etched the oxide but, because oxygen is present in the solution, new oxide spontaneously grows on the surface and is etched away by GA. Because this continuous re-oxidation of the Co present on the surface, after 26 minutes there is no Co left on the surface.

We also studied the effect of the glycolic acid concentration towards the etching, using a range of concentration between 10% down to 0.5% w/v. We exposed a set of 4 samples to GA solutions for 1 hour inside the glove box and we recorded the correspondent reflectograms showed in Figure 4. The original thickness of the sample was 12 nm.

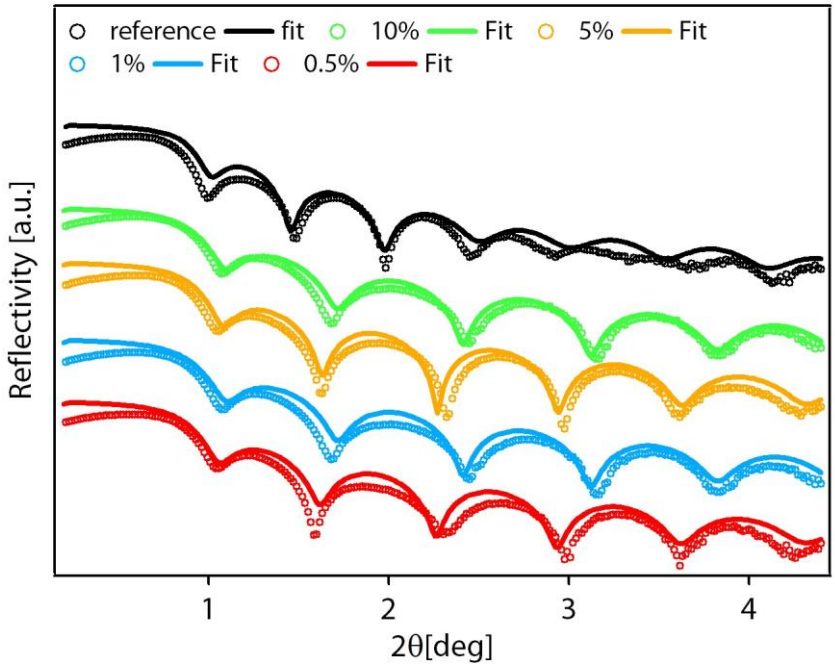

Figure 4 - Reflectograms of Co-Ox samples exposed to GA with different concentrations: reference (black), 10% (light green), 5% (orange), 1% (blue) and 0.5% (red).

From the fitting of the model, reported in Table 2, we calculated that 2 nm of oxide are etched, regardless of the concentration used. We decided to use as standard in all the tests performed in this thesis a 10% concentration.

Table 2 - Fitting parameters obtained from reflectograms in Figure 4

Concentration [w/v]	ρ_{CoOx} [g/cm^3]	T_{CoOx} [nm]	ρ_{Co} [g/cm^3]	T_{Co} [nm]
reference	6.11	2	8.6	10
10%	6.11	2	8.6	8
5%	6.11	2	8.6	8
1%	6.11	2	8.6	8
0.1%	6.11	2	8.6	8

Using AFM we also monitored how the surface roughness of Co samples etched under inert atmosphere change during the etching process. This aspect is very important for the incorporation of this methodology in the fabrication of spintronic devices. Topographic ex-situ AFM analysis of samples exposed to GA under inert atmosphere for 0 to 15 minutes are displayed in Figure 5a. As can be seen, the roughness increases after few minutes of exposition to GA, but a roughness comparable to that of the original untreated samples is recovered after 15 min, as is schematised in the pictorial representation in Figure 5b. We believe that in the initial steps of the process, Co oxide is partially and selectively dissolved and roughness increases; once all the oxide has been etched away, an oxide free metallic surface is recovered.

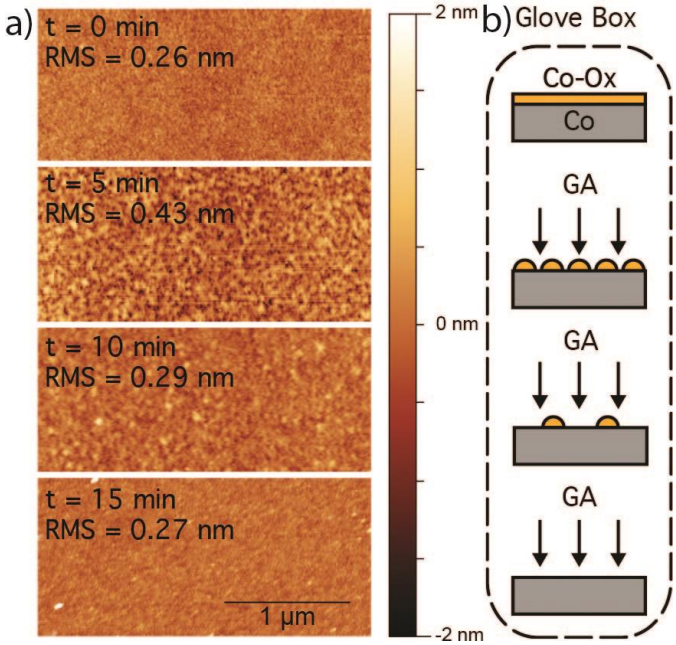

Figure 5 – a) Topographic AFM images measured under ambient conditions of air oxidized Co surfaces exposed to GA etching solutions in GB for different amounts of time. b) Pictorial representation of the Co oxide etching process, as a function of time.

To further support the selective etching of GA to the Co oxide, we used a patterned silicon substrate with Co stripes, that permitted us to measure the height of these stripes with AFM, before and after the GA etching. The sample was exposed to air for 16 hours and the height of the lines was determined by AFM. Next, we performed the etching in glove box, exposing the sample to GA for 15 minutes, and we measured the height one more time. The results are represented in Figure 6.

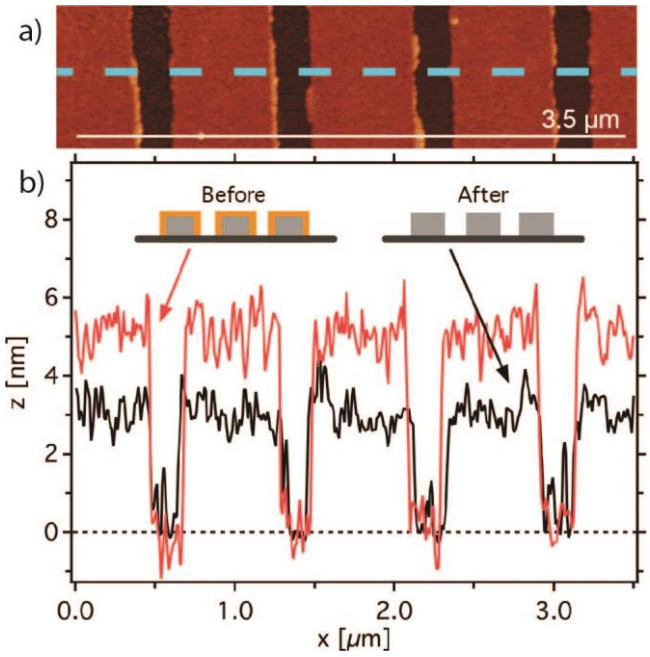

Figure 6 - a) Topographic AFM image of the patterned Co stripes on silicon surface. b) Topographic profile of two zones of the patterned stripes, before and after the GA etching. The difference between the two profiles is of 2 nm.

The high selectivity of the etching can be observed in Figure 6b. The difference in height of the patterned Co stripes, before and after the etching, is of 2 nm (red and black lines respectively) in accordance with XRR measurements. This confirms that the GA selectively etches Co oxide, leaving the metallic bulk unaffected.

Additionally, we performed further characterizations by means of *ex-situ* XPS measurements to confirm that etching completely removes metallic oxide. We prepared a set of three 10 nm thick Co samples, as represented in Figure 7. The first one, dubbed as Co-UHV, was prepared under UHV and capped with 25 nm of gold (red, Figure 7). The second sample, dubbed as Co-Ox, was exposed to

air and capped with the same amount of gold, (blue, Figure 7). The third one was exposed to air, etched and without breaking the inert atmosphere was capped with gold to avoid the re-oxidation, this is dubbed as Co-GA (black, figure 7).

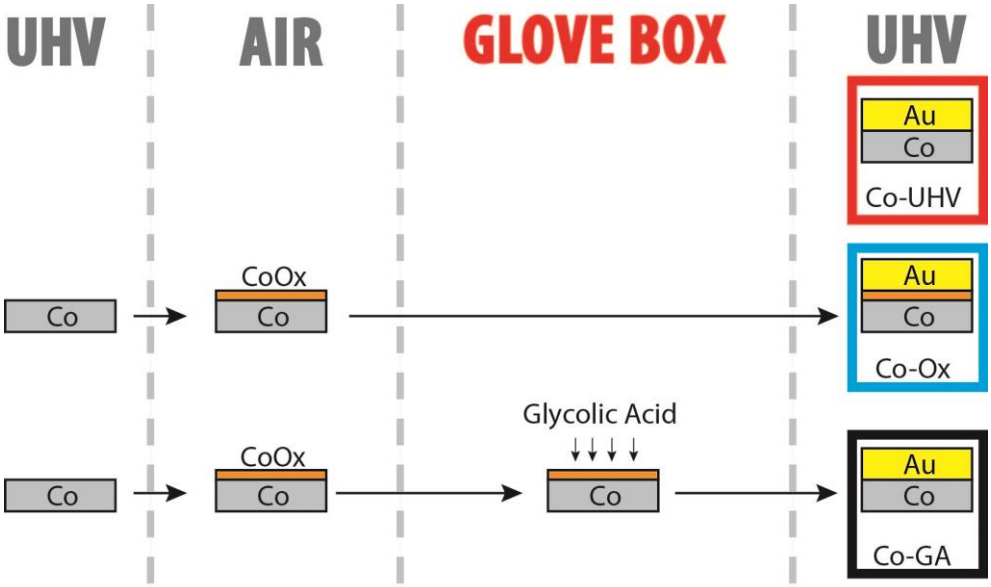

Figure 7 - Set of samples used for XPS and SQUID characterization: Co-UHV (red) was completely produced under UHV atmosphere. Co-Ox (blue) was exposed to air and then capped with gold. Co-GA (black) was exposed to air, treated with GA inside the glove box and then capped with gold without breaking the inert atmosphere.

In order to study the underlying Co surface, the protecting gold layer was first partially Ar^+ ion milled under UHV and then high resolution O1s and Co2p XPS spectra were directly recorded (Figure 8). In the air exposed sample, there is a peak with a pronounced shoulder, at 786.8 eV, which suggests the presence of Co(II) and Co(III) species. Moreover, the O1s spectrum shows the presence of two main contributions to the oxygen signal, coming probably from Co(II)

oxides (530.5 eV) and hydroxides (532.3 eV).[7] Meanwhile the results of the Co-GA totally match with the one of the reference sample (Co-UHV); no trace of oxygen was detected and the Co2p spectrum was compatible with a fully metallic surface. These data confirm that GA treatment is able to fully remove the Co oxide from the surface of oxidized samples.

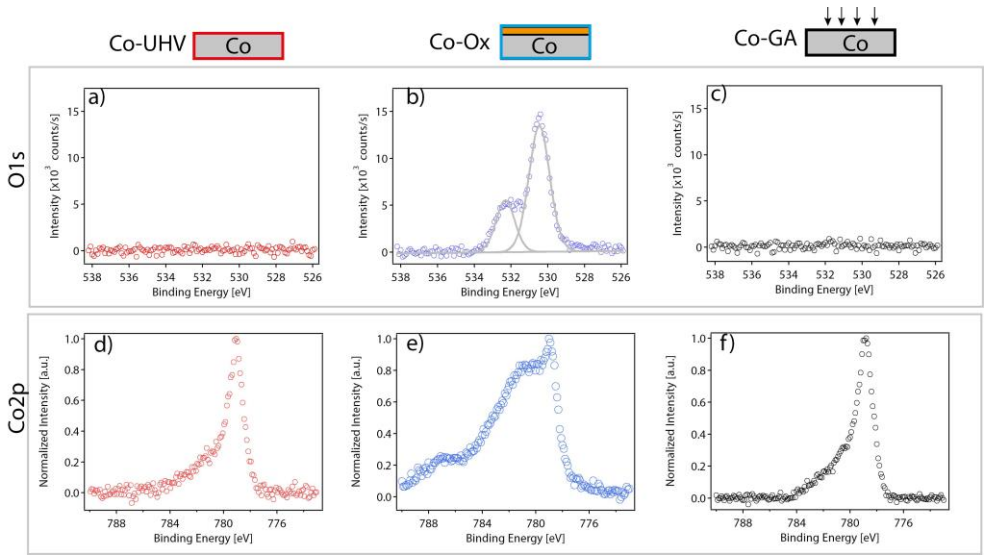

Figure 8 - XPS spectra of O1s (a-c) and Co2p (d-f) of Co samples subjected to different treatments: Co-UHV (red) was completely produced under UHV atmosphere. Co-Ox (blue) was exposed to air and then capped with gold. Co-GA (black) was exposed to air, treated with GA inside the glove box and then capped with gold without breaking the inert atmosphere.

We also performed the magnetic characterization of a set of analogue samples to the ones showed in figure 7 using a SQUID magnetometer. We measured the magnetization hysteresis loop at 30 K, after doing a field cool with 1 T, as represented in figure 9. The etched (Co-GA) and the in situ (Co-UHV) samples, show the same coercive field of about 4 mT, while the air exposed sample has a coercive field of 60 mT, caused by the exchange bias interaction between the

coupling of the ferromagnetic bulk and the antiferromagnetic oxide layer.[16] When the temperature is decreased, in the presence of a magnetic field, the FM Co and AF Co oxide layers are pinned and larger coercive fields are measured.

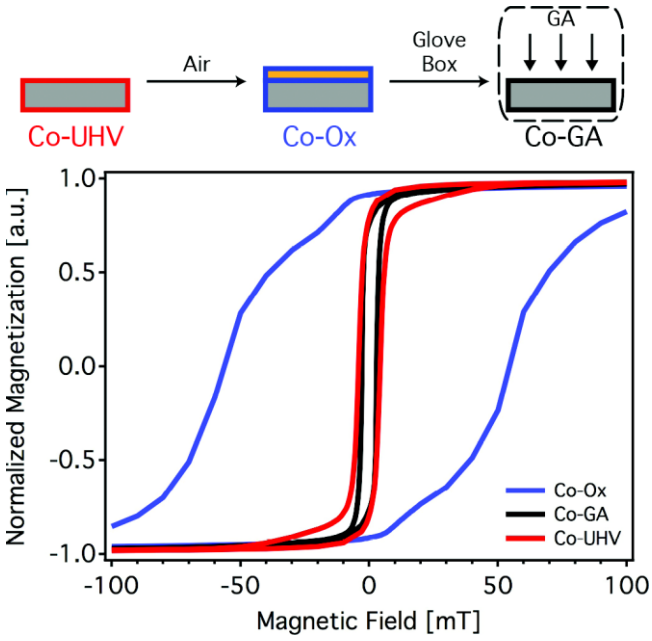

Figure 9 - SQUID characterization of Co samples subjected to different treatments: Co-UHV (red) was completely produced under UHV atmosphere. Co-OX (blue) was exposed to air and then capped with gold. Co-GA (black) was exposed to air, treated with GA inside the glove box and then capped with gold without breaking the inert atmosphere.

Next, we wanted to know if this selective etching process could be extended to other interesting FM materials like Py, whose characteristics have been introduced in the previous chapter. Therefore, analogous experiments to the ones previously performed for Co where carried out with Py. The results are summarized in figure 10. We exposed a set of 4 Py samples with thickness of 18

nm to GA etching in air (Py-Ox) from 0 to 16 hours and the XRR reflectograms were measured, (Figure 10a). We found that the Py layer was completely removed after 16 hours of GA exposure. This correspond to an estimated etching rate of 0.02 nm/min, from which we calculated that approximately 1.5 hours would be needed to etch 2 nm of oxide. As in the case of Co-Ox samples, we attributed the total absence of Py, to the simultaneous formation and etching of Py oxide, due to the presence of oxygen in the etching solution. Then, we tested the GA etching process under inert atmosphere, exposing a set of 3 Py (18 nm) samples to GA solution from 0 to 25 hours. We observed that in this case the thickness decreases and reach a stable value in both samples (exposed respectively for 16 hours and 25 hours), as represented in Figure 10b. The thickness of the etched material was 2 nm, which matches with the reported thickness of Py oxide.[17] We imaged the surface with AFM, as represented in figure 10c. The surface was smooth and clean, like in the Co case. In spite of the similar response presented by Co and Py to GA, there is a huge difference in calculated etching rates (0.6 nm/min and 0.02 nm/min, respectively). This might be attributed to the different nature of the two oxide layers showing that the Py oxide is less reactive towards GA, compared to the Co one.

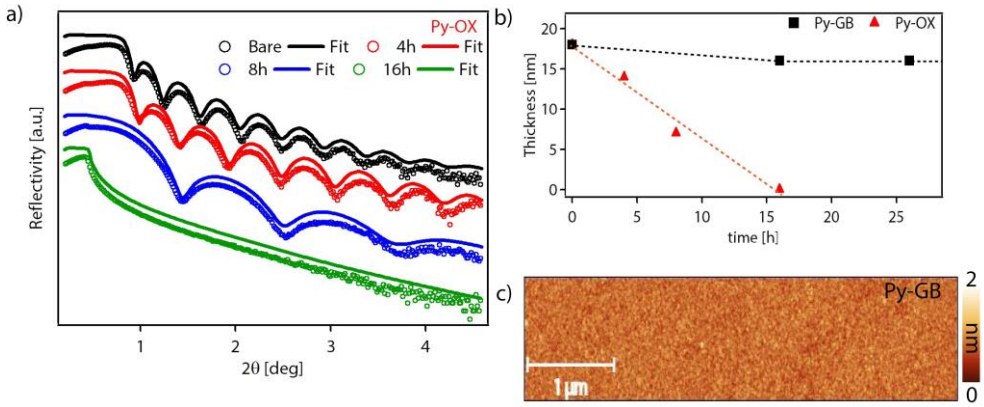

Figure 10 – a) XRR reflectograms of Py samples subjected to different GA etching times in air. b) Comparison of the thickness evolution with etching time for Py samples treated with GA inside a glove box (black) and in ambient atmosphere (red).

A similar set of experiments was carried out on gold capped Py samples, mimicking Co samples represented in figure 7. We recorded high resolution XPS spectra of oxygen and nickel, in gold protected Py (Py-UHV), air oxidized gold protected Py (Py-Ox), and etched gold protected Py (Py-GA). After partially removing the capping Au layer using Ar^+ milling, the Ni2p high resolution XPS displayed a sharp peak centered at 852.6 eV, attributed to metallic nickel. In the case of Py-Ox we also observed a marked shoulder peaking at 855 eV characteristic of nickel oxide/hydroxide contributions.[18] In the oxygen high resolution spectra we also observed two pronounced peaks centred at 529 eV and 531 eV, which as described in chapter 2, can be assigned to nickel oxide and/or hydroxide.[18] The intensity of the O1s signal is 40 times stronger than those observed in Py-UHV and Py-GA.

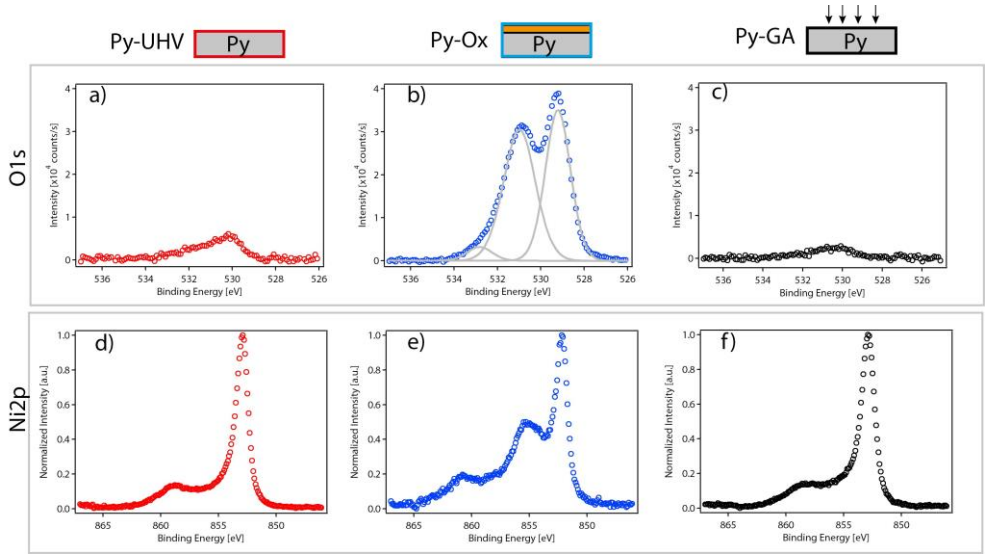

Figure 11 - XPS spectra at the O1s (a-c) and Ni2p (d-f) edges of Py samples subjected to different treatments: UHV (red), oxidized (Ox) (blue), etched GA (black).

We attribute the presence of a small residual oxygen signal in Py-UHV and Py-GA to oxygen contamination in our thermal evaporator. Py films were prepared in Valencia using a thermal evaporator with a base pressure of 10^{-6} mbar. On the other hand, Co films, which showed no trace of residual oxygen were fabricated in collaboration with the Unité mixte de Physique CNRS/Thales (UMR137), in a sputtering system with 10^{-9} mbar base pressure.

3.2.2. Formation of the SAM

After the development of an effective methodology to recover bare metallic surfaces from oxidized FM materials, we focused on our main goal that is the formation of SAMs directly anchored on the ferromagnet to be used as spacer and interface modulators in MTJs. Moreover, the successful growth of the SAM will confirm that GA renders the surface chemically active towards functionalization.

We observed, in the previous section, that the required etching times for Co and Py are different. So, in order to anchor alkanethiol SAMs on their etched surfaces, we decided to design the following common experiment for both materials. We exposed both oxidized surfaces to an ethanolic solution of GA for 15 minutes under inert atmosphere, and after this time, we added a 1 mM ethanolic alkanethiol solution to the same reaction beaker. We dubbed this protocol *mixing methodology*. Blank samples were prepared by exposing the substrate to the ethanolic GA solution and after 15 minutes fresh ethanol was added. We waited for 16 hours and we removed the samples from their solution and washed and blow dried them inside the glove box. We removed the samples from the glove box and immediately characterized them by $w\theta_{CA}$. The results are reported in Table 3.

We obtained $w\theta_{CA}$ for the Py that are comparable with the ones for Co samples, which indicates that the mixing methodology can be used for both surfaces.

Table 3 – $w\theta_{CA}$ obtained with the mixing methodology.

Substrate	Samples	$w\theta_{AA}$ (°)	$w\theta_{RA}$ (°)	Hysteresis
Co	Ø	30	0	30
	C12S	107	99	8
Py	Ø	30	0	30
	C12S	106	99	7

These results confirm that GA treatment is capable of removing the native metal oxide, and also renders chemically active free oxide surfaces towards the reaction with thiols. In all cases, the high CA values obtained agree with those expected for good quality alkyl SAMs of similar length.[7]

In a similar way to that presented in chapter 2, we monitored the variation of the $w\theta_{CA}$ as a function of time. Oxidized Co samples were first exposed to the GA solution for 15 minutes and then the alkanethiol solution was added. Samples were removed from the solution at different times and after washing and blow drying them, we measured the $w\theta_{CA}$ under ambient conditions, within seconds after exposing samples to the air. From contact angle values and using Cassie's Law we estimated the surface coverage (Γ). Results are represented in Figure 12.

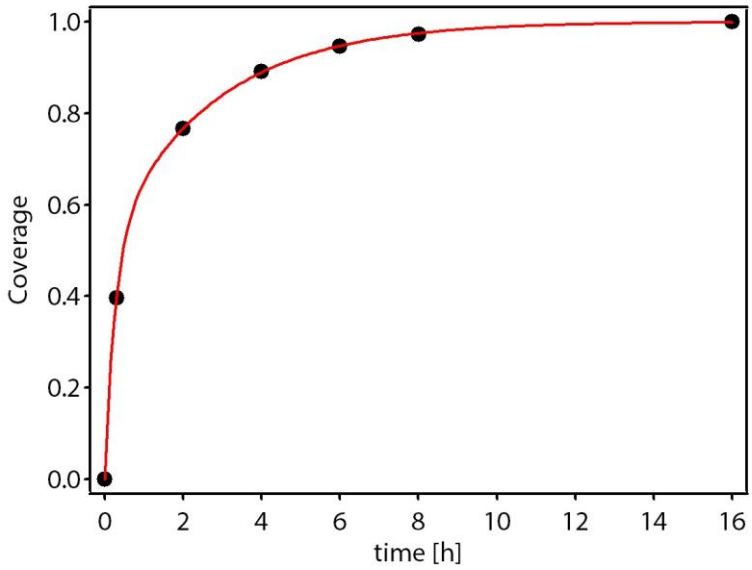

Figure 12 - Coverage as a function of time for Co substrate functionalized with $C_{12}S$ SAM.

In this case, the results can be fitted to a single Langmuir adsorption isotherm:

$$\Gamma = 1 - ae^{-Kt}$$

where Γ is the coverage, *a* is the scaling factor and *K* is a phenomenological rate constant. This rate constant integrates at least three processes that take place in solution: a) etching of the oxide by GA, b) adsorption of the alkanethiolate SAM and c) the reorganization of the SAM into its final state. As can be seen in Figure 13, we obtain 85% coverage of the surface within 3 hours of reaction, suggesting that the absorption of the alkanethiols from the solution to the surface is slower than the absorption of APAs onto air oxidized Py. The complete formation of the monolayer needs more than 13 hours. According to data XRR data (see Figure 3 above), 2 nm oxide etching only takes

a few minutes and is the quickest step. This indicates that the functionalization starts just after the exposure of the metallic surface.

To acquire directly the topography of the functionalized samples, in collaboration with the UMR137 CNRS\Thales, we used an AFM placed inside a glove box. The results are presented in Figure 13.

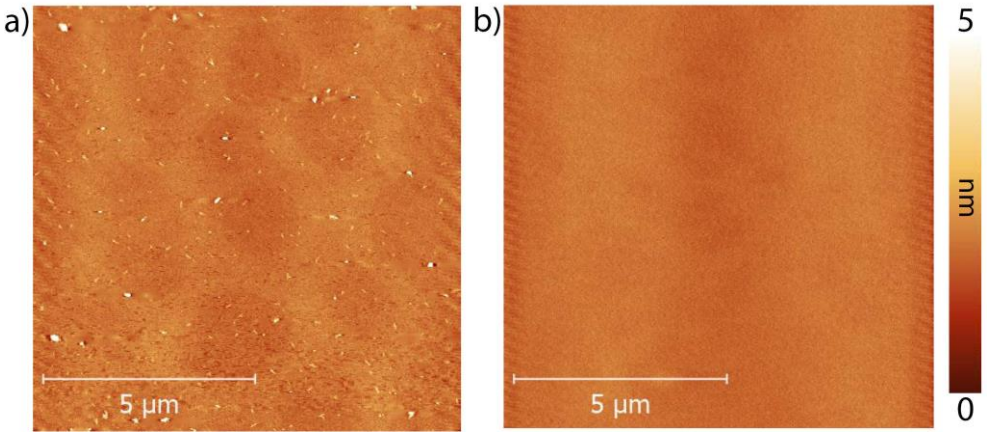

Figure 13 – Topographic AFM images of: C12S functionalized samples Co (a) and Py (b) after 16 hours of reaction taken inside the glove box. The images were FT filtered to remove the 50 Hz electrical noise from the GB.

Both samples appear quite clean, despite Co presents some dirtiness on the surface. The roughness of both the C12S functionalized samples, measured over an area of 10 μm^2, was of 0.30 nm, which is comparable to the one measured in control samples (0.27 nm). The fact that the surface appears clean and smooth, with very hydrophobic $w\theta_{CA}$ values and small hysteresis (Table 3), indicates good quality SAMs. Thus, the implementation of the mixing methodology in the fabrication process of spintronic devices is a viable option. It combines etching and functionalization in a single step and assures a

continuous etching of possible oxide that could be formed if oxide traces are present in the glove box or in the solvents.

3.2.3. Advanced characterization of $C_{12}S$ SAM

We characterized C12S-functionalized Py samples by means of IRRAS. Figure 14 shows the methyl and methylene region of the infrared spectrum of a Py-C12S sample.

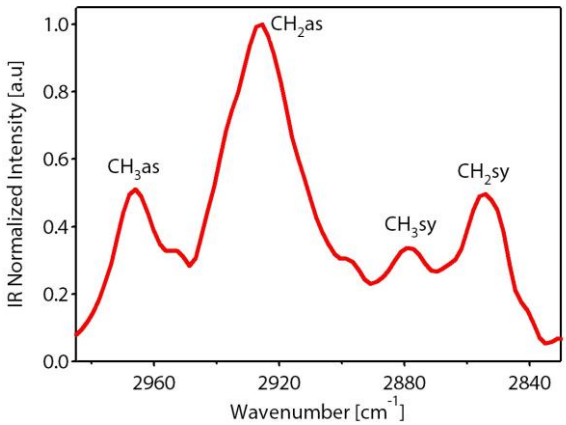

Figure 14 - IRRAS spectrum of a C12S SAM on Py. From left to right the asymmetric methylenes and methyl vibrations and the correspondent symmetric ones.

We observed the characteristic vibrations associated to the asymmetric and symmetric stretching of C-H bonds in methylene and methyl groups. For this SAM-modified Py, the methylene asymmetric frequency is 2925 cm^{-1}, and the symmetric one is 2854 cm^{-1}, while the correspondent values for the methyl stretching are 2966 and 2879 cm^{-1}. These values are close to those reported for SAMs of similar chain-length on Co[7] and nickel,[19] which indicate a more liquid-

like assembly for this short chain. Compared with the values obtained with C12P on Py oxide we find good agreement.

Additional information about the tilt angle (α) with respect to the surface normal has been obtained from the peak intensity ratios between the methylene and methyl asymmetric stretches,[20] following the same methodology used in chapter 2. The correspondent tilt and thickness results are represented in table 4. The reported tilt angle for alkanethiol SAM on Py is similar to that reported for Au, 30°,[21] and deviates from those described for other more reactive metals like silver,[22] copper[14] and platinum[23]: 13°, 15°, and 23°, respectively.

Table 4 – Tilt angle [°] and thickness [Å] of a C12S SAM on Py estimated from the IRRAS spectra using Eq.5 in 2.2.3.

Molecule	Tilt Angle [°]	IR Thickness [Å]	Theoretical Thickness [Å]
$C_{12}S$	29	13	16

In collaboration with the UMR137 we prepared a 5x5 mm^2 sample with the following architecture: 15 nm of Py as bottom electrode, functionalized with C12S using the mixing methodology, followed by the sputtering of 15 nm of Co, protected with a sacrificial layer of 5 nm of aluminium. The whole fabrication was carried out in inert atmosphere. The sample was characterized by means of XAS, at beamline Circe in Alba synchrotron facility. XAS, is a very versatile technique, that has a high elemental sensitivity and is useful for the study of buried interfaces in stacked systems.[24]

We recorded the XAS spectrum at iron and nickel $L_{2,3}$ edges (Figure 15). The difference in the absorption spectra obtained with the two polarizations (dichroism) indicates that the surface of the Py is ferromagnetic at room temperature, which supports the idea that the GA treatment selectively and effectively removes the oxide from the Py surface and the surface does not get oxidized after the functionalization with C12S.

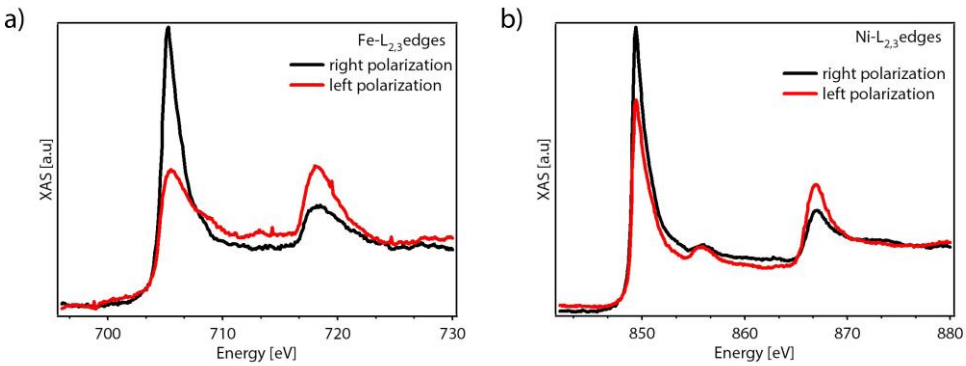

Figure 15 – XAS spectra recorded at Fe-$L_{2,3}$ (a) and Ni-$L_{2,3}$ (b) edges with left polarization (red) and right polarization(black) of a stacked Py//C12S/Co/Al sample after glycolic acid treatment and functionalization with C12S.

In order to study the magnetic coupling between the two FM electrodes, we took advantage of XMCD coupled with a photoemission electron microscope (PEEM), to obtain images with magnetic contrast. We first saturated the electrodes by applying a magnetic field of 7 mT to the sample; then, we decreased the field until reaching the demagnetization. At this point we observed the presence of a defined domain wall, between the zone where the magnetization followed the applied field, and the other one where the magnetization is still free. We recorded the magnetic images at L3 edges of cobalt, iron and nickel, in sequence without changing the magnetic field, as is

shown in Figure 16. One can see that the position of the domain wall did not change in the three images, which demonstrates that the two electrodes are ferromagnetically coupled, switching at the same time when a magnetic field is applied.

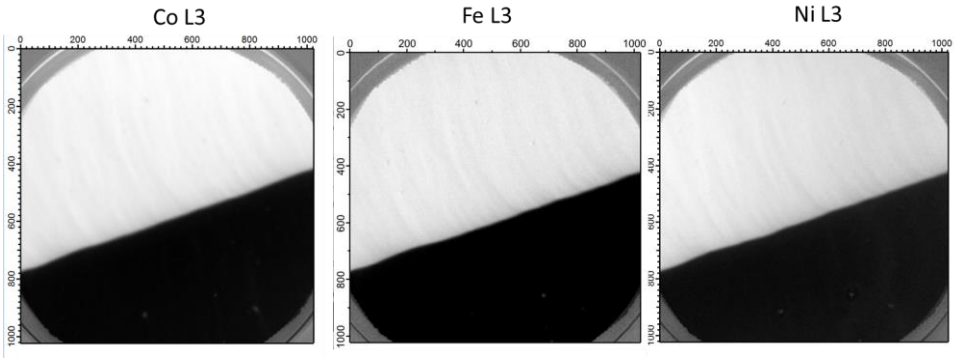

Figure 16 - XMCD-PEEM images recorded at Co, Fe and Ni L3 edges.

3.2.4. Extending the functionalization

We continued the study of the formation of longer alkanethiol SAMs on Co and Py using the mixing methodology. We functionalized three Co and Py substrates with alkanethiols from 1-tetradecanethiol (C14S) to 1-octadecanethiol (C18S) and measured $w\theta_{CA}$ after 16 h. The average results for both surfaces are reported in table 5.

Table 5 - $w\theta_{CA}$ of functionalized Co and Py samples with different CnS

Molecule	$w\theta_{AA}$ [°]	$w\theta_{RA}$[°]	Hysteresis
Co-C_{14}S	109	103	6
Co-C_{16}S	112	104	8
Co-C_{18}S	118	105	13
Py-C_{14}S	111	102	9
Py-C_{16}S	113	103	10
Py-C_{18}S	116	105	11

A dependence of the contact angle with the chain length can be clearly observed. As shown in the chapter 2 for APA SAMs, the clear progression of the contact angle is related with an increase of the quality of the SAM as the alkyl chain length increases. However, we observed that the hysteresis in the $w\theta_{CA,}$ follow an unexpected trend with respect of the SAMs formed in the previous chapter. Usually when the chain used to form a SAM is longer, the hysteresis is smaller. In our case we observe for both surfaces that the hysteresis increases with the chain length.

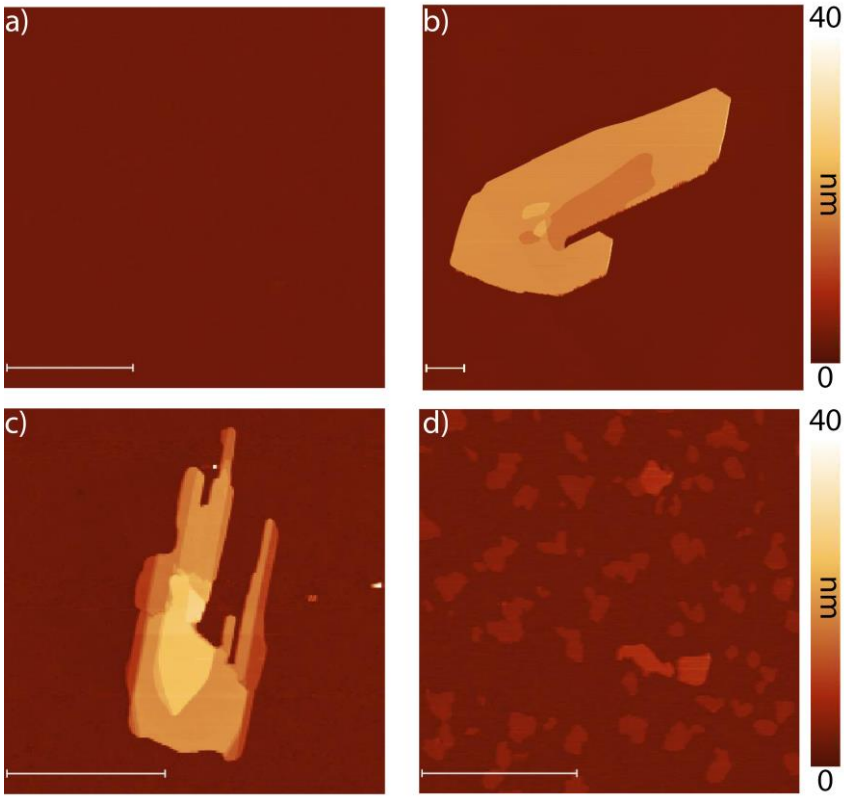

Figure 17 - AFM topographic images of Co functionalized with: a) C12S, b) C14S, c) C16S and d) C18S. The scale bar is 5 µm.

When we examined the set of Co and Py samples functionalized with alkanethiol (C12S–C18S) using the AFM under ambient conditions, we noticed that despite the air exposed C12S sample presented a smooth surface, comparable to that measurement carried in the glove box, upon air exposure of C14S, C16S and C18S samples, lamellar domains were formed on the surface. Similar results were obtained also for Py. The next chapter will be focused on the characterization of these features.

3.2.5. Fabrication of MTJ devices based on FM electrodes and SAMs

As introduced before, I did a 3 months stay at the UMR137 in Palaiseau under the supervision of Prof. Pierre Seneor and Dr. Richard Mattana. During this period I learned how to prepare spintronic devices using the nanoindentation assisted by AFM technique, which had been successfully used before for the preparation of LSMO//CnP/Co devices.[25–27] We wanted to test if the combination of chemical oxide etching, developed above, and AFM assisted nanoindentation was valid to prepare Co,Py//CnS/FM MTJs.

The technique, represented in Figure 18, is based on four steps: i) deposition by spin-coating of a resistive polymer matrix on the air oxidized FM surface, ii) nanoholes are fabricated by indentation, with the help of the AFM, iii) on the exposed surface the native oxide etching process with GA and the alkanethiol functionalization are carried out inside a glove box, iv) the last step is the evaporation of the top electrode without breaking the controlled atmosphere.

The nanoindentation is performed using a modified conductive tip AFM, which monitors in real time the resistance between the tip and the FM electrode. The photoresist used is highly resistive, and depending on the depth reached the resistance changes drastically. This enables a high control on the contact made during the fabrication. With this technique the risk of short-circuit of the device is decreased due to the small area (20 nm^2) of each contact.

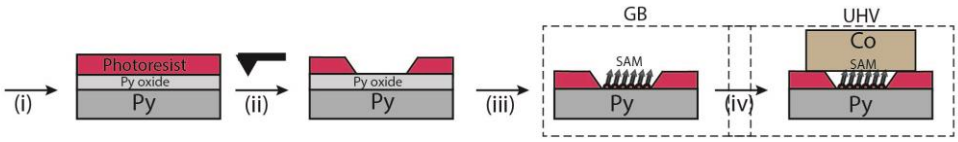

Figure 18 - Nanoindentation process for the preparation of a Py//SAM/Co MTJ: (i) deposition of photoresist, (ii) fabrication of nanoholes, (iii) etching of the oxide and functionalization of the metallic surface and (iv) top electrode deposition.

Delprat,[28] has recently confirmed at the UMR137 the potential for spintronics of FM1/CnS//FM2 MTJs following the methodology described above. Figure 19 shows current-voltage (I-V) and resistance-magnetic field (R-H) curves of a Py//C16SH/Co MTJ. The device displays a resistance of ~ 85 kOhm at 0.2 V and a non-linear I-V response expected for a non short-circuited contact. Interestingly, R-H curves denote the presence of TMR values up to 12% at room temperature at a bias voltage of 100 mV. These preliminary results are useful to demonstrate that the developed methodology can be integrated into the fabrication of room temperature molecular MTJs.

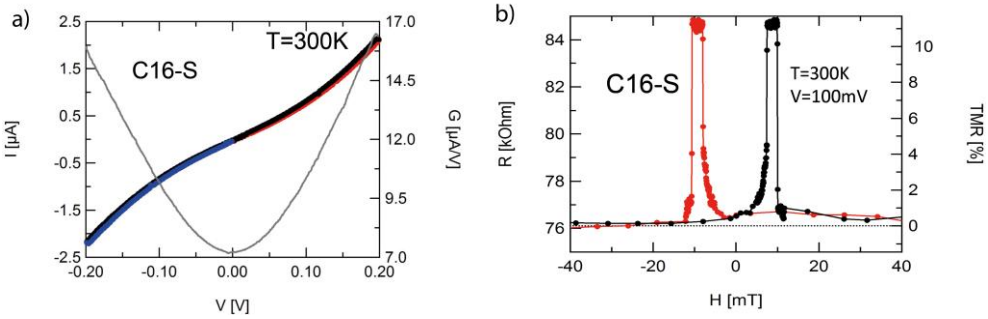

Figure 19 - Electrical characterization of the fabricated junction (Py//C16S/Co/Al): a) I-V curve that demonstrates the tunneling regime and b) R-H that shows TMR at room temperature.

3.3. Conclusions

We have developed a novel methodology to recover already oxidized ferromagnetic Co and Py surfaces by selectively removing the native oxide by means of a wet chemical etching with GA. This process avoids the use of complicated UHV approaches or physical methods and is compatible with common lithographic techniques. We have characterized both etched surfaces by means of different characterization techniques such as XRR, XPS and SQUID magnetometry to check that this treatment does not affect the properties of the metallic bulk. Then, we have moved towards the functionalization of the surfaces with alkanethiols. We have observed that if the functionalized surfaces are kept in inert atmosphere it is possible to use this method to build molecular spintronic devices, which exhibit tunnel magnetoresistance at room temperature. However, if these surfaces are exposed to air, lamellar domains start appearing on it. The characterization of these strange and unexpected features will be described in the next chapter.

3.4.References

1. Finazzi, M., Duò, L. & Ciccacci, F. Magnetic properties of interfaces and multilayers based on thin antiferromagnetic oxide films. *Surf. Sci. Rep.* **64,** 139–167 (2009).

2. Sanvito, S. Molecular spintronics: The rise of spinterface science. *Nat. Phys.* **6,** 562–564 (2010).

3. Galbiati, M. *et al.* Spinterface: Crafting spintronics at the molecular scale. *MRS Bull.* **39,** 602–607 (2014).

4. Nuzzo, R. G., Fusco, F. A. & Allara, D. L. Spontaneously organized molecular assemblies. 3. Preparation and properties of solution adsorbed monolayers of organic disulfides on gold surfaces. *J. Am. Chem. Soc.* **109,** 2358–2368 (1987).

5. Schoenfisch, M. H. & Pemberton, J. E. Air stability of alkanethiol self-assembled monolayers on silver and gold surfaces. *J. Am. Chem. Soc.* **120,** 4502–4513 (1998).

6. Hutt, D. A. & Liu, C. Oxidation protection of copper surfaces using self-assembled monolayers of octadecanethiol. *Appl. Surf. Sci.* **252,** 400–411 (2005).

7. Devillers, S., Hennart, A., Delhalle, J. & Mekhalif, Z. 1-Dodecanethiol Self-Assembled Monolayers on Cobalt. *Langmuir* **27,** 14849–14860 (2011).

8. Hoertz, P. G., Niskala, J. R., Dai, P., Black, H. T. & You, W. Comprehensive Investigation of Self-Assembled Monolayer Formation on Ferromagnetic Thin Film Surfaces. *J. Am. Chem. Soc.* **130,** 9763–9772 (2008).

9. Mekhalif, Z., Riga, J., Pireaux, J.-J. & Delhalle, J. Self-Assembled Monolayers of n-Dodecanethiol on Electrochemically Modified Polycrystalline Nickel Surfaces. *Langmuir* **13,** 2285–2290 (1997).

10. Galbiati, M. *et al.* Recovering ferromagnetic metal surfaces to fully exploit chemistry in molecular spintronics. *AIP Adv.* **5,** (2015).

11. Senthil kumar, K. *et al.* Fabrication of ultra-smooth and oxide-free molecule-ferromagnetic metal interfaces for applications in molecular electronics under ordinary laboratory conditions. *RSC Adv.* **7,** 14544–14551 (2017).

12. Vogt, A. D., Han, T. & Beebe, T. P. Adsorption of 11-Mercaptoundecanoic Acid on Ni(111) and Its Interaction with Probe Molecules. *Langmuir* **13,** 3397–3403 (1997).

13. Rajalingam, S., Devillers, S., Dehalle, J. & Mekhalif, Z. A two step process to form organothiol self-assembled monolayers on nickel surfaces. *Thin Solid Films* **522,** 247–253 (2012).

14. Caipa Campos, M. A. *et al.* Self-Assembled Functional Organic Monolayers on Oxide-Free Copper. *Langmuir* **27,** 8126–8133 (2011).

15. Smardz, L., Köbler, U. & Zinn, W. Oxidation kinetics of thin and ultrathin cobalt films. *J. Appl. Phys.* **71,** 5199–5204 (1992).

16. Svalov, A. V *et al.* Influence of temperature on structure and magnetic properties of exchange coupled TbCo/FeNi bilayers. *J Nanosci Nanotechnol* **12,** 7566–7570 (2012).

17. Nahrwold, G. *et al.* Structural, magnetic, and transport properties of Permalloy for spintronic experiments. *J. Appl. Phys.* **108,** 13907 (2010).

18. Pollak, R. A. & Bajorek, C. H. Surface composition and chemistry of evaporated Permalloy films observed by x–ray photoemission spectroscopy and by Auger electron spectroscopy. *J. Appl. Phys.* **46,** 1382–1388 (1975).

19. Mekhalif, Z., Laffineur, F., Couturier, N. & Delhalle, J. Elaboration of Self-Assembled Monolayers of n-Alkanethiols on Nickel Polycrystalline Substrates: Time, Concentration, and Solvent Effects. *Langmuir* **19,** 637–645 (2003).

20. Greenler, R. G. Infrared Study of Adsorbed Molecules on Metal Surfaces by Reflection Techniques. *J. Chem. Phys.* **44,** 310–315 (1966).

21. Nuzzo, R. G. & Allara, D. L. Adsorption of bifunctional organic disulfides on gold surfaces. *J. Am. Chem. Soc.* **105,** 4481–4483 (1983).

22. Schreiber, F. Structure and growth of self-assembling monolayers. *Prog. Surf. Sci.* **65,** 151–256 (2000).

23. Petrovykh, D. Y. *et al.* Alkanethiols on platinum: multicomponent self-assembled monolayers. *Langmuir* **22,** 2578–87 (2006).

24. Lee, J. R. I. *et al.* X-ray absorption spectroscopy for the structural investigation of self-assembled-monolayer-directed mineralization. *Methods Enzymol.* **532,** 165–187 (2013).

25. Bouzehouane, K. *et al.* Nanolithography Based on Real-Time Electrically Controlled Indentation with an Atomic Force Microscope for Nanocontact Elaboration. *Nano Lett.* **3,** 1599–1602 (2003).

26. Tatay, S. *et al.* Self-assembled monolayer-functionalized half-metallic manganite for molecular spintronics. *ACS Nano* **6,** 8753–8757 (2012).

27. Galbiati, M. *et al.* Unveiling self-assembled monolayers' potential for molecular spintronics: Spin transport at high voltage. *Adv. Mater.* **24,** 6429–6432 (2012).

28. Delprat, S. Jonctions tunnel magnétiques avec des monocouches moléculaires auto-assemblées. (Université Pierre et Marie Curie, 2017).

4 Characterization of lamellar alkanethiolate domains on ferromagnetic surfaces

4.1. Introduction

In the previous chapter, we have studied a novel method to recover oxidized Co or Py FM surfaces under inert conditions using GA to selectively etch the native oxide leaving a clean metallic surface. As summarized in Figure 1, the new exposed material was chemically active and could be functionalized with alkanethiols of different chain lengths (CnS n= 12, 14, 16 and 18). The resulting SAMs were stable for days under inert atmosphere. However, when these functionalized surfaces (CnS with n>12) were exposed to the air, island-like domains that could be easily distinguished by optical microscopy rapidly appear on the surface.

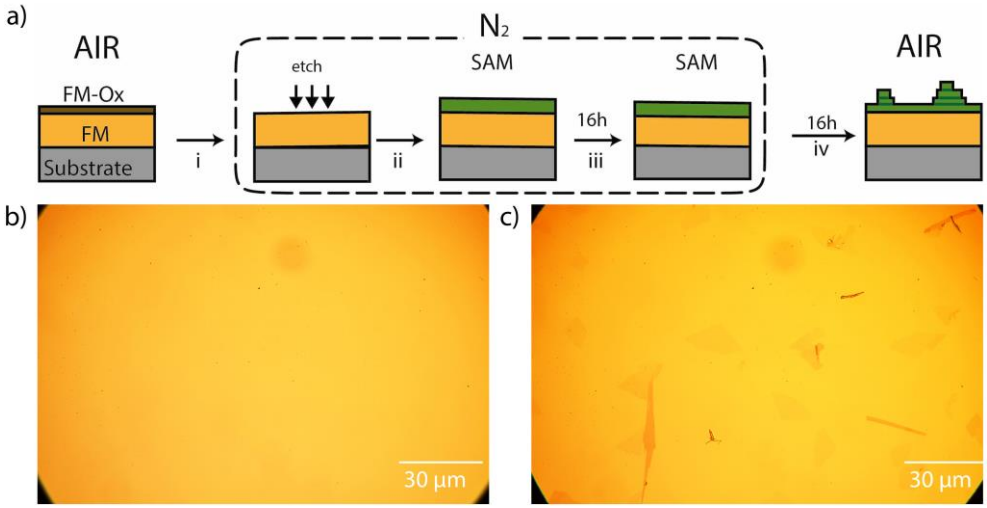

Figure 1 – a) Pictorial representation of island-like domain formation on an alkanethiol functionalized FM sample: i) Etching of native oxide layer on the FM with GA, ii) grafting of the CnS SAM, iii) functionalized films stable under inert atmosphere, iv) islands grow as the sample is exposed to air. b-c) Optical images of a functionalized Co surface with C14S just after functionalization (b) and after 16h of air exposure (c).

When we studied the islands formed on our samples with more detail by AFM (Figure 2) we noticed that these domains show a layered structure, as highlighted by the height distribution represented in Figure 2c. Although, the formation of oxide islands on some bare metals, such as aluminium[1] and cobalt[2] had been reported previously in literature, the fact that our reference samples (i.e. prepared exactly the same way but without thiol SAM) do not evolve into islands formation motivated us to look for alternative explanations about the nature of the observed features.

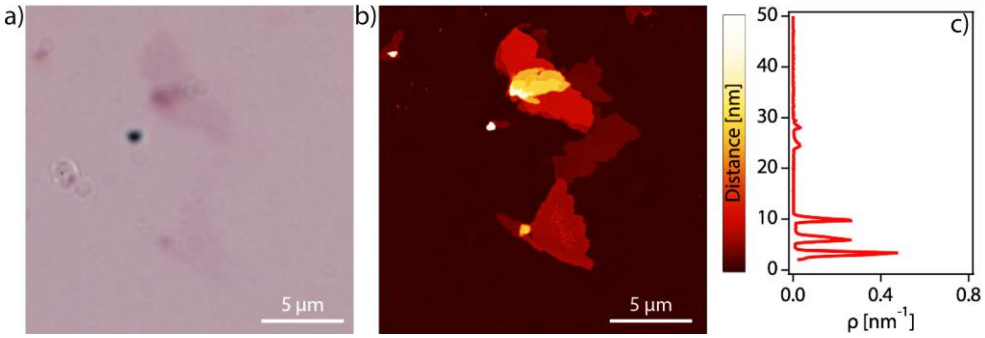

Figure 2 - Combined Optical - AFM characterization of a functionalized Co-C14S sample: a) Optical microscopy. b) AFM topographic image and c) height distribution of b.

The layered structure found in the domains formed over our FM surfaces suggested that maybe the islands were Lamellar Metal-alkanethiolates (LMAs) directly grown over the surface. LMAs, as bulk materials, are known since long time ago and have been prepared using different metals like silver,[3–9] palladium,[10–14] nickel,[15–17] and gold[18–21] to give material of general $M^{n+}(CnS)_n$ stoichiometry, where R is an alkyl chain and n = 1 or 2 depending on the metal valence. In the particular case of copper, apart from lamellar metal-alkanethiolates,[24,25] lamellar metal alkanesulfonates with an analogous structure have also been reported.[26,27] More recently, two papers on surface bound silver LMAs have been reported by Hu et al.[22,23] In both cases, the authors evaporated small amounts of silver onto a silicon substrate, obtaining an incomplete film formed by isolated silver nanoparticles, that they functionalized in a second step with alkanethiols. Finally, they performed an annealing treatment under UHV to obtain LMAs, as the major product on the surface (Figure 3).

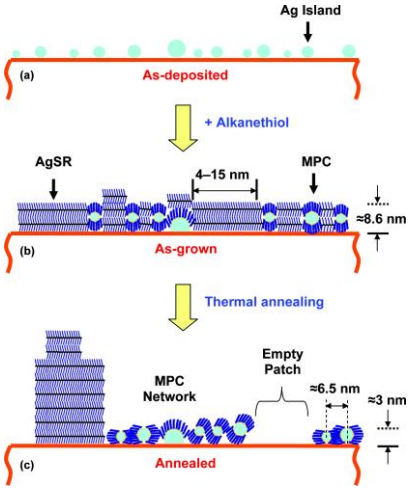

Figure 3 - Figure extracted from reference 23, which displays the formation of LMAs from silver nanoparticles.

LMA structure is generally described as formed by the stacking of slabs with a central metal-sulfur backbone, sandwiched between two alkyl chains, as represented in Figure 4.

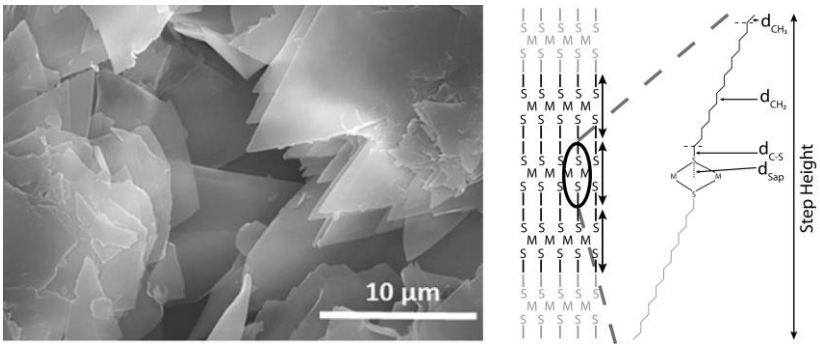

Figure 4 - SEM image of a Ag(CnS) LMA extracted from ref 8 (n = 16). Cartoon representing the structure of a $M(SR)_2$ lamellar metal-alkanethiolate. The thickness of a single LMA slab is the result of the contributions from the methylene chain (d_{CH_2}), terminal methyl group (d_{CH_3}), carbon-sulfur ($d_{C\text{-}S}$) and metal-sulfur (d_{Sap}) bond distances.

The scope of this chapter will be to elucidate by means of different surface techniques if the real nature of the domains spontaneously formed over our FM substrates correspond to that of LMA and to try to understand the origin and factors controlling the growing process.

4.2. Results and discussion

4.2.1. Structural Studies

In order to perform a detailed study about the structure of the domains, first we used AFM to obtain local quantitative topographic 3D information. Figure 5 shows the topographic images and the corresponding height distributions of islands formed from C14S, C16S and C18S alkanethiol samples. In all cases, the presence of multiple levels with defined step height is evidenced.

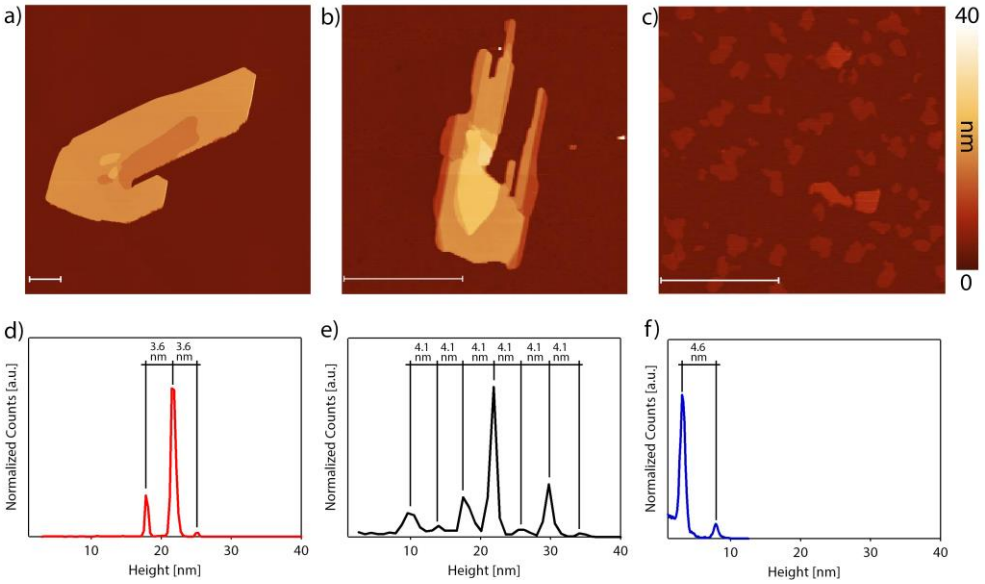

Figure 5 - AFM topographic images and height distribution profiles of islands obtained with C14S (a and d), C16S (b and e) and C18S (c and f). The difference between the black lines corresponds to the step heights. The scale bar is of 5 µm.

By measuring **step heights** (SH) on at least 6 islands of each chain length on Co and Py, we obtained an estimation of the most probable step height for each case (Figure 6b). Although no remarkable differences between equivalent SAM functionalized Co and Py samples were noticeable, a clear increase with the number of carbon atoms was observed, indicating that the islands contain alkanethiol chains. Thus, the islands formed from C14S show an average step height of 3.6 nm, which increases to 4.1 nm for those based on C16S and finally to 4.5 nm for those based on a C18S (Figure 6 and Table 1).

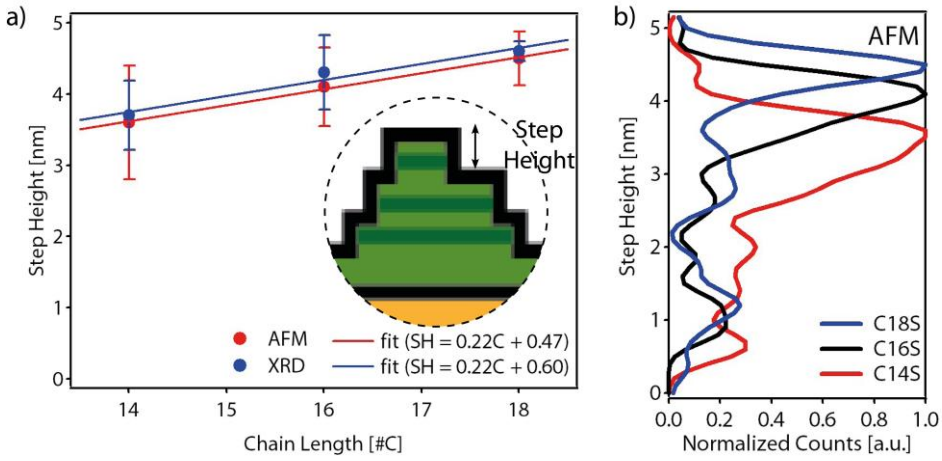

Figure 6 – a) Step height versus chain length of M-CnS island domains determined from AFM (red dots, M = Co and Py) and XRD (blue dots, M = Co). Solid lines are linear fits to the data (SH = mC + b, C = number of carbons). Fitted values are displayed as an inset. b) Step height distribution obtained after measuring individual step heights in 6 islands of each chain length on Co and Py. AFM error bars in a) are calculated as Gaussian fit from b). The error bars for XRD were calculated from the average of at least 2 different XRD measurements as those displayed in Figure 7.

As can be seen, there is a clear dependence between the alkanethiol chain length and the step height of the obtained islands, which indicates that the materials share a common structure.[5,7]

In order to have a further experimental proof on the layered nature of the island domains and the step height values, we also run a series of out-of-plane XRD measurements at Diamond Light Source BI07 beam line. To minimize FM layer contribution, we covered several silicon substrates with only 4 nm of cobalt (usually we worked with 15 nm thickness). Then samples were functionalized with C14S, C16S and C18S, exposed to the air and the XRD data recorded. Representative diffractograms are showed in Figure 7.

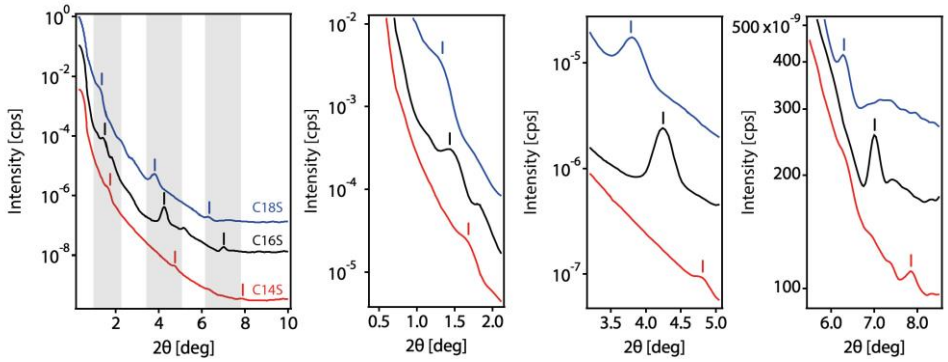

Figure 7 – Out-of-plane XRD measurements on Co-CnS samples: C14S (red), C16S (black) and C18S (blue).

We observe for all the samples three equally spaced diffraction peaks. The interlayer spacing determined from this periodicity, after applying the Bragg's law ($2dsin\theta = n\lambda$),[28] with n equal to 1 and λ equal to 0.9918 Å (C18S Δ2θ = 2.47 deg; d = 23 Å, C16S Δ2θ = 2.64; d = 21.50 Å, C14S Δ2θ = 3.07; d = 18.5 Å) closely correspond to half of the step height determined by AFM (Figure 6, blue dots).

Table 1 - Step height estimated from AFM and XRD measurements and predicted all-trans SAM thickness. The XRD Step heights have been calculated as two times the interlayer spacing determined from XRD measurements.

Material	AFM Step Height [nm]	XRD Step Height [nm]	SAM thickness [nm]
M-C14S	3.6	3.7	1.7
M-C16S	4.1	4.3	1.9
M-C18S	4.5	4.6	2.1

Next, we studied the **average height** of the islands. From the AFM height distribution measured in at least 5 samples of each chain length over Co and Py and considering the average step height for a C14S, C16S and C18S alkyl chain equal to 3.6 nm, 4.1 nm and 4.6 nm, respectively, as obtained from the experimental data, we computed the height (number of layers) histograms represented in Figure 8. Yellow dashed lines in this figure are the histogram integrals.

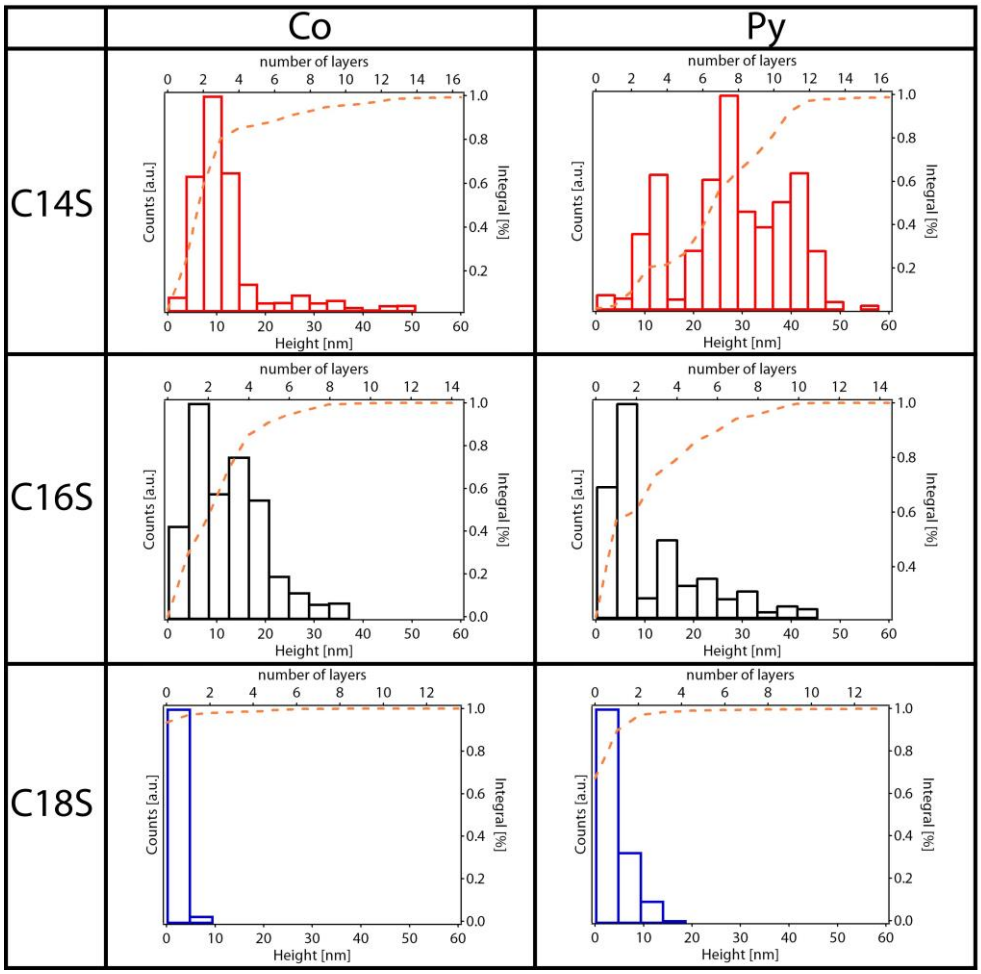

Figure 8 - AFM height statistics of island features: C14S(red), C16S (black) and C18S (blue). Yellow dashed line corresponds to the integral of the histogram.

From the histograms, we extracted the average height of the islands formed for each alkyl chain and P_{85} and P_{50}. $P_{85(50)}$ represents the island height below which 85(50)% of observations fall. Analyzing P_{85} values presented in Table 2, for Co and Py, there is a clear trend: C14S islands are thicker while C18S in most

cases are formed by a single layer. Moreover, islands of Co are thinner than those observed on Py.

Table 2 – Statistical parameters from histograms in Figure 8.*Number of layers values are calculated from P_{85}.

Material	Average Height [nm]	P_{85} [nm]	Number of layers*	P_{50} [nm]
Co-C14S	12.2	18	5	7.2
Co-C16S	18.5	16.4	4	10
Co-C18S	4.6	4.6	1	-
Py-C14S	19.8	39.6	11	25.2
Py-C16S	14.2	20.5	5	4.1
Py-C18S	4.6	4.6	1	-

The above results support that: i) alkyl chains form part of the structure of the lamella, ii) our lamellae present out-of-plane crystallinity and iii) the assembly of alkyl thiol chains results in the formation of layered structures with step heights fixed by the length of the organic molecules, which will be in accordance with the LMA structure proposed in Figure 4.

Moreover, this clear dependence with the alkyl chain length rules out the idea of metal oxide as main component of the islands and supports the possibility that during the oxidation of the surface beneath the formed SAM (air exposure), there is a reorganization of the organic molecules into lamellar alkanethiolate domains formed by metal ions, extracted from the metal surface, upon oxidation which are coordinated by the organic molecules.

If we assume that our islands are in fact the result of the growth of LMAs directly on surfaces, as suggested by the observed dependence of the step height on the chain length, it is possible to build a structural model based on step height data, represented in Figure 4. The total Step Height should be the sum of the contributions coming from: 1) the methylene chain ($(n-2)\cdot d_{CH_2}$), being d_{CH_2} the vertical C-C distance and n the number of carbons in the chain and 2) d_o, that represents the contribution provided by the sum of the distance from the S atom to the metal plane (d_{Sap}), the C-S bond distance (d_{C-S}) and the terminal methyl group (d_{CH_3}). That is:

$$\text{Step Height} = 2\cdot[(n-2)\cdot d_{CH_2} + d_o]$$

$$d_o = d_{Sap} + d_{C-S} + d_{CH_3}$$

We used the results from the linear fitting of the AFM step height displayed in Figure 4 to obtain the following values: $d_{CH_2} = m = 0.22$ nm and $2d_o = b + 2d_{CH_2} = 0.917$ nm. Assuming that the CH_2 groups in the alkyl chain are fully stretched, and taking into account that the theoretical carbon-carbon vertical distance is $d_{C-C} = 0.127$ nm,[7] from d_{CH_2} we can estimate a chain tilt angle of 30°. This value is close to the expected value for close packed alkyl chains on gold.[29] From the theoretical carbon sulfur bond length $d_{C-S} = 0.182$ nm,[8] and the theoretical van der Waals radii of the methyl group $d_{CH_3} = 0.21$ nm,[8] which is calculated from the average value of the distance between the carbon located before the methyl carbon and the last hydrogen(s) that points up to the next layer, we can derive $d_{Sap} = 0.068$ nm.

In Table 3 we summarize the d_{CH_2} and $2d_o$ values calculated from the Step Heights reported in the literature for bulk nickel, palladium and silver LMAs. As can be observed our values are not far from some of those previously reported.

Table 3 - d_{CH_2} and d_{CH_2} obtaianed from our AFM and XRD data compared with values obtained from the literature for bulk LMAs.

Material	d_{CH_2}[nm]	$2d_o$[nm]	Tilt Angle [°]	Ref	Compound
Ni	0.258	0.78	0	16	Ni(SR)2
Pd	0.248	0.81	14	14	Pd(SR)2
Ag	0.248	0.98	14	5	AgSR
Ag	0.250	0.97	12	9	AgSR
Ag	0.241	1. 02	19	7	AgSR
Ag	0.242	1. 05	19	8,26,27	AgSR
Py/Co (AFM)	0.225	0.92	30	This thesis	
Co (XRD)	0.225	1.05	30	This thesis	

Additionally, we performed a search in the Cambridge Structural Database (CSD) (23/11/2016) for motives including μ_2S–M and μ_3S–M bridges where M=Co, Fe and Ni. From this query, we obtained 5739 and 43 hits, respectively. The average values for d_{Sap}, in the case of μ_2S–M and μ_3S–M bridges, are respectively 0.070 nm and 0.092 nm. Thus, we observed that our d_{Sap} value calculated from AFM data (0.068 nm), matches with the crystallographic database for μ_2S–M bridges coordination. If we repeat the calculation using XRD data, however, our final value for d_{Sap} is 0.133 nm, which would indicate μ_3S–M bridges. As a result, and due to the experimental error, we cannot

extract further information about sulfur coordination in island domains. Nevertheless, we can assume that S is μ_3-coordinated and that binds to the metal plane forming a regular pyramid with a triangular base. These will result in a distorted hexagonal network packing, formed by octahedral MS_6 sites showing edges with half of the S atoms above and below the plane formed by the M atoms, as represented in Figure 9. This kind of packing is the same that the one adopted by layered double hydroxides (LDHs) and by hexagonal transition metal dichalcogenides (TMDCs).

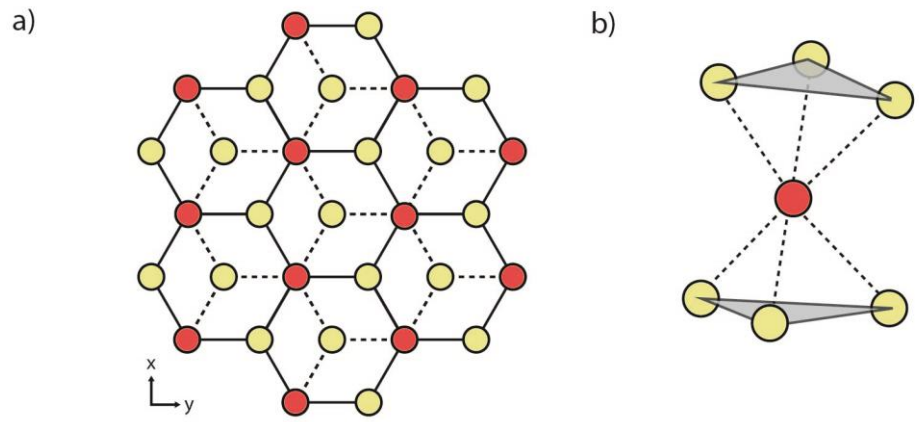

Figure 9 – a) Top view of a schematic representation of the metal-sulfur regions. Metal atoms are represented in red, sulfur atoms above and below the backbone plane are in yellow and b) octahedral coordination of the metal atom.

Next, we will analyze the amount of material that migrates from the interfacial SAM to form the lamellar structures during the growing process. For the case of C18S, the calculations are easier. In the Figure 10, the islands present on the cobalt surface functionalized with C18S have 3 layers with defined heights: the first one has 3.8 nm, and the second and the third ones, 8.4 and 13 nm, respectively. These layers cover respectively 16%, 2.35 % and 0.70% of the total

image area. Assuming that the area per molecule is the same in an island and in the original SAM, in order to calculate the total equivalent coverage, we need to multiply each value respectively by 2, 4 and 6 and sum all the resulting areas, which gave us an equivalent coverage value of 45.62%. This result means that only about 50% of the molecules that composed the original SAM have migrated into the island, and that the space between the islands is not completely void. Unfortunately, this simple analysis cannot be carried out for C14 and C16 samples because the number of islands imaged in a convectional AFM pictures is not high enough to obtain meaningful values. Another interesting thing that can be observed from the height histogram in Figure 10d, is the presence of the first peak at 3.8 nm for the case of C18S, when the calculated value for the step height is of 4.6 nm. This suggests the presence of partial interdigitation between the island domains and the SAM beneath. This behaviour is only observed with this chain length.

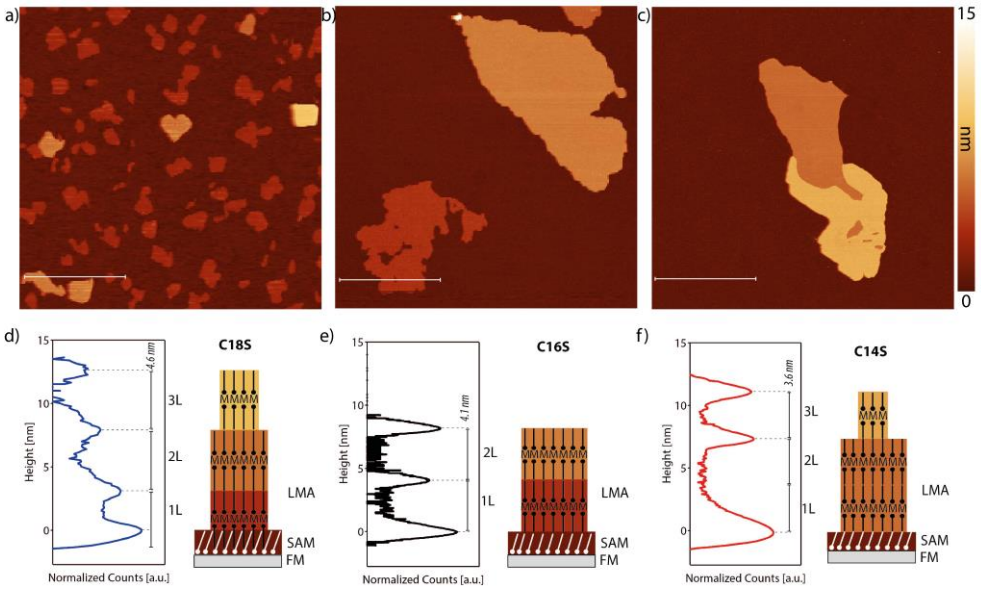

Figure 10 - AFM images of islands grown on Co from different alkanethiolates with their respective height histogram: C18S (a-d) , C16S (b-e) and C14S (c-f). The scale bar is of 5 µm.

4.2.2. Area distribution studies

The islands domains were also imaged using microscopy techniques other than AFM (i.e. Optic and SEM) in order to gain further information on their width distributions and to estimate coverage values. Figure 11 shows images of a C14S island grown on Py taken by means of atomic force, optical and scanning electron microscopies. As can be seen, the height contrast observed in the optical images is very weak (Figure 11b), but when the amount of light that reaches the detector is reduced by means of a neutral-density filter (ND) it improves considerably (Figure 11c). The alternative use of SEM was not so effective, (Figure 11d) as these images showed poorer height contrast. Moreover, we observed material damage after prolonged electron beam exposure, using 20 kV as acceleration voltage.

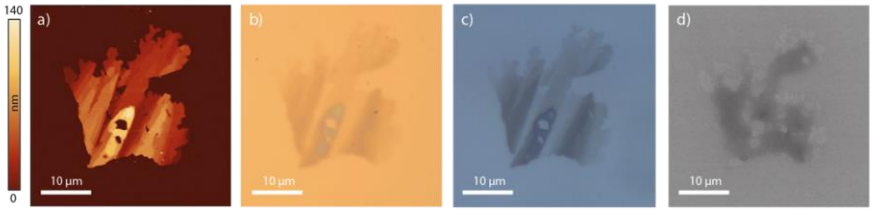

Figure 11 – A C14S island on Py imaged with different techniques a) AFM, b) Optical Microscope, c) Optical Microscope with ND Filter and d) SEM.

Although AFM is a very precise technique, and the only one that really gives true topographic information of the sample, it is not suited to study large surface areas (above 50-100 μm^2), and for that reason we used optical microscopy to study domain size distributions.

To perform a statistical analysis, first we prepared 3 Co and 3 Py samples with SAMs of each chain length (CnS, n= 14, 16 and 18) and imaged at least 3 different areas of each sample using optical microscopy. Representative optic images are showed in Figure 12. At a first glance, it is possible to observe that alkyl chain length has an important influence on the size and number of the formed domains.

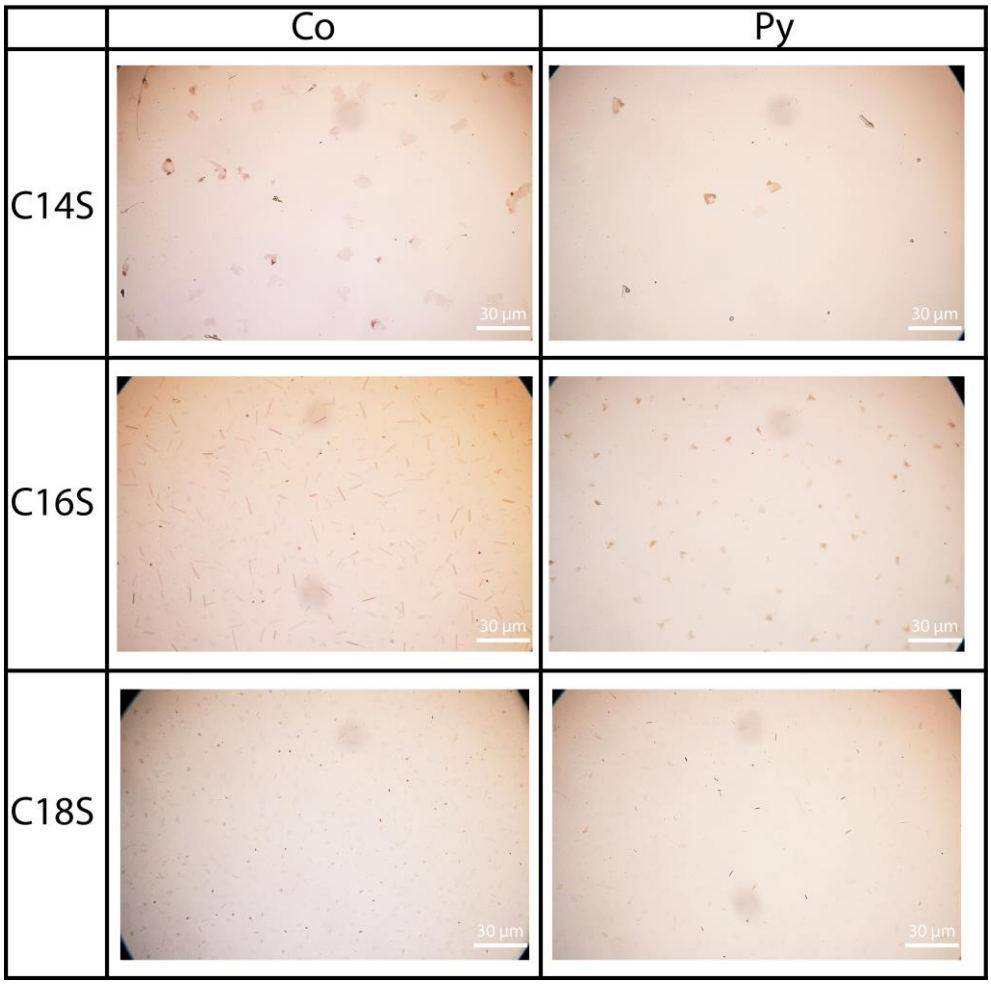

Figure 12 - Representative 100x optic images of Co and Py functionalized samples.

Using an imaging processing software (Gwyddion[31]) we calculated domain area histograms for each chain length. For the C14S and C16S we used 433x380 μm^2 images, while for C18S we used 253x190 μm^2 images. Results are presented in Figure 13.

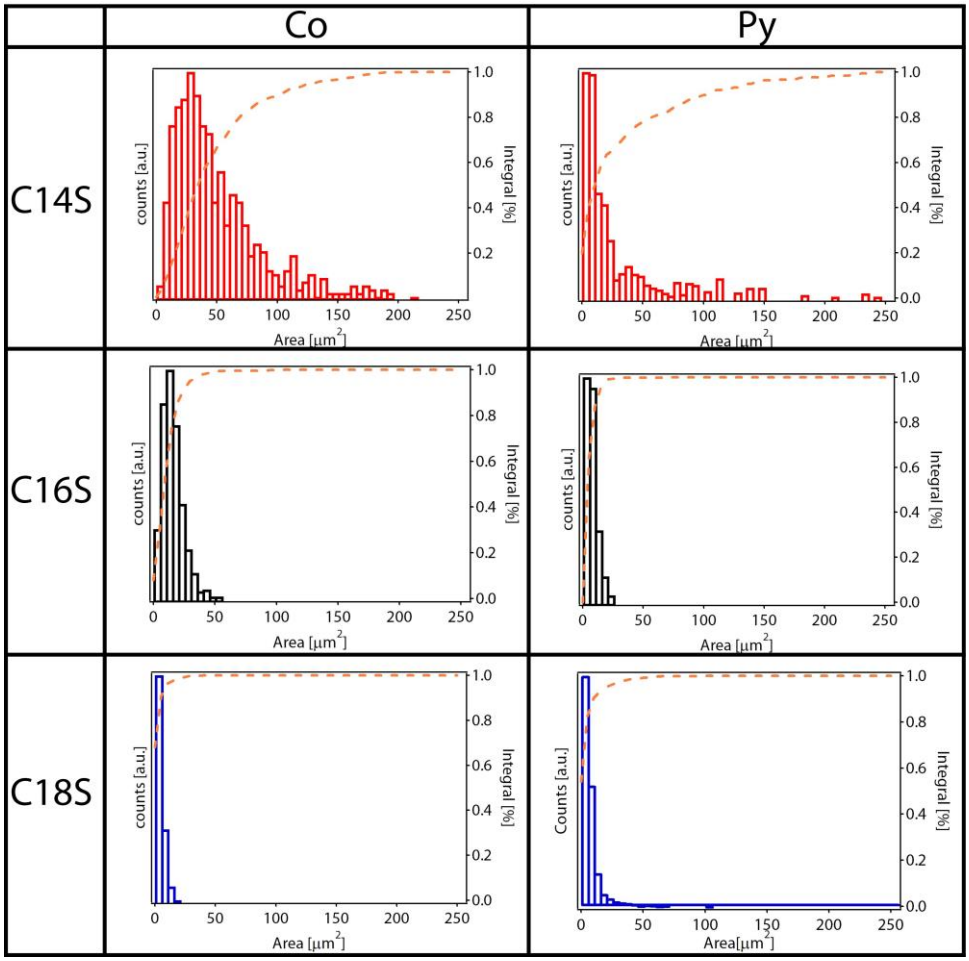

Figure 13 - Optical domain area histograms of Co and Py samples functionalized with C14s, C16S and C18S. Yellow dashed line is the area integral.

Values displayed below show that for Co and Py, shorter chain lengths give rise to bigger islands. However, less islands are detected on Py and tend to be smaller than those found on Co for all chain lengths. Moreover, and according to Table 2, longer alkyl chains render not only smaller but also thinner domains.

Table 4 – Statistical parameters from histograms in Figure 13 and total coverage derived from the optic statistic.

Material	Average Area [µm²]	Number of Island/100 µm²	P_{85} [µm²]	P_{50} [µm²]	Coverage [%]
Co-C14S	87.5	6.63	80	35	5.8
Co-C16S	22.5	33.8	20	10	7.6
Co-C18S	7.5	320	-	-	24
Py-C14S	67.5	2.07	70	10	1.4
Py-C16S	7.5	30.7	15	5	2.3
Py-C18S	9	62.2	-	-	5.6

From the analysed optical images, we also extracted the percentage of area covered by the islands. As can be observed in Table 4 moving from the C14S to the C18S, the cobalt coverage increases from approximately 6% to 24%. Moreover, the measured coverage in the case of Py was always below that measured for Co, and never exceeded 6%.

Using the average height derived from AFM (Table 2) and the coverage values displayed in Table 4, we can make a rough calculation of the material that has displaced from the original SAM into the island domains:

$$D = 2 * \frac{\bar{h}}{SH} * C$$

Where D is the percentage of displaced material, $\bar{h}$ is the average island height, SH is the calculated step height for each chain length and C is the coverage. We obtain that for Co, D values for C14S, C16S and C18S are 39.3%, 68.5% and 48%, respectively. The calculated value for C18S on cobalt is very close to the value of 45.6 % calculated from AFM data in Figure 10. For the case of Py, the values are 15.4%, 15.9% and 11.2%. These lower values reflect the lower tendency of Py to form island domains. In any case, what seems clear is that the space between islands is not completely void, and that there are still SAM molecules present on the surface.

4.2.3. Spectroscopy studies

Auger Spectroscopy. To gain chemical information and further confirm the structure proposed above we performed AES analysis on our samples in collaboration with the Autonomous University of Barcelona (UAB). Figure 14a-b shows a topographic AFM image of a C14S island of approximately 15 nm height. According to the model proposed above, this will correspond to at least 3 RS-M-SR layers. We recorded AES data inside (red square) and outside the island (green square) showed in Figure 14a. In Figure 14c-e the Auger spectra obtained from these two zones are shown at the cobalt, oxygen and sulphur edges. Outside the island strong oxygen and cobalt signals are recorded, while

only a faint signature of sulphur can be observed. This data is consistent with the migration towards the islands of surface bound thiols during the growing process, exposing the cobalt surface to oxidation. When the measurement was done on top of an island, we observed that the signals of cobalt and oxygen were attenuated while sulphur signal slightly increased. Escape depth of Auger electrons is only some nanometers, so the detector mostly collected electrons originated at the island volume while signals coming from the underlying cobalt surface are strongly attenuated. The main conclusion obtained from the AES measurements is that the islands contain cobalt besides the sulphur of the alkanethiol molecules. The presence of cobalt and sulfur inside the islands is consistent with the structure proposed in Figure 9. We tried to repeat the measurement in Py islands, to see if in the composition both nickel and iron were present. However, we did not observe any difference from the signal inside or outside the islands. This might indicate that the material was damaged by the measurement.

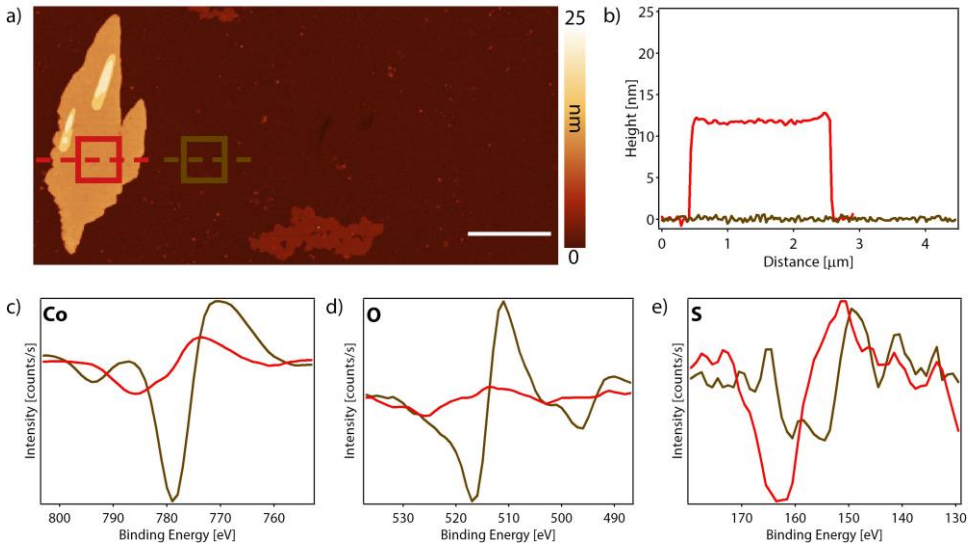

Figure 14 - Auger spectra determined inside (red) and outside (green) a C14S island grown over a 15 nm Co substrate, b) the height profile of the measured zone. Elemental spectra of c) Cobalt, d) Oxygen and e) Sulphur. The scale bar is of 2 µm.

Confocal Raman Spectroscopy. Strong adventitious carbon signals were observed inside and outside the islands, hindering carbon edge interpretation. Raman spectroscopy measurements were carried out to shine light on that, as alkyl chains show characteristic Raman peaks.

We compared the spectra recorded inside and outside the islands. Data recorded outside the island did not show any additional peaks compared to non-functionalized reference air-exposed cobalt samples. We have also run a series of measurements on gold surfaces functionalized with alkanethiols, but we did not observe any Raman signal, which suggest that our Raman is not sensitive enough to detect organic species at the monolayer level. Coming back to our samples, this does not mean that outside the islands the SAM is absent. From the data measured inside the island we observed a peak at 743 cm^{-1}

(Figure 15-i) that we tentatively assign to the twisting of the sulphur-carbon bond. [3,32,33] Additionally, in Figure 15-ii, are displayed signals coming from the C–H vibrations: C-H stretching (2849–2924 cm^{-1}), CH_2 scissoring (1450 cm^{-1}) and C–C aliphatic chain vibrations (1120–1290 cm^{-1}).[3,32,33] However, data measured inside the island showed no trace of unbound S-H groups at 2575 cm^{-1} (Figure 15-iii). [3,32,33] The intense silicon substrate signals, strong peaks at 1000 cm^{-1}, 532 cm^{-1} and 350 cm^{-1} mask any possible signal related to the S-M bonds which should be expected below 400 cm^{-1}.[3,32,33] These results seem to confirm the scenario were R-S molecules self-assembled on the cobalt surface, migrate and accumulate in the form of island domains when exposed to air.

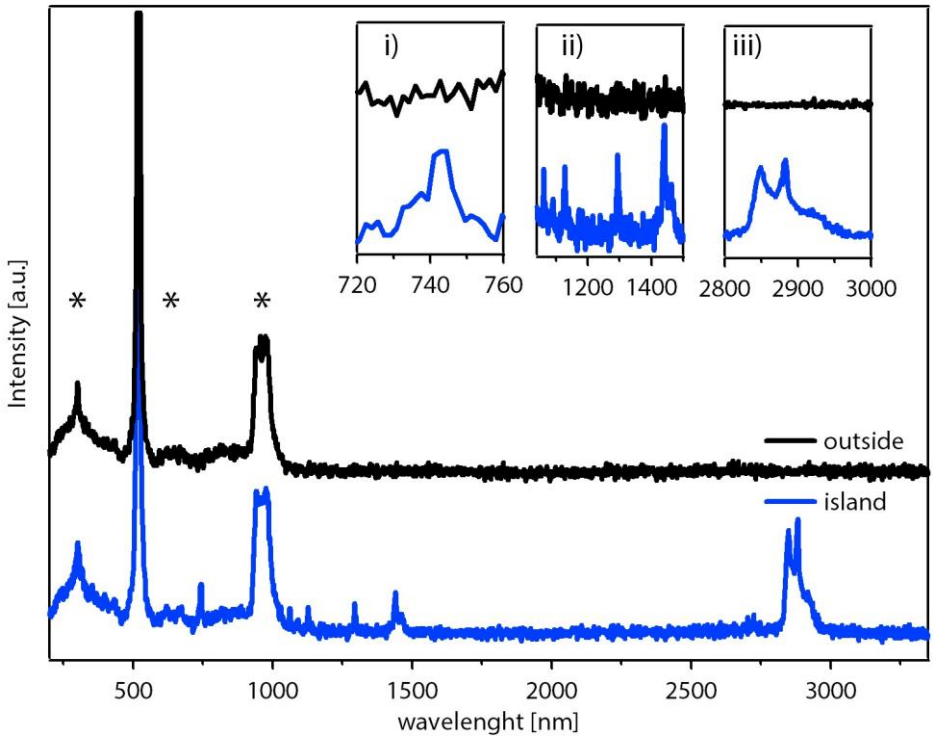

Figure 15 - Raman spectra recorded inside and outside an island, with its insets i), ii) and iii) of the regions of interest. Peaks marked with an * come from the silicon substrate.

The results presented above further confirm that the lamellar domains obtained after air exposure of Py and Co CnS–functionalized samples where n=14, 16, 18 are indeed formed by LMAs.

4.2.4.Growth rate studies

In the previous paragraphs we showed the topographic, structural and spectroscopy characterization of fully grown island domains. In this section, we will study the growth of the island domains as a function of time and also we will study the role of the temperature and atmosphere.

We proceeded to functionalize a Co surface with C18S inside a glove box, then we exposed the sample to air and we monitored the change of the topography as a function of time of a 30x30 μm^2 area using AFM. These results are presented in Figure 16.

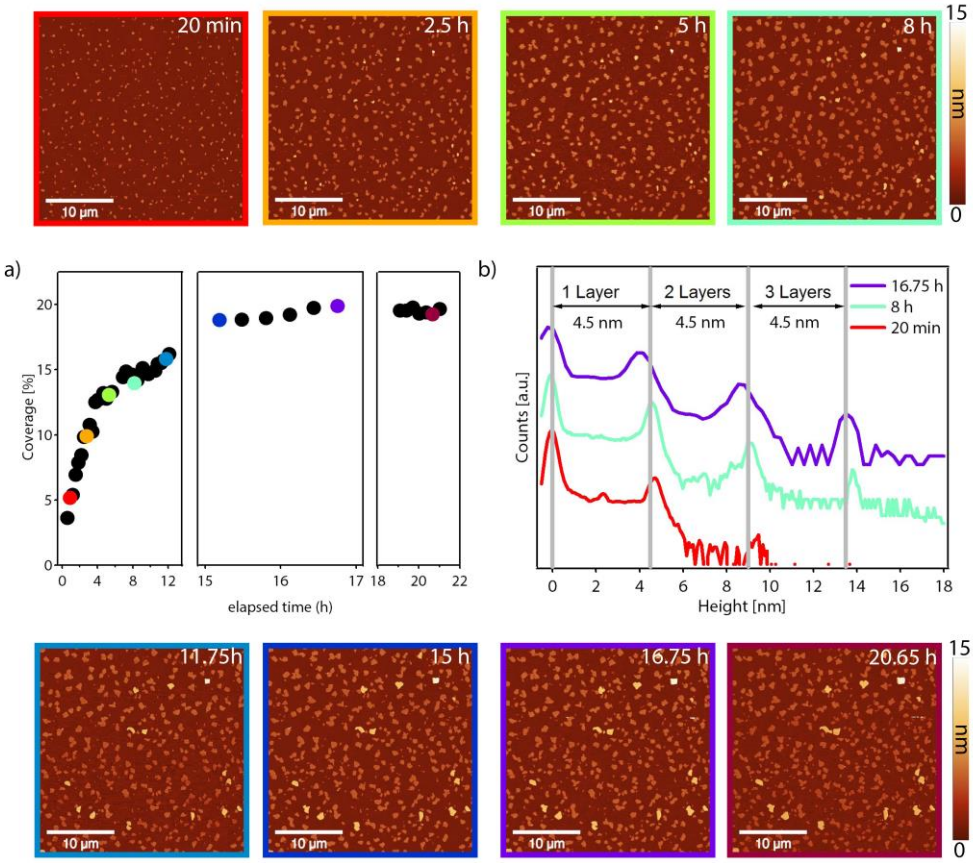

Figure 16 - Real time growth of C18S-Co island domains, imaged with AFM: AFM topographic images at 20 min (red), 2.5 h (orange), 5 h (yellow), 8 h (light green), 14.75 h (light blue), 15h (blue), 16.75 h (purple) and 20.65 h (deep red). (a) Evolution of the island coverage with time and (b) evolution of the height profile with time.

Figure 16a represents the coverage changes during the growing process. The AFM images with a coloured frame correspond to the points of the same colour in Figure 16a. It is possible to observe that right after air exposition the island domains started growing on the surface. The overall evolution of the height distribution is reported in Figure 16b. We observed that in the first 20 min (red) domains of around 4.5 nm height are present, while after 8 hours (green) some domains with a height slightly above 9 nm (2 layers) appear, and finally at the end of growing process, the height distribution reflects a small contribution of domains with 13.5 nm (3 layers). As commented before, in the case of C18S SAMs, interdigitation of the first layer is expected, which gives rise to a difference in the step height of the first and consecutive layers. Sample imaged in Figure 10 is not an exception of the above observation, but this effect is only detected at the later stages of the growing process. For instance, it is clearly visible after 17 hours (purple line) when no further evolution of number of islands, their areas or their heights is observed.

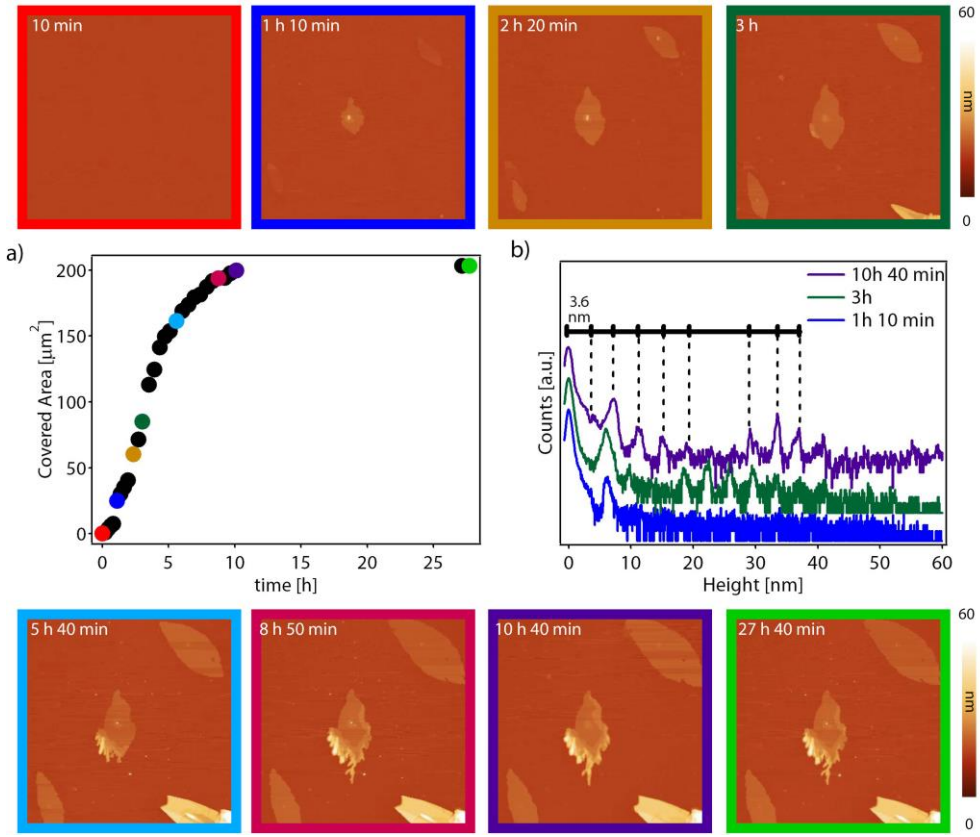

Figure 17 - Real time growth of C14S-Co island domains, imaged with AFM: AFM topographic images at 10 min (red), 1 h 10 min (blue), 2 h 20 min (orange), 3 h (dark green), 5 h 40 min (light blue), 8 h 50 min (pink), 10 h 40 min (purple) and 27 h 40 min (green). (a) Evolution of the island coverage with time and (b) evolution of the height profile with time. The colored squares indicate the corresponding point in the graph. The AFM images are 30x30 µm².

We have imaged a Co sample functionalized with C14S using AFM, like in the previous example. In this particular case, we observed a faster growth, because the whole process is accomplished in around 10 hours, as can be seen in Figure 17a. The height distribution, presented in Figure 17b, shows the presence of terraces of two layers (7 nm), since the very first images. After around 3h (in dark green), higher steps can be also observed.

Although some variability was observed between experiments, equivalent assays revealed that between 10 and 16 hours are necessary to reach stable island domains (no more variation in height or area are observed) independently of the substrate (Co or Py) and chain length used (n = 14, 16 or 18).

This is the first time that a kinetic measurement in real time is reported for this kind of island domains. We also want to remark that these island-like lamellar domains, grow exclusively on Co and Py, at room temperature, in a solvent free environment, which have never been reported in literature until the moment.

As we said before, AFM is a precise technique, but is time consuming and the quick imaging of the samples during the very first seconds of air contact is not possible. To improve the kinetic study, we took advantage of optical microscopy in order to take large area pictures in a matter of seconds. This allowed us to precisely follow the growing process in its initial stages. We functionalized again a cobalt sample with C14S, the sample was exposed to air and pictures were taken with the optical microscope every few minutes, as showed in Figure 18-21.

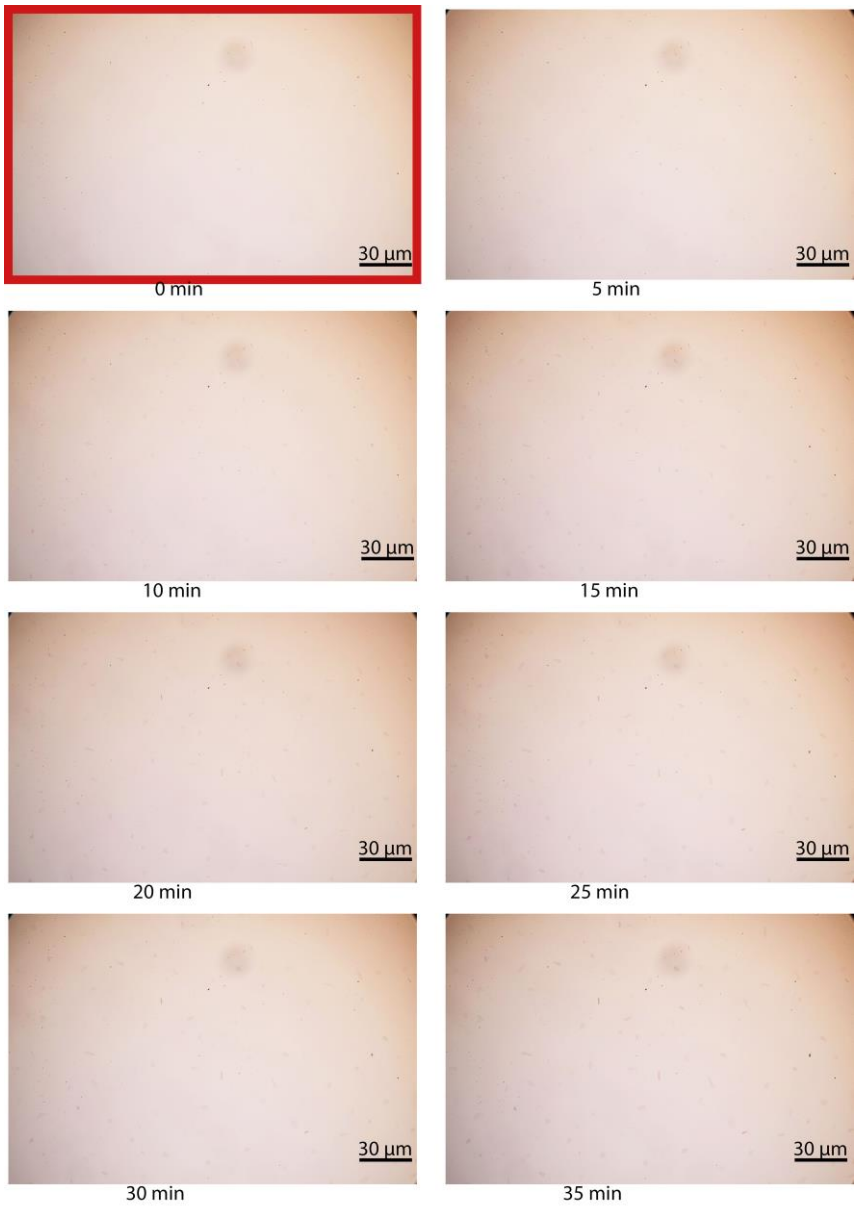

Figure 18 - Optical images of a kinetic on Co-C14S Surface from 0 to 35 minutes.

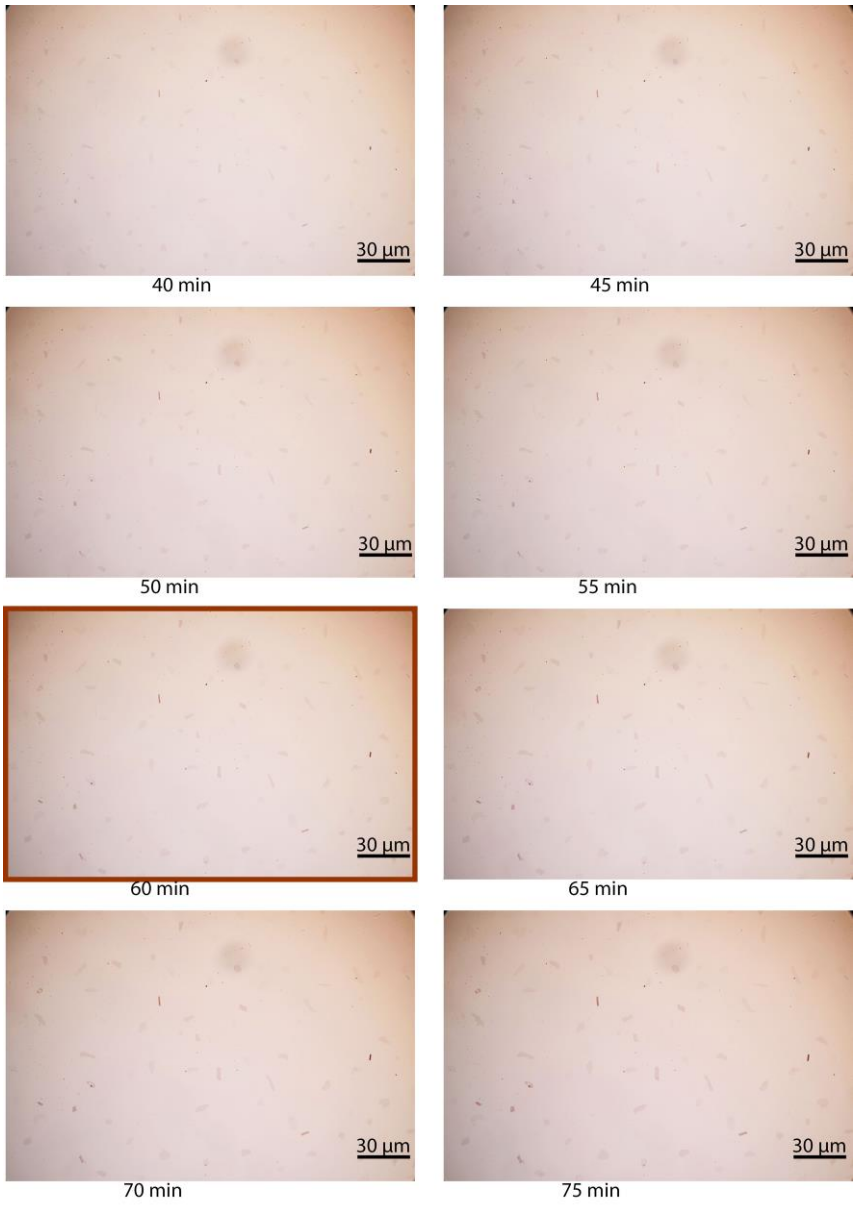

Figure 19 - Optical images of a kinetic on Co-C14S Surface from 40 to 75 minutes.

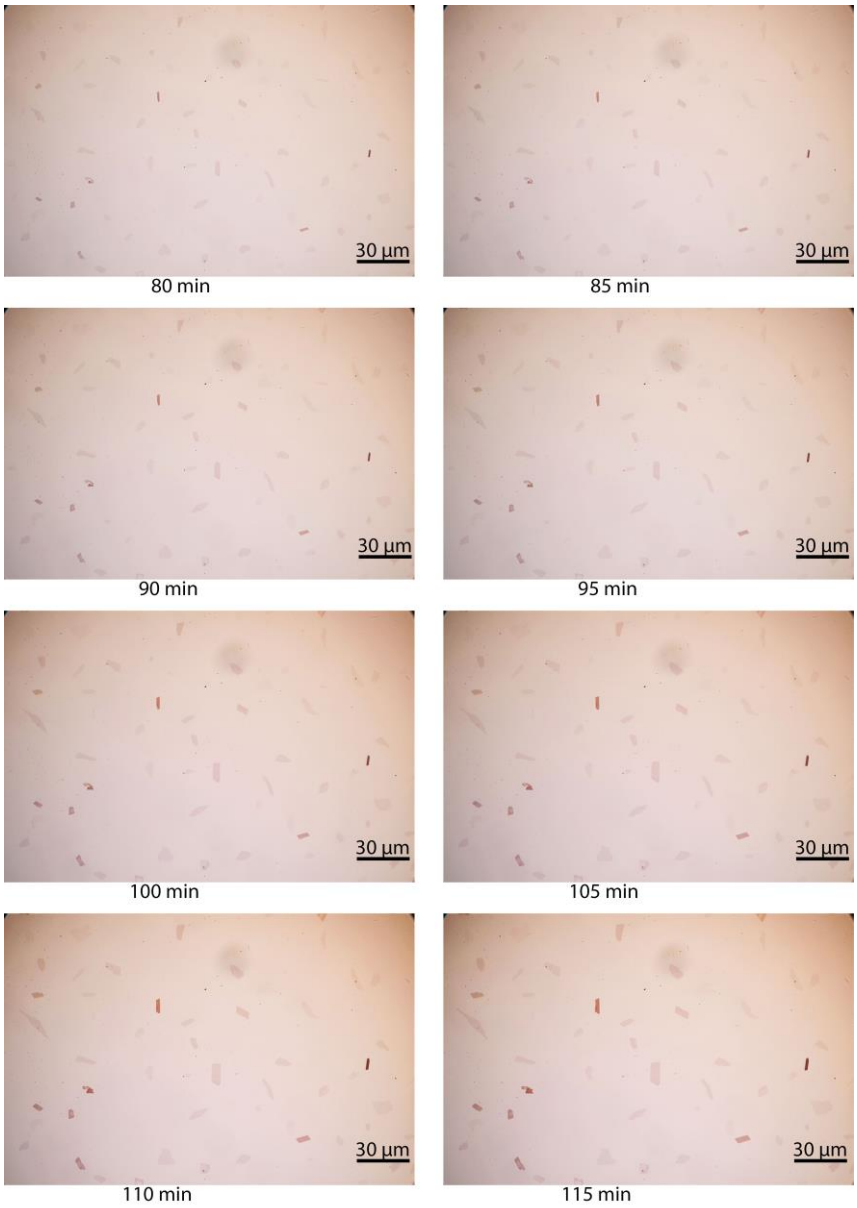

Figure 20 - Optical images of a kinetic on Co-C14S Surface from 80 to 115 minutes.

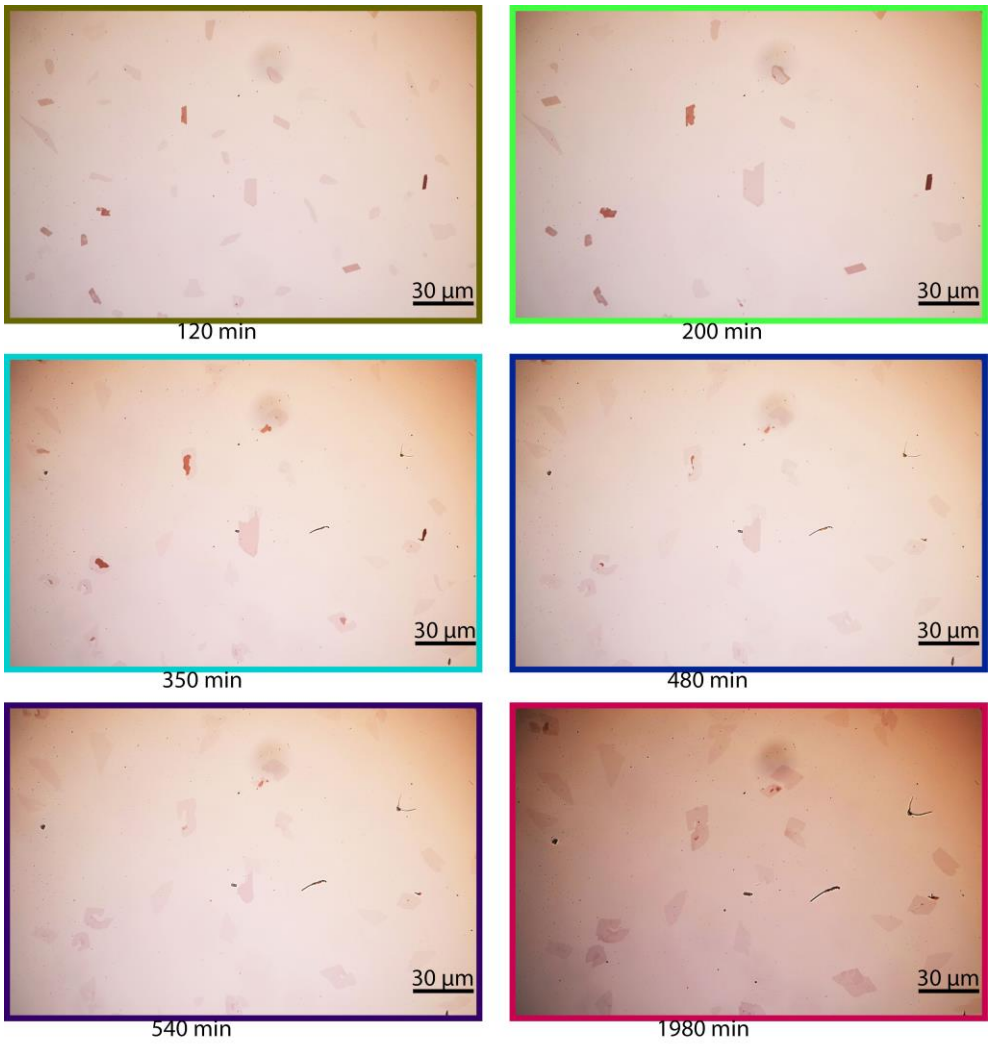

Figure 21 - Selected Optical images of a kinetic on Co-C14S from 120 to 1980 minutes (33 hours).

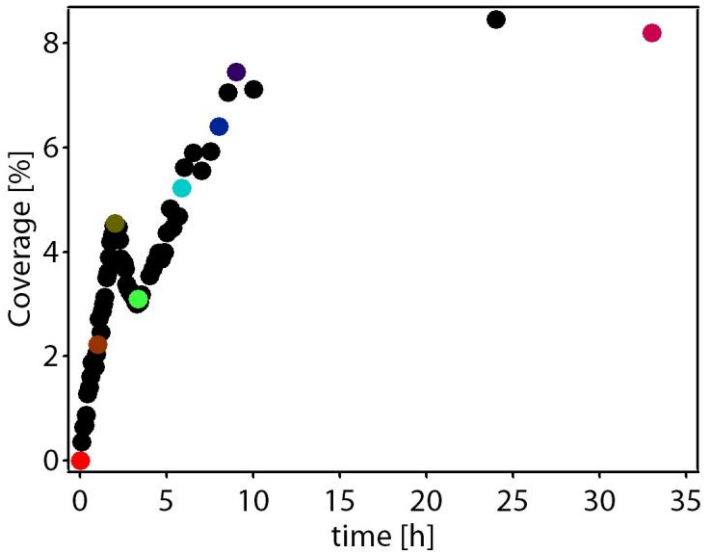

Figure 22 - Coverage evolution as a function of time of Co-C14S functionalized sample, calculated from images in Figure 18-21.

The coverage showed in Figure 22, exhibited the same trend of that measured with AFM and displayed in Figure 16a. Due to the shorter acquisition time of optical microscopy it is possible to observe that there is not only a lateral growth of the islands but also a reorganization of the material inside the growing domains. This is highlighted by the peak arising at 120 min in Figure 22.

4.2.5. Temperature and humidity influence studies

It is well known that the crystal growth in bulk materials is influenced by various parameters such as temperature, concentration or the growing media used.[34] The temperature, in particular, influences the balance between the nucleation and growth steps.[35] Based on that idea and to prove if the same behavior applies to our system, we performed a series of experiments where Co-C14S freshly functionalized samples were exposed to air at different

temperatures. We chose Co-C14S because, as discussed above, the resulting island domains are bigger and their optical detection is easier.

We functionalized three cobalt samples with C14S and we exposed them to air at three different temperatures: 35°, 25° (room temperature) and 5° and recorded optic images for all of them, as represented in Figure 23.

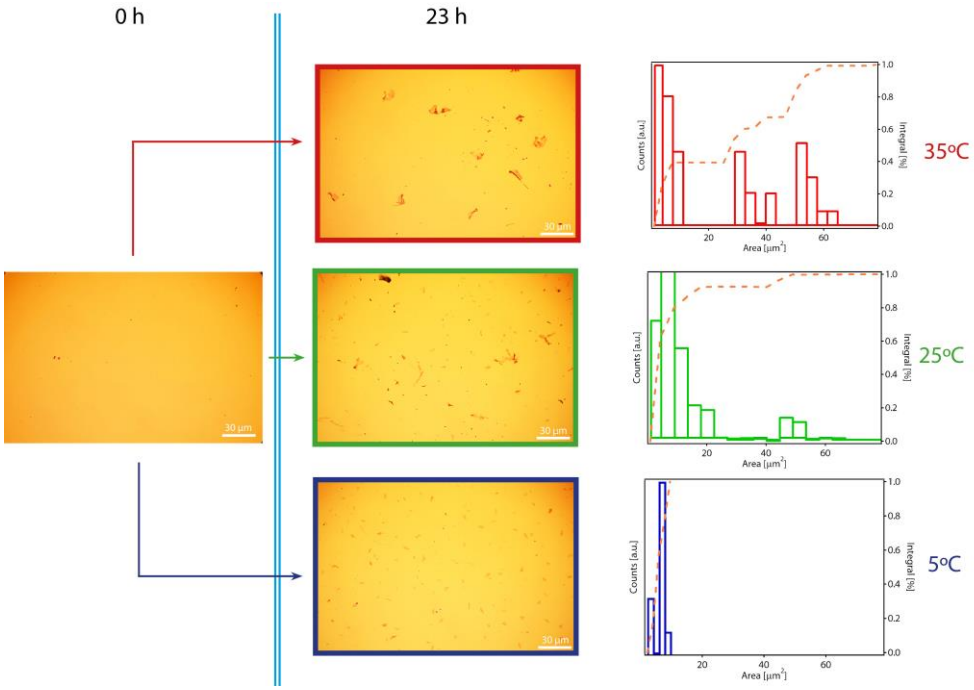

Figure 23 – Optical images of a Co-C14S samples exposed to the air at different temperatures for 23h, with their correspondent area distribution histograms and histogram area integrals (yellow dashed line).

At a first glance, it is possible to observe that after 23 h, the area distribution histograms show that an increase in temperature produces a smaller density of

islands, but with bigger sizes (Table 5). This result suggests that island domains grow following a nucleation and growth mechanisms similar to that observed for other bulk solids in solution.

Table 5 - Statistical parameters for histograms in Figure 23

Temperature [°]	Average Area [μm²]	Number of Islands/100 μm²	P_{85} [μm²]	P_{50} [μm²]
35	45	2.61	50	28
25	13	4.10	13	5
5	5	7.02	5	-

As we said before, one very important point is that, the LMAs growth take place only when the samples are exposed to air and not when they are kept under inert atmosphere. In ambient conditions, all surfaces are covered by a thin film of water, with dimensions that depend on the nature of the surface and the humidity and temperature conditions.[36–38] We wanted to study if this water layer was playing a key role in island domains formation. We designed an experiment where we functionalized a set of two twin cobalt samples with C14S. We exposed directly to air the first sample (Sample A), to have a reference, while we transferred the second sample directly from the glove box to a reaction chamber filled with dry air (Sample B). After 16 hours, we checked both samples using optical microscopy (Figure 24), and left both of them reacting in ambient conditions for additional 16 hours.

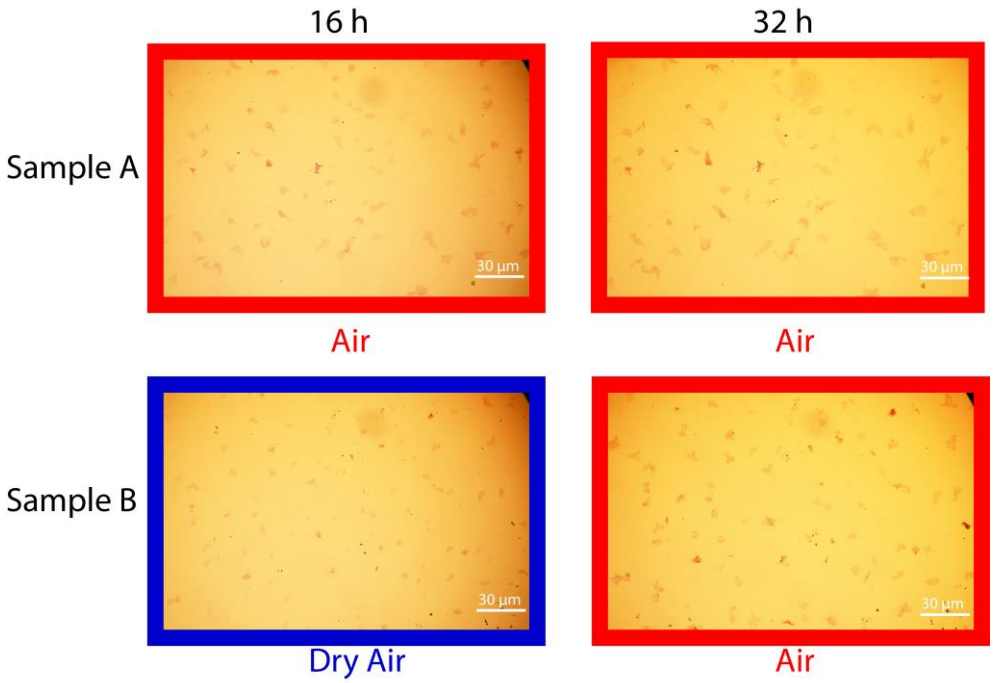

Figure 24 - Optical images of the substrates subjected to air and dry air for 16h and 32h.

Area histograms of optical images represented in Figure 24 are displayed in Figure 25.

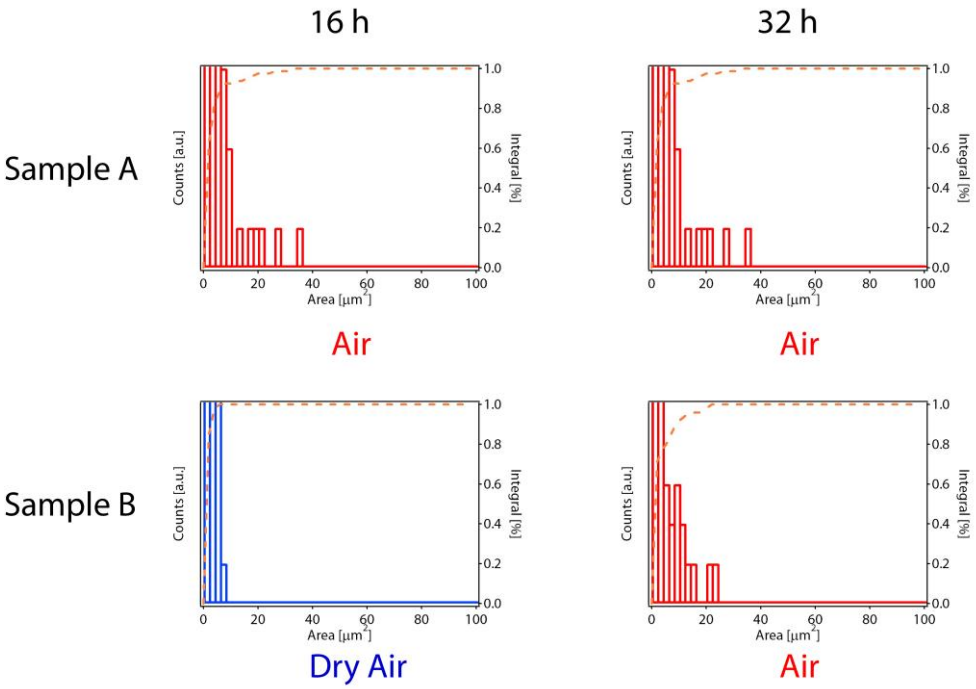

Figure 25 - Area distribution from the samples displayed in Figure 25 after 16h in air (or dry air) and additional 16 h in air. Yellow dashed line represents the histogram integrals.

In order to make straightforward the comprehension of the obtained results, in table 6 are reported the number of islands and the P_{85} for each of the atmospheres.

Table 6 - Statistical parameters from histograms in Figure 25.

Sample	Atmosphere	Time [h]	Average Area [μm^2]	Number of Islands/ 100 μm^2	P_{85} [μm^2]	P_{50} [μm^2]
A	Air	16	10	5.31	8	2
	Air	32	10	5.31	8	2
B	Dry Air	16	2	3.86	2	1
	Air	32	10	5.50	10	6

After 16h of reaction island growth on Sample A had already finished, and no particular evolution is observed after 32h. In the case of Sample B, we also observed the presence of islands after 16 hours of reaction under dry air. However, when we further exposed the sample to air for additional 16 hours, we found that both the number of island and their size increased to values closer to that reported for Sample A. In conclusion, it seems that, although water is not indispensable for island growth, it increases growth rate.

4.2.6. Etching Experiments

We took several topography AFM images on a single domain of Co-C18S in tapping mode, and we noticed that the material was etched away, from image to image, resulting in a modification of the island area. In the Figure 26l, it is possible to observe that when all the material is taken away from the tip, on the surface no hole is seen. This seems to confirm that island growth takes place over the original SAM.

Figure 26 – AFM topographic images of the Co-C18S island domains etching evolution depicted in a-l). The scale bar is 1 µm.

4.2.7. Growth mechanism

Based on all the information collected from the different techniques and from the growth experiments, we can propose a model to explain how do the island domains form. In Figure 27 our hypothesis is represented. In inert atmosphere,

we functionalize the FM surface, forming a complete alkanethiolate SAM. When the surface is exposed to air, oxygen reaches the cobalt surface through defects in the monolayer (Figure 27,i) triggering the oxidation of the metal from 0 to +2 and destabilizing the S-M bond. The continuity of the SAM is broken, which gives rise to the "jumping" of the metallic oxidized ions with the organic molecule away from the SAM giving rise to the appearance of the islands (Figure 27,ii).

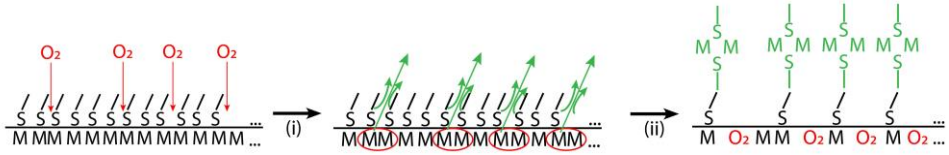

Figure 27 - Proposed growth mechanism of surface island domains. When the functionalized sample is exposed to air (i), oxygen enters into the defects oxidating the metal. The SAM is broken and reorganizes itself into island domains, the mass movement follows (ii) forcing the island domains growth.

4.3.Conclusions

The methodology studied in chapter 3 allowed the functionalization of FM surfaces with alkanethiolate SAMs in inert conditions. We observed that when these surfaces are exposed to air, lamellar domains started to appear spontaneously, without the use of any external stimulus and in a solvent free environment. The origin of their growth may be related to a not perfect protection against oxidation provided by the SAM. Surprisingly, this behavior has not been reported before in previous works that describe the preparation of SAMs on FM metals, even though the quality of the formed SAMs is equal in terms of contact angle, IR peaks value or stability against oxidation. Probably, several reasons can justify this fact: (1) there are only few works that face the formation of SAMs on FM metals, (2) imaging of the surface is usually not provided, (3) these domains only appear after air contact and (4) their growth seems to be restricted to alkanethiols chain lengths longer than 12 methylene.

Through this chapter, we have used several characterization techniques to shine light on the composition of these lamellar features. AFM and XRR confirmed that their step height is related to the alkanethiol used to functionalize the surface. Combining these results with additional Raman and AES spectroscopies, we have proposed an internal structure for the islands formed by stacks of CnS-M-SCn layers, where M is the metal present on the FM surface and CnS the thiol molecule. This structure is in resemblance to previously reported bulk Lamellar Metal-alkanethiolates and to other layered structures (LHDs and hexagonal TMDCs).

Our statistical analysis of AFM and Optical microscopy images pointed out that the number, area and height of the islands are inversely proportional to the length of the alkylic chain that composes the SAM. Moreover, in all cases not all the thiol molecules migrate into the lamellae; part of them remain on the surface as a SAM, which means that there is not bare surface between the islands.

The study of the kinetics of the growing process has also been faced during this chapter. These studies have confirmed that islands only start to appear when the sample gets in contact with air, and that their evolution takes generally 10-16 hours, after this time, no further changes are detected. It is also important to remark that temperature strongly influences the process. An increase of the temperature speeded up the assembly of the molecules, but the quality of the obtained material was far below the room temperature one. We also observed that the humidity of the environment does not play a critical role in the growth of these lamellar features.

One remarkable feature emerged during the research, is that the islands growth takes place in ambient conditions, at room temperature, in a solvent free environment and without the use of any external stimulus.

4.4. References

1. Hart, R. K. & Maurin, J. K. The nucleation and growth of oxide islands on aluminum. *Surf. Sci.* **20,** 285–303 (1970).

2. Luo, L., Kang, Y., Yang, J. C. & Zhou, G. Nucleation and growth of oxide islands during the initial-stage oxidation of (100)Cu-Pt alloys. *J. Appl. Phys.* **117,** 65305 (2015).

3. Fijolek, H. G., Grohal, J. R., Sample, J. L. & Natan, M. J. A Facile Trans to Gauche Conversion in Layered Silver Butanethiolate. *Inorg. Chem.* **36,** 622–628 (1997).

4. Bensebaa, F., Ellis, T. H., Kruus, E., Voicu, R. & Zhou, Y. The self-assembly of a layered material: metal-alkanethiolate bilayers. *Can. J. Chem.* **76,** 1654–1659 (1998).

5. Bensebaa, F., Ellis, T. H., Kruus, E., Voicu, R. & Zhou, Y. Characterization of Self-Assembled Bilayers: Silver–Alkanethiolates. *Langmuir* **14,** 6579–6587 (1998).

6. Levchenko, A. A., Yee, C. K., Parikh, A. N. & Navrotsky, A. Energetics of Self-Assembly and Chain Confinement in Silver Alkanethiolates: Enthalpy–Entropy Interplay. *Chem. Mater.* **17,** 5428–5438 (2005).

7. Dance, I. G., Fisher, K. J., Banda, R. M. H. & Scudder, M. L. Layered structure of crystalline compounds silver thiolates (AgSR). *Inorg. Chem.* **30,** 183–187 (1991).

8. Ye, Z., de la Rama, L. P., Efremov, M. Y., Zuo, J.-M. & Allen, L. H. Approaching the size limit of organometallic layers: synthesis and characterization of highly ordered silver–thiolate lamellae with ultra-short chain lengths. *Dalt. Trans.* **45,** 18954–18966 (2016).

9. Parikh, A. N. *et al.* Characterization of Chain Molecular Assemblies in Long-Chain, Layered Silver Thiolates: A Joint Infrared Spectroscopy and X-ray Diffraction Study. *J. Phys. Chem. B* **103,** 2850–2861 (1999).

10. John, N. S., Thomas, P. J. & Kulkarni, G. U. Self-Assembled Hybrid Bilayers of Palladium Alkanethiolates. *J. Phys. Chem. B* **107,** 11376–11381 (2003).

11. John, N. S., Pati, S. K. & Kulkarni, G. U. Electrical characteristics of layered palladium alkanethiolates by conducting atomic force microscopy. *Appl. Phys. Lett.* **92,** 13120 (2008).

12. Busupalli, B., Kummara, S., Kumaraswamy, G. & Prasad, B. L. V. Ultrathin Sheets of Metal or Metal Sulfide from Molecularly Thin Sheets of Metal Thiolates in Solution. *Chem. Mater.* **26,** 3436–3442 (2014).

13. Yang, Z., Smetana, A. B., Sorensen, C. M. & Klabunde, K. J. Synthesis and Characterization of a New Tiara Pd(II) Thiolate Complex, [Pd(SC12H25)2]6 , and Its Solution-Phase Thermolysis to Prepare Nearly Monodisperse Palladium Sulfide Nanoparticles. *Inorg. Chem.* **46,** 2427–2431 (2007).

14. Thomas, P. J., Lavanya, A., Sabareesh, V. & Kulkarni, G. U. Self-

assembling bilayers of palladiumthiolates in organic media. *J. Chem. Sci.* **113,** 611–619 (2001).

15. Woodward, P., Dahl, L. F., Abel, E. W. & Crosse, B. C. A New Type of Cyclic Transition Metal Complex, [Ni(SC 2 H 5) 2] 6. *J. Am. Chem. Soc.* **87,** 5251–5253 (1965).

16. John, N. S. *et al.* Magnetic Interactions in Layered Nickel Alkanethiolates. *J. Phys. Chem. C* **111,** 1868–1870 (2007).

17. Calderon, M. F. *et al.* New Findings for the Composition and Structure of Ni Nanoparticles Protected with Organomercaptan Molecules. *Langmuir* **29,** 4670–4678 (2013).

18. Cha, S.-H., Kim, J.-U., Kim, K.-H. & Lee, J.-C. Preparation and Photoluminescent Properties of Gold(I)–Alkanethiolate Complexes Having Highly Ordered Supramolecular Structures. *Chem. Mater.* **19,** 6297–6303 (2007).

19. Cha, S.-H., Kim, K.-H., Kim, J.-U., Lee, W.-K. & Lee, J.-C. Thermal Behavior of Gold(I)–Thiolate Complexes and Their Transformation into Gold Nanoparticles under Heat Treatment Process. *J. Phys. Chem. C* **112,** 13862–13868 (2008).

20. Nie, H., Li, M., Hao, Y., Wang, X. & Zhang, S. X.-A. Time-resolved monitoring of dynamic self-assembly of Au(i)-thiolate coordination polymers. *Chem. Sci.* **4,** 1852 (2013).

21. Woodward, J. T. *et al.* Effect of an Oxidized Gold Substrate on

Alkanethiol Self-Assembly. *Langmuir* **16,** 5347–5353 (2000).

22. Sandhyarani, N. & Pradeep, T. An investigation of the structure and properties of layered copper thiolates. *J. Mater. Chem.* **11,** 1294–1299 (2001).

23. Keller, H., Simak, P., Schrepp, W. & Dembowski, J. Surface chemistry of thiols on copper: an efficient way of producing multilayers. *Thin Solid Films* **244,** 799–805 (1994).

24. Park, S.-H. & Lee, C. E. A series of long-chain lamellar hydrated copper(II) alkylsulfonates with different chain molecular assemblies. *Chem. Commun.* **1,** 1838–1839 (2003).

25. Park, S. H. & Lee, C. E. Characterization of chain molecular assemblies in long-chain, lamellar copper alkylsulfonates: Self-assembled monolayer vs bilayer structure. *Chem. Mater.* **18,** 981–987 (2006).

26. Hu, L. *et al.* Self-Assembly and Ripening of Polymeric Silver–Alkanethiolate Crystals on Inert Surfaces. *Langmuir* **25,** 9585–9595 (2009).

27. Hu, L. *et al.* Synthesis and Characterization of Single-Layer Silver–Decanethiolate Lamellar Crystals. *J. Am. Chem. Soc.* **133,** 4367–4376 (2011).

28. Bragg, W. H. & Bragg, W. L. The Reflection of X-rays by Crystals. *Proc. R. Soc. A Math. Phys. Eng. Sci.* **88,** 428–438 (1913).

29. Sellers, H., Ulman, A., Shnidman, Y. & Eilerss, J. E. Structure and Binding of Alkanethiolates on Gold and Silver Surfaces: Implications for Self-Assembled Monolayers. *J. Am. Chem. SOC* **115,** 9389–9401 (1993).

30. Nečas, D. & Klapetek, P. Gwyddion: an open-source software for SPM data analysis. *Open Phys.* **10,** 181–188 (2012).

31. Bensebaa, F. *et al.* Raman characterization of metal-alkanethiolates. *Spectrochim. Acta Part A Mol. Biomol. Spectrosc.* **55,** 1229–1236 (1999).

32. Bryant, M. A. & Pemberton, J. E. Surface Raman scattering of self-assembled monolayers formed from 1-alkanethiols: behavior of films at gold and comparison to films at silver. *J. Am. Chem. Soc.* **113,** 8284–8293 (1991).

33. Burton, W. K. & Cabrera, N. Crystal growth and surface structure. Part I. *Discuss. Faraday Soc.* **5,** 33 (1949).

34. Cabrera, N. & Burton, W. K. Crystal growth and surface structure. Part II. *Discuss. Faraday Soc.* **5,** 40 (1949).

35. Santos, S. & Verdaguer, A. Imaging Water Thin Films in Ambient Conditions Using Atomic Force Microscopy. *Materials (Basel).* **9,** 182 (2016).

36. Henderson, M. A. The interaction of water with solid surfaces: fundamental aspects revisited. *Surf. Sci. Rep.* **46,** 1–308 (2002).

37. Verdaguer, A., Sacha, G. M., Bluhm, H. & Salmeron, M. Molecular

structure of water at interfaces: Wetting at the nanometer scale. *Chem. Rev.* **106,** 1478–1510 (2006).

Conclusions and Outlook

After our exhaustive study about the molecular functionalization of ferromagnetic metals, several aspects can be highlighted as main conclusions of this work that will drive the perspectives of our future working plan:

1- The passivating oxide layer that naturally grows on FM metals in ambient conditions can be used as adhesion layer for the growth of high quality SAMs. The key point of the SAM formation is the use of an optimum treatment of the surface just before molecular functionalization takes place. It was observed that the application of soft H_2 plasma, as preliminary surface cleaning/activation step, drastically improves the quality of the formed SAMs. This fact can be justified due to the increase of hydroxy groups on the surface that makes easier the condensation reaction with the surfactant possible. Phosphonic acids are perfect anchoring group in order to obtain high quality SAMs as continuous layers all over the surface. It is important to highlight that none of the steps needed to form the SAMs affect the nature and magnetic properties of the underlying FM metal. The quality of the formed SAMs permits their nanostructuration on the surface into defined patterns by means of soft lithography techniques. These patterns can be used as an effective etch resistant layer with potential application in circuitry design of FM metals, or can be envisaged as a seed layer for the deposition of different molecular

structures like surface MOFs. These applications have been already preliminary proven and can be extensively studied in a next future.

2- Glycolic acid can be used as a selective etching agent to completely remove the passivating oxide layer in FM metals without damaging the surface. The oxide-free recovered FM surface can be then functionalized with alkanethiols giving rise to homogeneous SAMs that maintain their integrity as long as they are kept under inert atmosphere. The perfect removal of the antiferromagnetic oxide layer, the low roughness of the resulting surface and the effective growth of high quality SAMs permit using this methodology to build molecular based tunnel junctions which show magnetoresistance at room temperature (work in collaboration with CNRS/Thales). These results motivate us to work on the implementation of this methodology to the formation of more complex SAMs over bare FMs, such as organic radical bearing SAMs, that could be of special interest as interfaces on spintronic devices.

3- Alkanethiol SAM modified FM metals, when exposed to air, quickly oxidize. In the case of alkyl chains with more than 12 carbon atoms this gives rise to the spontaneous formation of lamellar island like features all over the surface. The step height, area and number of these features are strongly dependent on the length of the alkyl chain used, which supports a molecular nature of these islands, that is further corroborated by Raman spectroscopy and X-Ray diffraction. The presence of the metal atoms inside the islands that can come exclusively from the FM surface is backed up by Auger spectroscopy. These data led us to the conclusion that the lamellar features are composed of a central metal-sulfur backbone sandwiched between two alkylic chains, in

analogy to bulk Lamellar Metal-alkanethiolate and to other layered structures (LHDs and hexagonal TMDCs), previously described in literature. Most remarkably, in our case growth on a surface takes place in situ, in a solvent free environment, and can be imaged precisely in way that had been never reported before. Regarding these results there are some questions that remain unexplained and have to be further investigated, like the mechanism that is really involved in the formation of the islands, how the coordination of the metallic ions takes place, or if it is possible to avoid the formation of the islands by means of the preparation of interlinked SAMs that could prevent the oxidation of the surface. Moreover, we also want to assess if the use of freshly prepared FM metals instead of recovered surfaces plays a decisive role in the appearance and growth of the islands.

Experimental Methods

I. Reagents

1-Dodecylphosphonic acid (Fluka, 95%) (C12P), 1-tetradecylphosphonic acid (Sigma-Aldrich, 97%) (C14P), 1-hexadecylphosphonic acid (Sigma-Aldrich, 97%) (C16P), and 1-octadecylphosphonic acid (Sikemia, 97%) (C18P) are commercially available and were used without any further purification. 2-Propanol (HPLC grade) and diethylene glycol were bought from Sigma-Aldrich. Kit Silicon Elastomer Sylgard 184 from Down Corning GMBH was used to prepare polydimethylsiloxane (PDMS) stamps.

1-decanethiol (Sigma-Aldrich, 97%) (C10S), 1-dodecanethiol (Sigma-Aldrich, 97%) (C12S), 1-tetradecanethiol (Sigma-Aldrich, 97%) (C14S), and 1-octadecanethiol (Sigma-Aldrich, 97%) (C18S) are commercially available and were used without any further purification. Absolute Ethanol (HPLC grade) and molecular sieves, 5 Å were bought from Sigma-Aldrich.

II. Substrate Preparation

Py layers were deposited on silicon or glass substrates using a tungsten basket coated Edwars Auto 500 thermal evaporator placed inside a nitrogen glovebox.

Base pressure was 2×10^{-6} mbar and evaporation rate 0.02 nm/s. 15 nm was the preferred thickness except for infrared spectroscopy, X-ray photoelectron spectroscopy and magnetic characterization, where approximately 150, 40 and 4 nm were used, respectively. When it was required, and to avoid Py oxidation, the Py samples were capped with an additional 25 nm gold layer.

Before Py evaporation, silicon substrates were sonicated 3 × 10 min in freshly prepared $H_2O_2/NH_4OH/H_2O$ (1:1:2) solutions, rinsed with milli-Q water, sonicated for 5 min in milli-Q water twice, and dried under a N_2 stream. Glass substrates were cleaned with an aqueous soap solution before use.

The cobalt layers were deposited using a Plassys MP9000 sputtering system, under Ar pressure of 2.5×10^{-6} mbar. The deposition rate is around 0.9 Angstrom/ s.

III. General procedure for SAM Formation

III.1. Alkylphosphonic Acid Monolayer Formation

Before chemical functionalization, in some cases, the substrates were pretreated in a plasma cleaner (MiniPCFlecto, Plasma Technology) under the following conditions, referred thorough the text as: (1) hydrogen plasma (H_2 0.03 mbar, 24 W, 30 sccm, 2 min) and (2) oxygen plasma (O_2 0.03 mbar, 32 W, 30 sccm, 2 min). For XPS, in order to increase the plasma effect, stronger plasma conditions were applied (80 W).

After the pretreatment, the substrates were dipped during a period of time ranging from some seconds to 16 h in a filtered 2 mM isopropanolic solution of

an APA of the desired chain length. After this time, the substrates were rinsed with fresh 2-propanol, dried under a N_2 stream and heated at 60° on a hot plate during 5 min.

Different sets of reference samples were also prepared following exactly the same experimental procedure but using neat 2-propanol instead of APA solutions.

III.2. Alkanethiol Monolayer Formation

Mixing methodology. A glycolic acid solution (GA) (10% in weight in 10 mL) was prepared inside the glove box, using anhydrous absolute ethanol, previously dried using molecular sieves. An alkanethiol 1 mM ethanolic solution of 10 mL (CnS) was prepared inside the glove box, using anhydrous absolute ethanol.

The substrates were transferred into the glove box, dipped into the 2 mL of the filtered GA solution for 15 min, then 2 mL of the filtered CnS solution was added. After 16 hours the substrates were rinsed with fresh anhydrous absolute ethanol, and were dried under a N_2 stream.

Different sets of reference samples were also prepared following exactly the same experimental procedure but dipping only into the GA solution for the same time as the CnS samples.

IV. Characterization Techniques

IV.1. X-ray Photoelectron Spectroscopy (XPS)

X-ray photoelectron spectroscopy (K-ALPHA, Thermo Scientific) was used to analyze the surfaces of the samples. Samples were analyzed *ex situ* at the X-ray Spectroscopy Service at the Universidad de Alicante. All spectra were collected using Al Kα radiation (1486.6 eV), monochromatized by a twin crystal monochromator, yielding a focused X-ray spot (elliptical in shape with a major axis length of 400 μm) at 3 mA·C and 12 kV. The alpha hemispherical analyzer was operated in the constant energy mode with survey scan pass energies of 200 eV to measure the whole energy band and 50 eV in a narrow scan to selectively measure the particular elements. XPS data were analyzed with Avantage software. A smart background function was used to approximate the experimental backgrounds. Charge compensation was achieved with the system flood gun that provides low energy electrons and low energy argon ions from a single source. Spectra are referenced using the C 1s main peak (284.8 eV).

IV.2. Contact Angle (CA) measurements

Dynamic water contact angle measurements of the samples were performed in air using a Ramé-hart 200 standard goniometer equipped with an automated dispensing system. The initial drop volume was 0.17 μL, increased by additions of 0.08 μL and waiting times of 1500 ms for each step.

IV.3. Atomic Force Microscopy (AFM)

The substrates were imaged with a Digital Instruments Veeco Nanoscope IVa AFM microscope in tapping and contact mode. Silicon tips with natural resonance frequency of 300 kHz and with an equivalent constant force of 40 N/m were used.

IV.4. Scanning Electron Microscopy (SEM)

S-4800 (HITACHI) Scanning electronic microscope with a spotlight of field emission (FEG) and a resolution of 1.4nm at 1KV was used. This equipment has backscattered detector of RX Bruker, transmission detector, the QUANTAX 400 programme for microanalysis and the five motorized axes

IV.5. Optical Microscopy

Optical images were obtained with a NIKON Eclipse LV-100 Optical microscope, equipped with Neutral Density Filters (ND50).

IV.6. Matrix-Assisted Laser Desorption Ionization- Time of Flight Mass Spectrometry (MALDI-TOF MS)

Samples were prepared as follows: 1 µL of CHCA matrix (5 mg/mL CHCA (Bruker) in 0.1% TFA-ACN/H_2O (7:3, v/v)) was directly spotted onto the substrates to analyze and allowed to dry in air at room temperature.

The samples were analyzed in a 5800 MALDI TOF instrument (ABSciex) in positive reflectron mode (3000 shots every position) in a mass range of 150–3000 *m*/*z*. Previously, the plate and the acquisition method were calibrated

with a CalMix solution. The analysis was carried out at the Proteomics Unit in the SCIE of the Universitat de València.

IV.7. Infrared Reflection- Absorption Spectroscopy (IRRAS)

A VeeMax II sampling stage (Pike Technologies) was placed in the sample compartment of a NICOLET 5700 transformation-infrared spectrometer. All measurements were performed under Ar atmosphere. Each FTIR spectrum represents the average of 512 scans with 4 cm^{-1} resolution. The infrared beam (incidence angle: 75°) was p-polarized by means of a manual ZnSe polarizer, and the output signal was collected with a refrigerated mercury cadmium telluride detector.

IV.8. X-Ray Reflectivity (XRR)

XRR spectra were recorded on PANalytical Empyrean X-ray difractometer equipped with a hybrid monochromator (Cu–Kα = 1.5418 Å), a focusing mirror and a PIXcel detector. Data was modeled using PANalytical's X'pert reflectivity software with a three slab model (SAM/Oxide/Substrate) in where the monolayers electron density was kept constant throughout all the film.

XRR spectra were recorded at the I07 Beamline at the Diamond Light Source, Didcot, U.K. using as wavelength 0.9918 Å , with 12.5 keV voltage.

IV.9. Magneto-Optical Kerr Effect Magnetometry (MOKE)

Measurements have been performed at room and low temperature (15–27 K), by means of a homemade Kerr Magnetometer equipped with longitudinal setup using a green laser (560 nm) as excitation light, applying a magnetic field of 325 mT and with an analyzer set at 0°.

IV.10. Auger Spectroscopy (AES)

Auger electron spectroscopy experiments were performed in a PHI 670 Scanning Auger Nanoprobe (from Physical Electronics) with a Schottky field emission electron gun as excitation source, Cylindrical Mirror Analyser (CMA) and Multichannel Detector system. In order to avoid inhomogeneity the analyzed area was about 2 microns around the center of reference. Electrons of 10 keV of energy were sent perpendicularly to the surface of the sample and a Fix Retard Ratio mode was used to collect the electrons with an energy step of 1 eV for all the range. MULTIPAK software has been used to obtain the derivative spectra.

IV.11. Raman Spectroscopy

Raman spectra were acquired with a micro-Raman (model XploRA ONE from Horiba, Kyoto, Japan) with a power of 4.5 mW, wavelength 532 nm, grating of 1800 gr/mm, slit of 50 μm, and hole of 100 μm.

IV.12. X-ray Absorption Spectroscopy (XAS) and X-Ray Magnetic Dichroism (XMCD).

The experiments have been performed at the CIRCE beamline of the Alba Synchrotron Light Facility. The beamline employs an Elmitec spectroscopic and low-energy electron microscope (SPELEEM), which allows real-time LEEM imaging, as well as selected-area microspot LEED. The instrument also allows acquiring the x-ray absorption spectrum at the different elemental edges, as a function of the photon energy with both photon helicities. By combining the XAS spectrum recorded with the two photon helicities is possible to calculate the X-ray circular magnetic dichroism (XMCD). The main microscope chamber operates with a base pressure below 1.10^{-10} mbar, at room temperature.

V. Microcontact Printing and Etching

A total of 10 mg of C18P were sonicated for 1 h in 10 mL of diethylene glycol. A PDMS stamp (prepared using a compact disc as mold) of approximately 100 mm^2 was covered for 45 s with a drop of the filtered APA solution, the excess solution was blown with a N_2 stream, and then the stamp was placed in close contact with a hydrogen plasma activated Py surface with the help of two magnets. After applying pressure for 15 s, the stamp was carefully peeled off. Finally, the patterned Py was immersed in a glycolic acid isopropanol solution (10% in weight) for at least 4 h to completely etch away the nonpatterned Py areas. Then, the samples were removed from solution, rinsed with isopropanol and dry with a N_2 flow. Py stripes were easily observed by optical microscopy and AFM.

VI. Inverted Lithography

A Poly(methyl_methacrylate) (PMMA) solution (5g in 20g acetone) was deposited on a silicon surface, later it was put in contact with the PDMS stamp to create the line pattern. 5 nm of Cobalt were deposited, we chose this height to make easier the lift off of the PMMA. The lift off was performed by submerging the substrate in a acetone solution for 9 hours.

A Appendix

A.1 Atomic Force Microscopy (AFM)

The atomic force microscope (AFM) was designed and invented by Binning, Quate and Gerber in 1986,[1] and allowed performing measurements on insulating samples and also liquids, to overcome the limitations of its predecessor, the scanning tunnel microscope, which only could measure conducting or semiconducting samples. AFM measurements can be carried out in atmosphere and also in UHV.

The basic principle of the AFM is the measurement of the interactive force between a tip and the sample. The tip is mounted on a cantilever which moves across the sample in raster mode and the tip-sample interaction is recorded by measuring the cantilever deflection, using a laser which illuminates the back of the tip and is reflected to a 4 quadrant split photodetector, to monitor the movement in x and y axis. The AFM cantilevers are microfabricated from silicon or silicon nitride using photolithographic techniques. Their typical dimensions are on the order of 100 μm with thickness of 1 μm. The experimental setup is completed with a set of piezoelectric tube scanners, that assure the micrometric positioning, and with an electronic control system which is based on digital feedback.

The AFM can be used either in the static or the dynamic mode. In the **static mode**, also referred to as the repulsive or contact mode, a sharp tip at the end of the cantilever is brought into contact with the surface of the sample. The force acting on the tip causes the cantilever to deflect, which is usually measured by optical detectors. This interaction force between tip and sample is measured by monitoring the cantilever deflection.

In the **dynamic mode** of operation, also referred to as attractive force imaging or noncontact imaging mode, the tip is brought into close proximity to (typical few nanometers), but not in contact with the sample. The most used working mode in AFM is the so-called *tapping* mode (intermittent contact mode). In the tapping mode, during the surface scan, the cantilever/tip assembly is sinusoidally vibrated by a piezo mounted above it, and the oscillating tip slightly taps the surface at the resonant frequency of the cantilever (70–400 kHz) with a constant (20–100 nm) amplitude of vertical oscillation, and a feedback loop keeps the average normal force constant. The oscillating amplitude is kept large enough that the tip does not get stuck to the sample due to adhesive attraction ("snap to contact" phenomenon). The tapping mode is used in topography measurements to minimize the effects of friction and other lateral forces to measure the topography of soft surfaces. To obtain topographic information, the interaction force is either recorded directly, or used as a control parameter for a feedback circuit that maintains the amplitude. Using an AFM operated in the contact mode, topographic images with a vertical resolution of less than 0.1 nm (as low as 0.01 nm) and a lateral resolution of about 0.2 nm have been obtained.

The AFM data require special processing for eliminating such undesired effects, which result from very different sources like the intrinsic non-linearity of the scanner, an improper tip-sample feedback, electrical noise or the tip convolution effects (artefacts).

AFM manufacturers have gained much experience in eliminating most of them with the improvement of software, hardware and control electronics.

A.2 Infrared Reflection Absorption Spectroscopy (IRRAS)

The infrared reflection absorption spectroscopy is a surface sensitive technique, used to identify a wide range of functional groups present on a surface as well their orientations relative to the reflective surface. This technique is applied to thin films on highly reflective surface, like in the case of SAMs on metal surfaces.

The first experimental proof was given by Greenler,[2] which observed that the absorption of infrared radiation was enhanced at high angle of incidence and involved only one polarization of the incident light.

In IRRAS, the light that is measured consists of the polarization which stems from the constructive interference. The reflected parallel or p-polarized radiation has amplitude which is almost twice that of the incident radiation, because of the constructive interference, the incident and the reflected vectors are summed. In the case of the perpendicular or s-polarized radiation, the incident and the reflected vectors undergo to a 180° phase shift relative to each other and cancel each other through a destructive interference, resulting in

zero absorbance. The only active vibrations which are observed consist of bonds vibrating in the direction normal to the metal surface, which means that in IRRAS spectra the individual peaks represent specific functional groups with bonds perpendicular to the surface.

A.3 X-Ray Reflectivity (XRR)

The specular X-ray reflectivity is a non-destructive powerful method to study multilayered structures, up to 100 nm, in order to retrieve important parameters such as thickness, density and roughness for each layer, starting from the electron density distribution. In a routine experiment, the sample is irradiated with an x-ray beam with an angle θ_i and the refracted beam is collected with a detector placed at an angle θ_r, in a specular geometry where $\theta_i = \theta_r$. A typical reflectivity curve is represented In Figure 1.

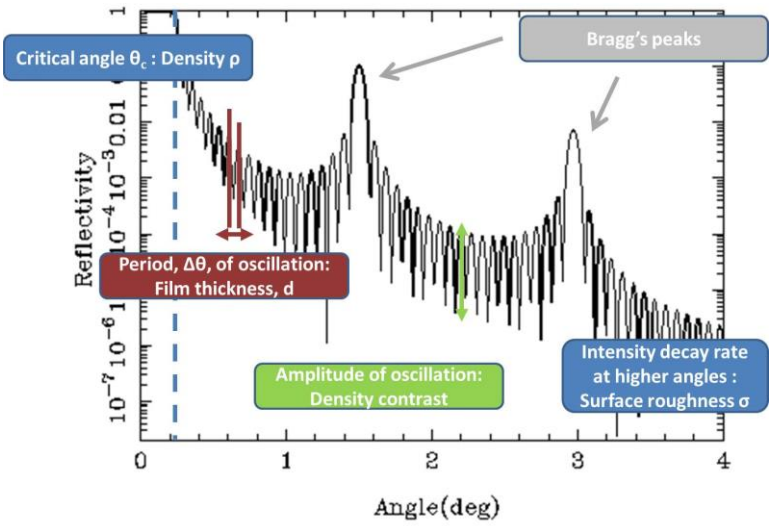

Figure 1 - Reflectivity curve with its characteristics parameters.

The first part of the curve is characterized with the presence of a plateau, followed by a fast decrease of the reflectivity. The point where the plateau ends is defined as the critical angle θ_c, which corresponds to the angle at which the incoming beam is totally reflected from the surface, and it depends only on the substrate. Moving towards higher angles, the beam penetrates in the sample. Depending on the number on layers present in the sample, the reflectogram will show oscillations, generated from the interference of the reflections coming from the buried layers. These oscillations are called Kiessing fringes, and from their period is possible to calculate the thickness of the layers. From the amplitude of the oscillation is possible to obtain the density contrast between layers. In the case of multilayer stack with a repeated thickness, is possible to observe Bragg peaks, which will be positioned at the angle corresponding to the layering distance. The roughness of both surface and interface, between each layer, will affect the intensity of the reflectivity because it will reflect less that ideally flat surface which brings to an intensity decay rate at higher angles.

In order to give the correct interpretation to the reflectivity curves some mathematical approaches have been developed. The most used is the so-called Parrat recursion formalism, developed by Parrat in the 1954, when was studying oxidized copper films.[3]

This formalism accounts the effect of reflection from each internal interface, including their coherent interference to yield the final reflection intensity. The reflected and transmitted amplitude of layer j are given by R_j and T_j, such that:

$$X_j = \frac{R_j}{T_j} = e^{-2ik_{z,j}z_j}\frac{r_{j,j+1} + X_{j+1}e^{2ik_{z,j}z_j}}{1 + r_{j,j+1}X_{j+1}e^{2ik_{z,j}z_j}}$$

Where

$$r_{j,j+1} = \frac{k_{z,j} - k_{z,j+1}}{k_{z,j} + k_{z,j+1}}$$

Is the Fresnel coefficient for interface j. The boundary conditions used to solve the system of equation are T_1=1, which is the incident wave normalized to unity and R_{N+1}=0, where no reflection from the bottom of the substrate are present.

For sufficiently large incident angle ($\theta_i >> \theta_c$), is possible to use a kinematical approximation, using the so-called Master Formula:

$$R(q_z) = R_F \left| \frac{1}{\rho_e(z \to \infty)} \int_{-\infty}^{+\infty} \frac{d\rho_e}{dz} e^{iq_z z} dz \right|^2$$

Where R_F , which is the Fresnel reflection,is expressed by the equation:

$$R_F = \left| r_{j,j+1} \right|^2$$

It should be noted that this is essentially a Fourier transform of the electron density variation and is possible to obtain directly the electron density profile related to the thickness of each layer.

A.4 References

1. Binnig, G. & Quate, C. F. Atomic Force Microscope. *Phys. Rev. Lett.* **56,** 930–933 (1986).

2. Greenler, R. G. Infrared Study of Adsorbed Molecules on Metal Surfaces by Reflection Techniques. *J Chem Phys* **44,** 310–315 (1966).

3. Parratt, L. G. Surface studies of solids by total reflection of x-rays. *Phys. Rev.* **95,** 359–369 (1954).

Resumen en castellano

El objetivo principal de esta tesis ha sido el estudio de la funcionalización de superficies ferromagnéticas mediante la formación de monocapas moleculares autoensambladas, (SAMs, *self-assembled monolayers*) con el fin de conseguir procesos sencillos y fiables para la preparación de interfaces híbridas aplicables en dispositivos de espintrónica molecular.

La investigación se ha centrado en la funcionalización de materiales ferromagnéticos, concretamente el cobalto y la aleación de níquel:hierro conocida como Permalloy. Las propiedades magnéticas y de polarización de espín de estos metales ferromagnéticos se mantienen a temperatura ambiente, lo que los hace muy interesantes para su aplicación práctica en dispositivos reales. Sin embargo, estos materiales presentan el inconveniente de su fácil oxidación en condiciones ambientales, que les hace desarrollar una capa de óxido antiferromagnética que pasiva la superficie.

Este manuscrito se divide en: un capítulo de introducción, tres capítulos de resultados, un apartado de conclusiones y perspectivas generales, una sección que describe la metodología experimental desarrollada y empleada a lo largo de la tesis y finalmente ,un apéndice de marco teórico de algunas técnicas de caracterización.

En el capítulo de introducción se presentan brevemente los conceptos usados en el desarrollo de esta tesis: (1) descripción del concepto de SAM y su estructura, (2) resumen de las técnicas de caracterización de superficies usadas para estudiar las monocapas y (3) varias aplicaciones de las SAMs en diferentes campos, con especial hincapié en el campo de la espintrónica molecular.

La SAM se forma a partir de la autoorganización de una molécula de surfactante en una superficie por vía vapor o en disolución. Las moléculas que forman la SAM se dividen en tres partes: (i) Grupo funcional que define la afinidad a anclarse en determinado tipo de superficie, (ii) cuerpo o esqueleto cuyas interacciones intermoleculares débiles ayudan a la correcta autoorganización en la monocapa y (iii) grupo funcional terminal que definirá las características de la nueva superficie como el carácter hidrófilo/hidrófobo de la misma, o la carga superficial etc. Técnicas que se usan comúnmente para su caracterización son: Medidas de ángulo de contacto, microscopía de fuerza atómica (AFM), espectroscopia Raman, espectroscopia infrarroja por reflexión (IRRAS), espectroscopia de electrones (Auger) o de rayos-X (XPS: espectroscopia de fotoelectrones emitidos por rayos-X y XAS: espectroscopia de absorción de rayos-X), reflexión y difracción de rayos-X (XRR y XRD respectivamente) y la espectrometría de masas de desorción/ionización láser asistida por matriz acoplada a un detector de tiempo de vuelo (MALDI-TOF).

La formación de SAMs se ha aplicado para control y modificación de la hidrofobicidad de las superficies, como enganche para el anclaje de otras especies a la superficie (con especial interés en el desarrollo de sensores o detectores), como capa protectora incluso frente a tratamientos de ataque

químico, y en electrónica molecular, participando como diferentes componentes electrónicos de los sistemas. En el siglo XXI, las SAMs han encontrado aplicación en el campo de la espintrónica molecular. La espintrónica se basa en el uso no sólo de la carga del electrón sino también de su espín, para almacenar y procesar información. La espintrónica molecular incorpora el uso de los materiales orgánicos, ya que al estar compuestos por elementos ligeros, como carbono, hidrógeno y oxígeno, tienen interacciones hiperfinas y acoplamiento espín-orbita muy débiles, que promueven la alta difusión del espín. Este factor es importante a la hora de sustituir por moléculas los materiales tradicionales y óxidos inorgánicos, que se usan como barreras para separar dos electrodos ferromagnéticos. Los primeros trabajos que emplearon una SAM como espaciador, entre dos electrodos de níquel, o de níquel y cobalto, se publicaron respectivamente por Petta en el 2004 y Wang en el 2006. Ambos, detectaron el magnetorresistencia de efecto túnel (TMR) en su geometría de unión túnel magnético (MTJ). Dicho efecto, es la base de funcionamiento de las MTJ. Cuando se aplica una diferencia de potencial, se genera una corriente polarizada que fluye desde el electrodo ferromagnético inferior hasta el electrodo ferromagnético superior, que atraviesa el separador, normalmente un material no magnético. La magnitud de la corriente depende de la orientación de la magnetización de los electrodos. Aplicando un campo magnético externo, es posible actuar singularmente sobre cada electrodo ferromagnético, cambiando dicha orientación de paralela a anti paralela. Este giro produce un aumento en la resistencia del tránsito de los electrones. Resumiendo, dependiendo de la orientación relativa de los electrodos es posible definir dos estados diferentes de resistencia eléctrica. Para garantizar el

giro selectivo, se pueden usar diferentes materiales ferromagnéticos. El efecto túnel se debe al carácter aislante del espaciador, y su grosor nanométrico. En los ejemplos reportados en literatura, ambos autores han evidenciado estos cambios de resistencia, desafortunadamente a la temperatura de 4 K. Otro ejemplo más reciente, fue reportado por Galbiati et al., que usó un óxido de lantano, manganeso y estroncio (LSMO) que posee una polarización de espín del 100% a bajas temperaturas. Estos resultados tan prometedores dejan el campo abierto a nuevas investigaciones hacia la incorporación de SAMs en dispositivos espintrónicos que funcionen a temperatura ambiente, lo que explica la motivación de esta tesis.

En el capítulo dos, hemos investigado la posibilidad de formar SAMs de cadenas alquílicas utilizando la capa de óxido superficial que pasiva al permaloy ya que en la literatura no se han encontrado protocolos para su funcionalización. Elegimos como grupo de anclaje el ácido fosfónico que se usa tradicionalmente para funcionalizar los óxidos de metales y trabajamos con ácidos alquilfosfónicos de diferente longitud de cadena empezando por el ácido dodecilfosfónico (C12P), hasta el ácido octadecilfosfónico (C18P). Recurrimos a diferentes tratamientos con plasma como alternativa para limpiar y/o activar el óxido, y observamos que tratando la superficie con un plasma suave de hidrógeno, se produce un incremento en la cantidad de hidróxidos lo que aumenta la reactividad. De hecho, al exponer una superficie pre-tratada con hidrógeno, observamos una disminución de ángulo de contacto del agua, respecto a las muestras expuestas solamente a disolvente. Tras las funcionalización con las moléculas de alquilfosfónico, la superficie modificada presenta un carácter hidrófobo, con ángulos mayores de 110^{o} y el valor sigue

una tendencia monótona al aumentar la longitud de la cadena de carbonos, pasando de 110 º para un C12P hasta un 118 º para un C18P. Esta variación de hidrofobicidad de la superficie, también fue empleada para estimar en cuánto tiempo se forma una monocapa completa sobre este sustrato. El resultado fue que, el crecimiento de la monocapa está formado por dos procesos cooperativos, de duración total de 3 horas. La primera etapa es la aproximación de las moléculas a la superficie y que tiene lugar en unos pocos segundos y la segunda es la reorganización molecular, que dura unas decenas de minutos. Todo el proceso de crecimiento se lleva a cabo siguiendo el modelo de crecimiento uniforme, en el cual se forma un film de moléculas recostadas sobre la superficie y a medida que el recubrimiento crece, las moléculas van adquiriendo una inclinación uniforme, según su empaquetamiento hasta llegar a la formación de una monocapa ordenada. Pudimos obtener información sobre los ángulos de inclinación, respecto a la normal de la superficie, mediante IRRAS, una técnica de caracterización sensible a las vibraciones perpendiculares a la superficie de los grupos funcionales. Según se aumentaba la longitud de la cadena, observamos un ángulo menor de inclinación, relacionado con su grosor, que indicaría la transición desde un film menos ordenado hacia uno más ordenado. Combinando este dato con la información extraída por XRR, obtuvimos el grosor de la SAM formada, desde 1.5 nm en el caso de C12P hasta 2.5 nm en el del C18P. Además, mediante el uso de la técnica de XPS, identificamos la presencia de fósforo, relacionada con el grupo fosfónico en la superficie y estudiando el cambio en las intensidades de los picos de níquel y carbono, en función de la molécula usada, pudimos obtener una tercera estimación del grosor molecular, confirmando los valores del XRR.

Utilizamos la espectrometría de masas MALDI–TOF como técnica con ionización suave que garantiza la ausencia de fragmentación del analito y nos permitió demostrar la integridad de las moléculas en la superficie. Además, no se detectaron picos relativos a la presencia de una multicapa, situados teóricamente al doble del peso molecular más un átomo de hidrógeno. El C18P, pudo ser estudiado por esta técnica debido a interferencias en el espectro con la matriz usada para transferir electrones al analito. Las propiedades magnéticas de las superficies funcionalizadas fueron detectadas por espectroscopia magneto óptica del efecto Kerr (MOKE), que se basa en el estudio de la variación en la polarización de un láser al incidir en la superficie magnética, en presencia de un campo magnético externo. Es una técnica muy sensible al magnetismo de superficies. El óxido de permaloy se ordena antiferromagnéticamente a bajas temperaturas. El grueso del material, de forma opuesta, tiene un comportamiento ferromagnético. La cercanía de un material ferromagnético a otro antiferromagnético se refleja en un ensanchamiento de la curva de histéresis magnética, debido al fenómeno de interacción de canje. La histéresis magnética de una muestra funcionalizada con la SAM de ácidos alquilfosfónicos es igual a una muestra sin funcionalizar, oxidada al aire. Eso demuestra que la funcionalización no afecta a las propiedades magnéticas del óxido y del grueso del material. Para comprobar la calidad de nuestra SAM, se consiguió dibujar un patrón de líneas por medio de un método de litografía suave, llamado impresión por microcontacto (*microcontact printing*). Se embebió un sello de una resina polimérica, que presenta un patrón de líneas, con una disolución de ácidos alquilfosfónico, y lo pusimos en contacto con una superficie oxidada de permalloy, previamente

tratada con plasma de hidrógeno. Debido al contacto directo entre la molécula y la superficie a funcionalizar, la reacción tiene lugar en cuestión de segundos, obteniendo la transferencia del patrón de líneas. Se estudió la topografía de la superficie por AFM, en modo contacto, ya que, de otra manera no se podía visualizar. Para poder revelar el patrón, se expuso la superficie a una disolución de ácido glicólico, que ataca las zonas no funcionalizadas. El resultado final fue un patrón de líneas, con resolución micrométrica, que demuestra la validez de estas SAMs como barreras resistente a un ataque químico. Como conclusión del capítulo 2 podemos destacar que, se ha llevado a cabo por primera vez la funcionalización del óxido de permalloy, que no había sido reportada en literatura. El punto crítico fue el pretratamiento de la superficie con un plasma de hidrógeno suave, que promueve el incremento de grupos hidróxido en el óxido original, favoreciendo la reacción de condensación con el grupo fosfónico. Se ha logrado formar una SAM de ácidos alquilfosfónicos, compacta y de tamaño nanométrico. Su robustez se ha comprobado con su uso como agente resistente a un ataque químico y protector de la superficie de permaloy subyacente.

En el capítulo tres pasamos al estudio de la funcionalización directa del material ferromagnético (cobalto o permalloy). El objetivo fue recuperar metales ferromagnéticos que ya han sido expuestos al aire y por tanto pasivados con una capa de óxido antiferromagnético que representa una fuente de despolarización del espín. El ataque del óxido permite que quede expuesto directamente el material ferromagnético para reaccionar con la unidad molecular que dará lugar a la formación de la SAM. Para la funcionalización de metales como oro, plata y cobre, generalmente, se han empleado SAMs de

alcanotioles. Se han reportado métodos variados de ataque del óxido que o resultan caros u originan superficies rugosas, que no son compatibles con trabajo en atmosfera inerte o con procesos litográficos y por tanto no son óptimos para su aplicación en la fabricación de dispositivos espintrónicos. Durante nuestra investigación se observó que al exponer una superficie oxidada de cobalto o permaloy a una disolución etanólica de ácido glicólico, se producía un ataque completo (etching) del material. Repitiendo el mismo experimento en atmósfera inerte, el proceso se detenía una vez que había alcanzado la superficie metálica, resultado en un ataque selectivo de la capa de óxido. Por XPS se comprobó la ausencia de picos de oxígeno, que confirma una recuperación del metal desnudo. Las propiedades magnéticas después del tratamiento han revelado también que se han recuperado los campos coercitivos de una muestra que no presenta óxido superficial. La funcionalización con una SAM se llevó a cabo exponiendo las superficies a una disolución de ácido glicólico en atmósfera inerte y tras transcurridos 15 minutos, se les añadió la disolución de alcanotioles deseada. El resultado, tras pasar 16 horas de reacción, se detectó con un aumento de la hidrofobicidad de la superficie, respecto a la superficie que fue expuesta sólo al ácido glicólico. Se ha observado que, a medida que la cadena usada para funcionalizar la superficie aumentaba de doce átomos de carbonos (C12S) a dieciocho (C18S), el ángulo de contacto de agua pasaba de110° a 114 °. Continuando con la caracterización, sin exponer la superficie funcionalizadas al aire, se ha observado mediante medidas de absorción de rayos-X que la formación de la SAM en la superficie tras la eliminación del óxido, no provocaba la re-oxidación de esta..

En colaboración con CNRS\Thales, se fabricaron MTJ de área nanométrica mediante litografía láser, para disminuir la probabilidad de cortocircuitos. La superficie del permalloy, se funcionalizó aplicando la metodología desarrollada en este capítulo con una SAM de alcanotioles y se completó el dispositivo con un electrodo superior de cobalto. Se pudo detectar un efecto de TMR del 16% a temperatura ambiente, en un dispositivo que empleaba una monocapa de C16S.

Resumiendo, la exposición, en atmósfera inerte de un sustrato oxidado de cobalto o permaloy a una disolución de ácido glicólico, permite el ataque selectivo del óxido antiferromagnético, sin afectar las propiedades magnéticas del grueso del material y además permite su funcionalización con una SAM de alcanotioles que puede integrarse en dispositivos espintrónicos. Finalmente hay que destacar que se observó un comportamiento anómalo una vez los sustratos funcionalizados con alcanotioles eran expuestos al aire, ya que se detectó por microscopia óptica el crecimiento espontáneo de dominios laminares en la superficie.

En el capítulo 4 describimos el estudio para identificar la naturaleza de estos dominios laminares, que aparecen exclusivamente, en las superficies metálicas ferromagnéticas funcionalizadas con SAM y expuestas al aire, de manera espontánea, sin ningún tipo de estímulo externo. La primera hipótesis que descartamos fue que estaban compuestos por óxidos inorgánicos, ya que se encontró una dependencia lineal de la altura de escalón que se define de forma repetitiva en estos dominios, con la longitud de cadena de la molécula usada para funcionalizar la superficie; a medida que la longitud de la molécula

aumenta, observamos que la altura de escalón también aumentaba desde 3.6 nm hasta 4.6 nm, al pasar de un C14S a un C18S, respectivamente. Este resultado fue confirmado también por medidas de XRD que evidenciaron la dependencia con la molécula usada para funcionalizar la superficie, sobre todo por la correlación linear que es una clara señal de que estos dominios comparten la misma estructura interna. En base a estos estudios de AFM y XRD, y en la existencia de estructuras conocidas crecidas en polvo de materiales laminares de alcanotioles que coordinan cationes metálicos según la fórmula RS-M-SR, intentamos hacer un modelo que describiera la estructura de los dominios observados, sin embargo este es sólo una aproximación debido al error experimental en las medidas de AFM y de XRD.

Por AFM también, ha sido posible determinar la altura media por material (cobalto o permaloy) y por cadena empleada, observando que con C14S se obtienen islas más altas, hasta unas 10 capas, y con C18S se obtienen islas más finas, de una capa. Este resultado se mantiene también pasando de cobalto a permalloy. Por medio de microscopia óptica, se ha estudiado el área media de las islas, pudiendo abarcar superficies amplias en cuestión de minutos, en lugar de recurrir al AFM, para una medida más exacta, pero que requiere mayor tiempo y por tanto menor superficie analizada. Se ha observado que utilizando la cadena más corta C14S, se obtiene una baja densidad de islas, pero con mucha variedad de tamaños, por encima de las 90 micras cuadradas. Sin embargo, con la molécula más larga C18S, se obtiene una alta densidad de islas, pero de tamaño inferior a las 20 micras cuadradas. La densidad obtenida se refleja en el recubrimiento de la superficie, siendo eso alrededor de un 6% para el C14S y un 24% para el C18S. Mediante el estudio de la altura media obtenida

por AFM, y del área media, obtenida por microscopía óptica, se pueden hacer estimaciones rápidas, sobre qué cantidad de material, que originariamente formaba parte de la SAM en la superficie, y después se ha reorganizado en los dominios laminares. Según los cálculos, siempre queda parte de las moléculas en la superficie ocupando el espacio entre los dominios, siento en el caso de moléculas más largas (C18S) cuando mayor proporción de moléculas migran hacia los dominios. También se ha evidenciado desde los histogramas de altura, que existe un fenómeno de interdigitación entre los dominios formados con la monocapa subyacente en el caso del C18S. En el caso de C16S y C14S, no se ha relevado este tipo de interacción entre la monocapa y los dominios.

Las medidas hechas por espectroscopia Raman y Auger con carácter local, han servido para confirmar nuestro primer modelo de composición de los dominos laminares, mediante su potente resolución espacial. La espectroscopia Raman, ha sido útil para localizar y medir las vibraciones pertenecientes a las cadenas alquílicas en los dominios laminares. Por otro lado, la espectroscopia Auger, ha confirmado la presencia de iones cobalto y de azufre en el interior de las islas, desafortunadamente no se logrado estimar su estado de oxidación, debido a las limitaciones de la técnica. Los resultados confirman nuestra idea preliminar de una estructura tipo sandwich, donde las cadenas alquílicas se extienden por arriba o por debajo de una capa de iones metálicos a los que coordinan por el azufre.

Así mismo también ha sido posible seguir la aparición y evolución de los dominios al entrar en contacto la muestra con el aire, por medio de AFM y de microscopía óptica. Cabe resaltar que estos dominios laminares, tienen no sólo

una etapa de crecimiento en vertical, sino también en lateral, sufriendo también etapas de coalescencia, cuando dos o más dominios se encuentran, para fundirse en uno de tamaño mayor. Se ha detectado que la evolución en área y altura dura aproximadamente 16 horas hasta llegar a una situación estable. Para probar que efectivamente los dominios sólo aparecían al contacto con el aire, se realizaron medidas de AFM de muestras que nunca habían sido extraídas de la caja seca tras la funcionalización, gracias al equipamiento disponible en los laboratorios de CNRS\Thales en el grupo del profesor P. Seneor. Allí existe un AFM dentro de la caja seca donde se realiza el tratamiento con ácido glicólico y posterior crecimiento de la SAM, lo que permite la adquisición de la imagen previa a la exposición al aire, sin embargo, la calidad de las imágenes se ve comprometida por las vibraciones de la caja. Para comprobar el papel que juegan la temperatura y la humedad en el crecimiento espontáneo de los dominios laminares se realizaron dos tipos de experimento diferentes, en el primero se prepararon diferentes muestras de monocapas sobre cobalto en caja seca y al sacarlas unas se introdujeron en el nevera a 5°C, otras se dejaron a temperatura ambiente y otras se colocaron sobre una placa calefactora a 35°C, la muestras se inspeccionaron por microscopía óptica tras 23 horas y se observó que las islas habían crecido en todos los substratos, pero que en las muestras a menor temperatura el número de islas era mucho mayor pero estas eran de tamaño mucho más pequeño, mientras que las muestras a alta temperatura el número de islas era menor pero estas tenían una tamaño mucho mayor en área y altura, este comportamiento se asemeja a la cristalización de sistemas en disolución ya que la falta de energía térmica dificulta la migración de las moléculas. Para estudiar

la influencia de la humedad se prepararon muestras de monocapas en cobalto en la caja seca que al extraerse se expusieron una a la atmósfera normal del laboratorio y otra dentro de un dispositivo con un flujo de aire seco. Tras 16 horas se estudiaron las muestras por microscopía óptica (al ambiente) y se observó que en ausencia de humedad las islas también habían aparecido sin diferencias de tamaño o número muy significativas aunque siempre inferiores que en el caso de la muestra en aire seco. Ambos tipos de muestra se dejaron expuestas al ambiente del laboratorio y tras 16 horas más se vio que la muestra que habían estado expuesta al aire húmedo ambiental desde el principio no sufría ninguna evolución mientras que la que había estado en aire seco durante las primeras horas seguía evolucionando en tamaño y número hasta alcanzar una estadística similar a la otra muestra. Este estudio parece indicar que aunque la humedad no es determinante para la aparición de los dominios laminares, sí que determina su velocidad de crecimiento.

Por otro lado, hemos observado que, si se toman imágenes consecutivas con el AFM sobre uno de estos dominios, se produce un fenómeno raro e impresionante a la vez, donde a medida que el número de imágenes aumentan, el área y altura de la misma van disminuyendo de manera notable y de forma discreta (capa a capa). De hecho, el efecto que se nota es que el material desaparece al pasar la punta del AFM, que está midiendo en modo tapping, es decir, en contacto intermitente entre la punta y la superficie y no arrastra el material. Esto puede significar que el material: 1) no está enlazado covalentemente con la superficie, 2) no tiene mucha interacción entre capas, que conlleva al punto 3) que es un material que se puede delaminar en superficie. Un aspecto importante, es que en las zonas donde se ha quitado el

material, no se evidencia la presencia de un agujero en la superficie, que significa que la SAM subyacente a la isla tiene una conformación homogénea.

A la vista de los resultados obtenidos, proponemos un mecanismo de formación de los dominios laminares basado en el idea de que la SAM se forma en condiciones de atmósfera inerte de forma normal, pero una vez expuesta al aire, el oxígeno encuentra unos defectos para empezar a reaccionar oxidando la superficie metálica y una vez oxidados algunos centros metálicos, se produce una migración de estos iones coordinados por los tioles fuera de la superficie por encima de la SAM, obligando a que las otras moléculas que forman parte de la monocapa se reorganicen. El proceso sigue hasta que todos los iones metálicos se oxidan y que la monocapa disminuye drásticamente su densidad.

Después de nuestro estudio exhaustivo sobre la funcionalización molecular de los metales ferromagnéticos y las conclusiones principales extraídas, surgen nuestras perspectivas que investigar. La formación de SAMs sobre la capa pasivante de óxido sin afectar el metal subyacente y compactas y homogéneas que pueden nanoestructurarse por litografía suave y pueden usarse de agente protector frente a ataque químico nos lleva a intentar dibujar estructuras más complejas de permaloy propias de circuitos, que pueden aprovecharse en la preparación por ejemplo de nanosensores. La preparación de las SAMs directamente sobre el material ferromagnético recuperado nos ha motivado a trabajar a la implementación de esa metodología para la formación de SAMs más complejas, por ejemplo como constituidas por radicales orgánicos, que pueden ser de interés especial como interfaces en dispositivos espintrónicos. En referencia a la formación espontánea de dominios cuando las superficies

funcionalizadas son expuestas al aire, todavía, quedan unas cuestiones abiertas que se tendrán que investigar con más detalle. Por ejemplo, sobre el mecanismo que está involucrado en la formación de esas islas, el tipo de coordinación de los iones metálicos, o si es posible de evitar la formación de esas islas preparando SAMs interconectadas que pudieran prevenir la oxidación de la superficie. Además, queremos estudiar si el uso de una superficie metálica, en lugar de una superficie recuperada, juega un papel importante en la aparición y crecimiento de las islas.